Improving the electrolyte - cathode assembly for mt-SOFC

Nicolas Hildenbrand

Cover: Scanning Electron Microscopy micrograph of the cross-section of a Solid Oxide Fuel Cell built by means of Pulsed Laser Deposition, using a traditional (Ni/YSZ) cermet anode as substrate.

Ph.D. committee:

Chairman and secretary:

prof. dr. G. Van der Steenhoven (University of Twente)

Supervisor:

prof. dr. ing. D.H.A. Blank (University of Twente)

Assistant supervisor:

dr. B.A. Boukamp (University of Twente)

Members:

prof. dr. S.J.G. Lemay (University of Twente)

prof. dr. J. Schoonman (University of Delft)

dr. H.J.M. Bouwmeester (University of Twente)

prof. dr. ing. A.J.H.M. Rijnders (University of Twente)

Referents:

dr. N. Bonanos (Technical University of Denmark)

dr. F.P.F. van Berkel (Energy research Centre of the Netherlands)

The work described in this thesis was carried at the Inorganic Materials Science department at the Faculty of Science and Technology and the MESA+ Institute for Nanotechnology, University of Twente, P.O. 217, 7500 AE Enschede, the Netherlands.
This research was financially supported by SenterNovem, an agency of the Dutch Ministry of the Economic Affairs through the EOS-SOFC program.

N. Hildenbrand
Improving the electrolyte – cathode assembly for mt-SOFC,
Ph.D. thesis University of Twente, Enschede, the Netherlands.

ISBN: 978-94-91211-57-7
Printed by Ipskamp Drukkers

IMPROVING THE ELECTROLYTE - CATHODE ASSEMBLY FOR MT-SOFC

PROEFSCHRIFT

ter verkrijging van
de graad van doctor aan de Universiteit Twente,
op gezag van de rector magnificus,
prof. dr. H. Brinksma,
volgens besluit van het College voor Promoties
in het openbaar te verdedigen
op vrijdag 10 juni 2011 om 16:45 uur

door

Nicolas Hildenbrand

geboren op 26 oktober 1981
te Mulhouse, Frankrijk

Dit proefschrift is goedgekeurd door:

prof. dr. ing. D.H.A. Blank (promotor) en
dr. B.A. Boukamp (assistant-promotor)

Contents.

Introduction..... 1
1. Solid Oxide Fuel Cells..... 4
1.1. Basic principles..... 4
1.2. Fuel cell efficiency..... 5
1.2.1. Heating efficiency..... 5
1.2.2. Thermodynamic efficiency..... 6
1.2.3. Current efficiency..... 6
1.2.4. Voltage efficiency..... 7
1.3. Overpotential – Polarization..... 7
1.3.1. Charge transfer or activation polarization..... 8
1.3.2. Reaction polarization..... 8
1.3.3. Resistance or ohmic polarization..... 9
1.3.4. Diffusion or concentration polarization..... 9
1.4. Materials for SOFC..... 11
1.4.1. Anodes..... 11
1.4.2. Electrolytes..... 12
1.4.3. Cathodes..... 14
2. Scope of this thesis..... 16
References..... 17

Chapter 1. Experimental considerations..... 19
1. Deposition techniques..... 20
2. Characterization techniques..... 21
3. Experimental set-up..... 22
4. Electrochemical Impedance Spectroscopy (EIS)..... 24
4.1. Theory - Physical modeling of the system..... 24
4.1.1. Impedance spectroscopy..... 24
4.1.2. Processes and their representation in EIS..... 27
4.1.2.1. Semi-infinite Diffusion - Warburg impedance..... 27

4.1.2.2. Finite Space Warburg…… 29
4.1.2.3. Finite length Warburg…….... 29
4.1.2.4. Finite length Diffusion…….. 30
4.1.2.5. Constant Phase Elements…… 30
4.1.2.6. Gerischer impedance…… 32
4.2. Data validation…… 33
4.3. Complex Nonlinear Least Squares Analysis……... 34
References……... 38

Chapter 2. Characterization of Gadolinium Doped Ceria as electrolyte for SOFC..... 41
1. Introduction..... 42
2. Experimental..... 44
2.1. Synthesis of CGO powders..... 44
2.2. Complexation route using citric acid..... 44
2.3. Complexation route using ethylene glycol..... 45
2.4. Characterization..... 46
3. Results and discussion..... 47
3.1. Powder characterization..... 47
3.2. Sintering behavior..... 50
3.3. Microstructure..... 51
3.4. Conductivity measurements..... 52
3.5. TEM characterization..... 55
4. Conclusions..... 57
References..... 58

Chapter 3. The impedance of thin dense oxide cathodes..... 59
1. Introduction..... 60
2. Theory: Generic Finite Length Diffusion (GFLD) equation..... 61
3. Experimental procedure..... 64
4. Results and discussion..... 65
4.1. Effect of the electrode layer thickness..... 65
4.2. Effect of the current collector..... 68
4.3. Effect of Cr poisoning..... 70
5. Conclusions..... 71

References..... 71

Chapter 4. The effect of microstructure on the performance of LSCF cathodes..... 73
1. Introduction..... 74
2. Experimental..... 77
3. Results and discussion..... 77
3.1. Microstructure..... 77
3.2. Effect of sintering temperature on the cathode's performance.... 79
3.3. Modeling with different equivalent circuits..... 81
3.4. Temperature and oxygen partial pressure dependences..... 82
4. Conclusions..... 86
References..... 87

Chapter 5. Improved cathode / electrolyte interface of SOFC..... 89
1. Introduction..... 90
2. Experimental..... 90
3. Results and discussion..... 92
3.1. Microstructure..... 92
3.2. Temperature dependence..... 94
3.3. Oxygen partial pressure dependence..... 97
4. Conclusions..... 102
References..... 102

Chapter 6. Investigation of $La_2NiO_{4+\delta}$ cathodes to improve SOFC electrochemical performance..... 105
1. Introduction..... 106
2. Experimental..... 107
3. Results and discussion..... 108
3.1. Microstructure..... 108
3.2. XRD characterization..... 111
3.3. Effect of sintering temperature and of the PLD layer on the polarization resistance..... 111
3.4. Electrical characterization..... 114
3.4.1. Description of the impedance spectra..... 114

3.4.2. Equivalent circuit explanation valid for all types of samples.. 115
3.4.3. Equivalent circuit explanation valid for samples with a dense LNO layer..... 119
3.5. Discussion..... 119
3.5.1. Discussion of the LNO samples..... 119
3.5.2. Discussion of the LNO and LSCF samples..... 122
4. Conclusions..... 124
References..... 125

Chapter 7. Pulsed Laser Deposition: A tool to produce SOFC?..... 129
1. Introduction..... 130
2. Experimental..... 131
3. Result and discussion..... 133
3.1. Cleaning procedure..... 133
3.2. Growth of 8YSZ electrolyte thin films..... 135
3.3. Fuel cell characterization and microstructure..... 137
4. Conclusions..... 140
References..... 140

Summary and Outlook..... 143
Sammenvatting..... 149

Dankwoord / Acknowledgement / Remerciements..... 155

Introduction

At the beginning of the 21st century, a large consensus among the scientific world has been reached about the effects of human activities on the Earth's climate [1]. Since the industrial revolution in the 19th century, the technological progresses of our societies have been mainly based on the use of fossil fuels: coal, natural gas and oil. When those fossil fuels are burnt during our activities, greenhouse gases are released and quickly change – compared to typical time frame of natural changes – the composition of the atmosphere. The interaction of the radiation of the sun with these greenhouse gases leads to a global warming of the Earth atmosphere at a very rapid pace. The speed of global warming and its inevitable consequences are still under debate. They will vary from one region to the other. Melt of eternal snow and glaciers, elevation of the sea level, extension of desert areas, important changes in the streaming patterns of the oceans, strong and unpredictable weather phenomenon's are examples of changes that will completely change our ecosystem. The international community is trying to reach an agreement to limit the increase of the average Earth temperature to 2°C at the end of the century in order to avoid too dramatic changes [1].

Limiting the increase of the average Earth temperature means that we need to limit the release of greenhouse gases in the atmosphere. Our consumption of fossil fuel should thus decrease and be replaced by energies or energy vectors that are more environment friendly. Different options are available. When looking at the greenhouse gas emission only, nuclear power (fission) is a good alternative. However, the radioactive waste and the limited resources in uranium (common fuel needed for the nuclear power plants) are problematic and this route cannot be seen as a long term and stable solution. Nuclear fusion would be a good solution as it produces only limited radioactive waste (mainly the walls of the power plant) but many decades of research still need to be done before one can hope to use this technology. Renewable energies are seen as part of the solution to our still increasing energy demand: photovoltaic cells and wind turbines producing electricity, bioethanol can be produced from plants, waste or algae's. However, the wind does not blow and the sun does not shine 24 hours a day and 365 days per year, the agricultural areas should be used to produce food before being used to produce bioethanol for our car's fuel. Even if the over-production of

electricity can be stored in batteries, those solutions will probably remain partial solutions.

A global solution means that a new and clean vector of energy must be used. Hydrogen could be a good candidate as a new and clean vector of energy instead of the current fossil fuels in our societies. The concept of a hydrogen economy would be to produce hydrogen by different processes and use it to produce electricity with hydrogen fuel cells. Hydrogen would work as the current fossil fuels and fuel cells would produce electricity using hydrogen as a fuel, releasing only heat and water as exhaust gas.

However, using hydrogen as new fuel presents some important drawbacks. As hydrogen has the lowest atomic weight, hydrogen molecules are hardly present naturally on Earth as the gravitational force is too weak to keep them within the atmosphere (but also thermodynamically unstable with oxygen). All hydrogen atoms present are always linked to other atoms like oxygen O in the water molecule H_2O, to carbon C in natural gas CH_4, methanol CH_3OH, ethanol C_2H_5OH or oil, to nitrogen in ammonia NH_3. It means that hydrogen molecules always need to be produced before use in a fuel cell. Another problem of hydrogen is the storage. A very effective way of storing hydrogen still needs to be found. Hydrogen gas is highly flammable and will burn in air at a concentration as low as 4 vol% of hydrogen in air. Hydrogen and air form an explosive gas mixture with volumetric hydrogen concentrations in the range 4 % - 75%. The gas mixtures will detonate by spark, heat or sunlight [2]. Moreover, hydrogen is a very small molecule that makes leakage problems very important. Current natural gas pipelines can not be used to transport hydrogen because the quality of the welding is not good enough to avoid hydrogen leakages.

Fuel cells are electrochemical devices that directly convert chemical energy into electrical energy. From the reaction between a fuel and an oxidant, heat, electricity and exhaust gases are produced. Depending on the type of fuel cells, different fuels can be used: hydrogen, as previously discussed, but also ethanol, methanol or gaseous fossil fuels like natural gas. Solid Oxide Fuel Cells (SOFCs) are examples of fuel cells that work at high temperatures and that can use hydrogen or natural gas as fuel. This aspect is important.

The gap towards a society based on hydrogen economy is relatively wide as one need to solve three problems: the hydrogen production, the hydrogen storage and the development of fuel cells. In the transition period between the current way of life and a (near future?) hydrogen society, it is possible to use natural gas as fuel for Solid Oxide Fuel Cells (SOFCs) and build experience with the SOFC technology. When clean hydrogen production processes and safe storage systems would be ready for the market, it would be possible to switch to this clean fuel without important changes of the technology.
Moreover, the energy conversion efficiency of the SOFC is much higher than of a traditional generator. In a traditional generator, the chemical energy (free enthalpy of the fuel) is converted to heat, the heat to mechanical energy and the mechanical energy to electrical energy. Important losses occur during these three conversions. In a SOFC, the chemical energy is directly converted to electrical energy and heat. As a consequence, SOFCs have a smaller environmental impact (production of CO_2 and NO_x) than traditional generators per kWatt power produced.

SOFCs are still not widely used and commercially available for two main reasons: cost and lifetime/degradation of the fuel cells. To understand those problems, a description of the SOFCs principles and materials is now presented.

1. Solid Oxide Fuel Cells.

1.1. Basic principles.

The electrochemically active part of Solid Oxide Fuel Cell consists of three layers as shown in Figure 1: the cathode, the electrolyte and the anode. In the following description, hydrogen is used as fuel and oxygen is used as oxidant. As discussed previously, other fuels can be used. Oxygen gas, O_2, is reduced in the cathode to oxygen ions O^{2-} according to:

$$O_2 + 4e^- \leftrightarrow 2O^{2-}$$

The oxygen ions diffuse through the electrolyte and react on the anode side with the hydrogen fuel, H_2, to form water, H_2O, according to:

$$H_2 + O^{2-} \leftrightarrow H_2O + 2e^- + heat$$

The overall reaction of the cell is thus:

$$H_2 + \frac{1}{2}O_2 \xleftrightarrow{K_i} H_2O$$

where K_i is the equilibrium constant of the equation is equal to:

$$K_i = \frac{pH_2O}{pH_2 \cdot \left(pO_2\right)^{1/2}}$$

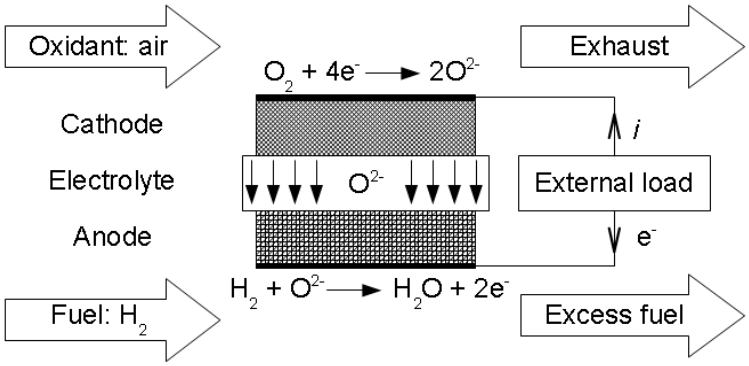

Figure 1. Schematic representation of the electrochemically active parts of a Solid Oxide Fuel Cell.

1.2. Fuel cell efficiency.

Different losses occur in a SOFC. For each loss, it is possible to determine the efficiency as the ratio between the real case and the ideal case. The overall efficiency of the SOFC is then the product of the different efficiencies related to all different losses. In the following section, a description of the different losses and their efficiencies is given.

1.2.1. Heating efficiency.

As the fuel always contains impurities, inert gases and other combustibles in addition to the electrochemically active species, the heating efficiency is defined by:

$$\varepsilon_H = \frac{\Delta H^0}{\Delta H_{com}}$$

where ΔH^0 is the amount of enthalpy of fuel species available in the fuel to generate electricity and ΔH_{com} is the amount of enthalpy of all combustible species in the fuel.

1.2.2. Thermodynamic efficiency.

In a SOFC, the chemical energy is directly converted to electrical energy which means that the free enthalpy change of the cell reaction ΔG may be totally converted to electrical energy. The fuel cell has thus an intrinsic maximum thermodynamic efficiency depending on the reaction which is defined by:

$$\varepsilon_T = \frac{\Delta G}{\Delta H} = 1 - \frac{T\Delta S}{\Delta H}$$

where ΔH is the enthalpy change, *T* is the temperature and ΔS is the entropy change.

1.2.3. Current efficiency.

When all reactants are converted to reaction products, the current density i_F is given by Faraday's law:

$$i_F = zF\frac{df}{dt}$$

where $\frac{df}{dt}$ is the molar flow rate of the fuel and *zF* the charge transferred per mol.

The fuel conversion is always lower than 100%, the real current density *i* is given by:

$$i = zF\left(\frac{df}{dt}\right)_{consumed}$$

The current efficiency, commonly named fuel utilization is thus:

$$\varepsilon_J = \frac{i}{i_F}$$

1.2.4. Voltage efficiency.

In an ideal SOFC, the operating cell voltage is given by the Nernst equation:

$$E_r = \frac{RT}{zF} \ln \frac{p_{cathode}O_2}{p_{anode}O_2}$$

where *R* is the gas constant, *T* the temperature, *F* the Faraday constant and pO_2 the oxygen partial pressure at the given electrode.
Considering the overall fuel cell reaction, the ideal operating cell voltage is given by:

$$E_r = \frac{RT}{4F} \ln K_i + \frac{RT}{4F} \ln p_{cathode}O_2 + \frac{RT}{2F} \ln \frac{p_{anode}H_2}{p_{anode}H_2O}$$

However, parameters such as current density, temperature, pressure, gas flow rate, cell materials, gas combustion have a strong influence on the cell voltage under current load. The voltage efficiency is defined as the ratio of the real operating cell voltage under load *E* to the equilibrium cell voltage E_r given by the Nernst equation:

$$\varepsilon_V = \frac{E}{E_r}$$

Finally, it is possible to define the overall SOFC efficiency as:

$$\varepsilon_{FC} = \varepsilon_H \times \varepsilon_T \times \varepsilon_J \times \varepsilon_V$$

1.3. Overpotential - Polarization.

In the paragraph describing the voltage efficiency, it can be easily seen that important parameters intrinsic to the cell (such as the cell materials) have a strong influence on the cell voltage. By considering the difference between the operating cell voltage, *E,* and the expected reversible cell voltage, E_r, it is possible to clearly see the contribution of each parameter to the voltage change. This difference $\eta = E - E_r$ is called the overpotential or polarization.

The polarization of a cell cannot be suppressed but should be minimized by choosing the right materials and cell design. The total polarization is the sum of four types of polarizations described in the following paragraphs. The effect of each polarization can be seen in the polarization curve presented in Figure 2.

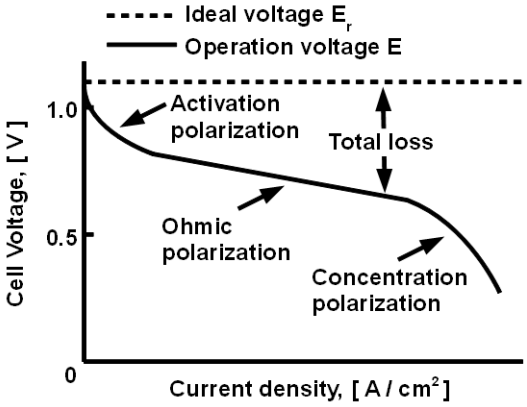

Figure 2. Polarization curve of a SOFC.

1.3.1. Charge transfer or activation polarization.

To start a chemical or an electrochemical reaction, an energy barrier must be overcome by the reacting species. This energy barrier or activation energy results in activation or charge transfer polarization η_A. The activation polarization is related to the current density i by the Butler-Volmer equation:

$$i = i_0 \exp\left(\frac{\beta_a \eta_A F}{RT}\right) - i_0 \exp\left(\frac{\beta_c \eta_A F}{RT}\right)$$

where i_0 is the exchange current density, β are the symmetry coefficients, F is the Faraday constant, R is the gas constant and T is the temperature.

1.3.2. Reaction polarization.

When the rate of the electrode process is influenced by a chemical reaction, a reaction polarization term η_R appears.

1.3.3. Resistance or ohmic polarization.

The resistance of diffusing ions through the electrolyte, the resistance of electrons through the electrodes and the current collectors and the contact resistance between the cell components cause the ohmic polarization, η_Ω, given by:

$\eta_\Omega = i\mathrm{R}$

where i is the current density, R is the total ohmic resistance of the cell.

1.3.4. Diffusion or concentration polarization.

When the supply of reactants to the electrode and/or when the removal of the reaction products from the electrode is slower than that corresponding to the charging / discharging current, i, mass transport effects becomes limiting and causes diffusion or concentration polarization, η_D. When the electrode process is completely governed by diffusion, the limiting current, i_L, is reached. For an electrode process free of activation polarization, the diffusion polarization is given by:

$$\eta_D = \frac{RT}{zF}\ln\left(1-\frac{i}{i_L}\right)$$

where F is the Faraday constant, R is the gas constant, T is the temperature, i the current and i_L is the limiting current which is given by:

$$i_L = \frac{zFD\Delta c_M}{\delta}$$

where D is the diffusion coefficient of the reacting species, c_M the concentration of the reacting species and δ is the thickness of the diffusion layer.

Finally, the total polarization or overpotential can be expressed as:

$$\eta = \eta_A + \eta_R + \eta_\Omega + \eta_D$$

By choosing the right materials and the proper microstructures for the different layers of the SOFC, the polarization can be decreased and the power output of the SOFC can be maximized. As shown previously, each

part of the fuel cell is giving a contribution to the polarization. Figure 3 shows the contribution of each part of the SOFC to the polarization resistance as a function of temperature. From this figure, it becomes evident that the cathode has the most important contribution to the overall polarization, especially when the SOFC working temperature decreases. Important improvements can be achieved when the polarization of the cathode is decreased. Improving the cathode by finding new materials with lower polarization resistance and optimizing the microstructure will be the main aim of this thesis.

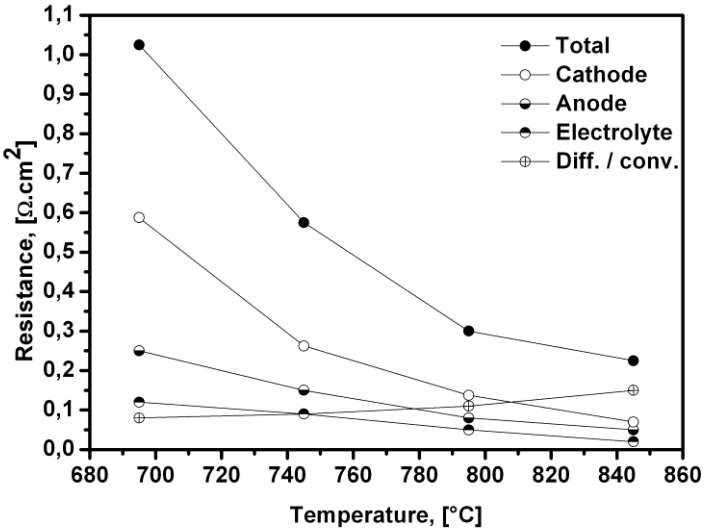

Figure 3. Contribution of each part of a SOFC to the polarization resistance as function of temperature (adapted from Linderoth S. presentation during Real SOFC Summer School, 2007)

1.4. Materials for SOFC.

In the past 20 years, a significant amount of research on SOFC's was carried out: over 6300 articles are listed in Web of Science with SOFC as keyword. Research efforts can be divided in three main topics, all geared at making SOFC technology competitive with existing energy technologies:
- Decrease costs, using cheaper raw materials and reducing manufacturing costs.
- Produce high performance cells and thus be able to lower the working temperature of the SOFC, moving from an electrolyte supported cell to anode supported cell design, using other materials as cathode.
- Increase durability and reliability, understand and decrease the degradation processes. One of the main degradation processes concerns the poisoning of the cathode material by chromium species evaporating from the stainless steel interconnects of the SOFC.

Various reviews [3-4] are available in literature. They give a full overview of the research on the materials used for the cell (electrolyte and electrodes), the other stack components (interconnects, coatings, sealants) and the manufacturing technologies. In the following paragraphs, a brief overview of the main materials used for the anode, electrolyte and cathode will be given.

1.4.1. Anodes.

In a planar SOFC design, the anode acts most of the time as substrate for the whole cell. The requirements for the anode are thus:
- good mechanical stability,
- good electrical conductivity,
- good gas permability
- good electrocatalytic conversion of the fuel with fine and homogeneous microstructure.

The most common anode material is a Nickel/Yttria Stabilized Zircania (YSZ) cermet. Nickel Oxide is dispersed in an YSZ matrix, reduced to Ni during the startup of the cell and serves as a catalyst for the hydrogen oxidation. The YSZ matrix meets all the other requirements and matches the thermal

expansion coefficient (TEC) between the Nickel and the other elements of the cell.

Other materials are used to improve this state of the art anode. For costs reduction, Ni/Al_2O_3 and Ni/TiO_2 cermets were tried as substrate in combination with a Ni/YSZ anode active layer [5-6]. Severe interaction between the two layers was observed and the electrochemical performance was decreased.

The Ni/YSZ cermet presents two major drawbacks. When the fuel gas is natural gas, sulfur impurities are contained in the fuel and poisoned the anode. Moreoever, when the fuel contains an insufficient amount of water, the internal reforming can lead to coking in the anode. Different materials were studied [7] to solve this problems, $(Sr,La)TiO_3$, $(Sr,Y)TiO_3$, $(La,Sr)(Cr,Mn)O_3$, $(La,Sr)CrO_3$, $(La,Sr)(Al,Mn)O_3$, $(La,Sr)(Ti,Mn)O_3$ but the cell performance was always much lower than the conventional Ni/YSZ cermet. These materials lacked electronic conductivity, or ionic conductivity or electrocatalytic activity. Improving these anodes using ceramic composites or the addition of small amounts of catalysts is a possible path to improve the performance. Various combinations are suggested $(Sr,Y)TiO_3$/YSZ/Ru, $(Sr,Y)TiO_3$/YSZ/Ni, $(Sr,La)TiO_3$/YSZ/Pd–CeO_2, (Sr,La)TiO3/Ni/YSZ [8-11]. These compositions showed improved sulfur tolerance and stability with respect to coking when natural gas is used as fuel.

1.4.2. Electrolytes.

In case of a planar anode supported cell, the electrolyte can be a thin film deposited on the porous anode. The requirements for the electrolyte are:

- good ionic conductivity,
- very low electronic conductivity to avoid short between the electrodes,
- good gas tightness to avoid gas leakage between anode and cathode side,
- chemical stability with the other parts of the cell,
- thermal expansion coefficient in agreement with the other parts of the cell.

Four families of materials are widely accepted as good electrolyte candidates for SOFC's: partially cation-sustituted ZrO_2, CeO_2, $LaGaO_3$ and apatites. The substitution is mostly performed with Yttria or Scandia for ZrO_2

materials, Yttria, Samarium or Gadolinium for CeO_2 materials, Strontium and Manganese for $LaGaO_3$.

For the zirconia materials, Yttria Stabilized Zirconia (YSZ) is widely used and is the most common electrolyte used for the SOFC. For 8YSZ, ionic conductivities are in the rage 5.0 x 10^{-2} S/cm and 6.2 x 10^{-2} S/cm at 800°C and 600°C, respectively [3]. Replacing the Yttria substitution by Scandia improves the ionic conductivity by a factor two and the degradation of the electrolyte is much better [12-13].However, yttria is less scarce than scandia and hence has a lower cost. Yttria is thus a preferable option for substitute in Zirconia. One of the major problems is that the zirconia reacts with Lanthanum, an element that is very often used in the cathode materials. In this case, a barrier layer between the electrolyte and cathode must be used.

For the Ceria materials, good ionic conductivities are obtained, typically for $Ce_{0.8}Gd_{0.2}O_{1.9}$ 6.5 x 10^{-2} S/cm and 1.3 x 10^{-2} S/cm at 800°C and 600°C, respectively [3]. However above 600°C, a p-type electronic conduction is observed [14]. At low oxygen partial pressure (anode side of the cell), the n-type electronic conductivity increases because of the reduction of Ce^{4+} to Ce^{3+}. This also causes a significant lattice expansion, causing the electrolyte plate to warp in case of an electrolyte supported cell. Finally, Ceria materials are usually difficult to sinter [see chapter 2] and thus obtaining gas tight electrolytes can usually only be obtained at high sintering temperatures.

For the Lanthanum Gallate Materials, partial replacement with Strontium and Manganese ions improves the ionic conductivity to 1.1 x 10^{-1} S/cm and 1.6 x 10^{-2} S/cm at 800°C and 600°C, respectively for $La_{0.8}Sr_{0.2}Ga_{0.9}Mg_{0.1}O_{3-x}$ [3]. However, lanthanum gallate electrolytes reacts with the nickel oxide of the anode to give lanthanum nickelates [15], which deteriorates the performance of the cell. An interlayer is necessary to avoid this reaction. Moreover, gallium is also an expensive element.

For the apatite materials, the ionic conduction due to oxygen ions excess on interstitial sites is different than the ionic conduction for the three previous materials due to oxygen vacancies. The temperature dependence is thus different and this type of materials is especially interesting at working temperatures lower than 600°C [16].

On should keep in mind that, in the case of an anode supported cell, the thickness of the electrolyte can be minimized to ~ 10 µm or lower. For such a

thin layer, the ohmic loss due to the electrolyte layer is ~ 10 - 20 $m\Omega \cdot cm^2$, a value much lower than the one due to the polarization resistance of the cathode. For the electrolyte, a high ionic conductivity is thus usually not the most important parameter.

1.4.3. Cathodes.

As shown in Figure 3, the cathode gives the major contribution to the polarization resistance of the overall cells at temperatures below 800°C. Significant research efforts have been made to further improve the cathodes. The requirements for the cathode are:
- good ionic and electrical conductivity,
- stable microstructure, chemically stable with the other parts of the cell in an oxidizing environment,
- high catalytic activity for oxygen reduction reaction,
- thermal expansion coefficient in agreement with the other parts of the cell.

For SOFC working at high temperatures (800 – 1000°C), Lanthanum manganite ($LaMnO_3$) is used with substitution by Strontium or Calcium on the A-site of the perovskite ABO_3. This family of materials $(La_{1-x}Sr_x)MnO_3$ was already selected in the 1970s by Westinghouse and ABB as a good cathode candidate after examining a variety of oxide compositions for long term compatibility with YSZ at elevated temperatures [17]. LSM had also good catalytic activity towards oxygen dissociation (and surface adsorption). Surface diffusion of (charged) O_{ad} species is of importance. As LSM is an electronic conductor, the oxygen reduction reaction was restricted to the so called triple phase boundary line (TPB) at the interface between the porous cathode, the dense electrolyte and the gas phase. In order to extend the electrochemically active region in the cathode, composite materials such as LSM-YSZ were used to combine the high electronic conductivity of LSM and the high ionic conductivity of YSZ. Because of degradation problems due to chemical stability of the composites at high temperatures and chromium poisoning, a need for improved materials working at intermediate temperatures (600 – 800°C) was growing and mixed ionic-electronic conductors such as Lanthanum strontium cobaltite LSC gained attention [18].

This family of material has very good electronic and ionic conductivity, 1600 and 0.22 S/cm respectively for $La_{0.6}Sr_{0.4}CoO_{3-x}$ at 800°C according to Teraoka [19] and Ullmann [20]. With mixed ionic electronic conductors, the electrochemically active area for oxygen reduction is increased because the surface of all perovskite grains is available for oxygen reduction [21]. However, the high thermal expansion coefficient (TEC) of ~ 20 x 10^{-6} K^{-1} in comparison to other parts of the SOFC (TEC ~ 12 x 10^{-6} K^{-1}) and the reactivity between LSC and YSZ at temperatures higher than 800°C poses a serious problem for these materials.
This reaction can be suppressed by introducing a ceria interlayer between the cathode and electrolyte [22]. Partially substituting cobalt by iron (from $La_{0.6}Sr_{0.4}CoO_{3-x}$ to $La_{0.6}Sr_{0.}4Co_{0.2}Fe_{0.8}O3_{-x}$) on the B-site of the LSC perovskite decreases the high TEC from 20 to 15.3 x 10^{-6} K^{-1}. Both electronic and ionic conductivity remain high, 330 and 0.008 S/cm, respectively at 600°C [20,23]. A large variety of materials can be explored by changing the elements on A- and B-sites of the perovskite and by varying the concentrations of these elements. For the perovskite, the composition $Ba_{0.5}Sr_{0.5}Co_{0.8}Fe_{0.2}O_{3-x}$ (BSCF) shows extremely high oxygen ion mobility but a too large thermal expansion coefficient. However, application of this material in SOFCs is prohibited because of its high TEC and of its severe performance degradation in CO_2 containing atmosphere (formation of barium carbonate) [24-25]. A good overview of the thermal expansion coefficient, electronic and ionic conductivities of the most important perovskites is given by Sun et al. [4].

In the past years, more complex structures such as double perovskites have been investigated [26-29] but no significant improvement has been shown yet. Materials with a K_2NiF_{4+x} –type structure, so-called Ruddlesden-Popper phases, consist of alternating layers of perovskite $(KNiO_3)^-$ and rocksalt $(KO)^+$. These materials show both very high oxygen exchange kinetics and very high ionic conductivity. However, the ionic conductivity is highly anisotropic and the electronic conductivity is relatively low [30-34]. The first tests of these materials as cathode for SOFC gave a good performance, especially for fuel cells working at intermediate working temperatures.

2. Scope of this thesis.

As described in this introduction, improving the cathode is one of the main challenges to have Solid Oxide Fuel Cells working at intermediate temperatures (600 – 800°C). At these temperatures, the different degradation mechanisms (chromium poisoning, microstructure instability, chemical instability of the materials of the cell, interconnects, sealing's, etc…) should be slower. The performance of the SOFC should thus decrease at an acceptable rate during the expected lifetime of 40.000 hours. Most of the work presented in this book concerns the cathode, as the polarization resistance of this layer is the most important of the cell at the intermediate temperatures.

In chapter 1, a description of the different deposition techniques, of the characterization techniques and of the experimental setup is given.

In chapter 2, a study on the interlayer material Cerium Gadolinium Oxide (CGO) is presented. The main problem of this material is the requirement for high temperature sintering to get dense layers. A technique is shown to reduce the sintering temperature but also to improve the oxygen diffusion through CGO.

In chapter 3, a simple microstructure is used for two cathode materials. Thin dense layers prepared by Pulsed Laser Deposition are tested to distinguish bulk diffusion from surface diffusion for these materials. The effect of the current collector is discussed.

In chapter 4, the real state-of-the-art porous cathode $La_{0.6}Sr_{0.}4Co_{0.2}Fe_{0.8}O3_{-x}$ is tested. The effect of the microstructure on the polarization resistance is shown and modeling of the impedance data is performed with different equivalent circuits taken from literature or developed by the authors.

In chapter 5, an attempt to improve the performance of LSCF cathodes is presented. By tuning the electrolyte / electrode interface, the performance of the whole electrode is improved. A discussion on the reasons for this improvement is given.

In chapter 6, Lanthanum nickelate La_2NiO_{4+x} as cathode material is presented. Different microstructures are tested by mean of electrochemical impedance spectroscopy. The microstructure presented in chapter 4 for LSCF is also tested.

In chapter 7, a discussion on the possibility to use Pulsed Laser Deposition to deposit all layers of a SOFC is presented.

References.

[1] IPCC third assessment report, 2001, www.ipcc.ch

[2] Carcassi M.N., Fineschi F., Energy 30 (2005) 1439.

[3] Menzler N.H., Tietz F., Uhlenbruck S., Buchkremer H.P., Stoever D., J. Mater. Sci., 45 (2010) 3109.

[4] Sun C., Hui R., Roller J., J. Solid State Electrochem., 14 (2010) 1125.

[5] Tietz F., Dias F.J., Naoumidis A. (1998) In: Stevens P. (ed) Proc. 3rd Eur. SOFC Forum, vol 1. Eur. Fuel Cell Forum, p 171.

[6] Meschke F., Dias F.J., Tietz F., J. Mater. Sci. 36 (2001) 5719.

[7] Atkinson A., Barnett S., Gorte R.J., Irvine J.T.S., McEvoy A.J., Mogensen M., Singhal S.C., Vohs J., Nat. Mater. 3 (2004) 17.

[8] Kurokawa H., Yang L.M., Jacobsen C.P., De Jonghe L.C., Visco S.J., J. Power Sources 164 (2007) 510.

[9] Fu Q.X., Tietz F., Sebold D., Tao S.W., Irvine J.T.S., J. Power Sources 171 (2007) 663.

[10] Kim G.T., Gross M.D., Wang W.S., Vohs J.M., Gorte R.J., J. Electrochem. Soc. 155 (2008) B360.

[11] Pillai M.R., Kim I.W., Bierschenk D.M., Barnett S.A., J. Power Sources 185 (2008)1086.

[12] Yamamoto Y., Arati Y., Takeda Y., Imanishi N., Mizutani Y., Kawai M., Nakamura Y., Solid State Ionics 79 (1995) 137.

[13] Haering C., Roosen A., Schichl H., Schnoeller M., Solid State Ionics 176 (2005) 261.

[14] Blumenthal R.N., Prinz B.A., J. Appl. Phys. 38 (1967) 2376.

[15] Huang K., Tichy R.S., Goodenough J.B., J. Am. Ceram. Soc. 81 (1998) 2581.

[16] Nakayama S., Sakamoto M., J. Eur. Ceram. Soc. 18 (1998) 1413.

[17] Steele B.C.H., Heinzel A., Nature 414 (2001) 345.

[18] Yamamoto O., Takeda Y., Kanno R., Noda M., Solid State Ionics 22 (1987) 241.

[19] Teraoka Y., Zhang H.M., Okamoto K., Yamazoe N., Mater. Res. Bull. 23 (1988) 51.
[20] Ullmann H., Trofimenko N., Tietz F., Stoever D., Ahmad-Khanlou A., Solid State Ionics 138 (2000) 79.
[21] Adler S.B., Lane J.A., Steele B.C.H., J. Electrochem. Soc.143 (1996) 3554.
[22] Chen C.C., Nasrallah M.M., Anderson H.U., Alim M.A., J. Electrochem. Soc. 142 (1995) 491.
[23] Tai L.W., Nasrallah M.M., Anderson H.U., Sparlin D.M., Sehlin S.R., Solid State Ionics 76 (1995) 273.
[24] Yan A., Cheng M., Dong Y.L., Yang W.S., Maragou V., Song S.Q., Tsiakaras P., Appl. Catal. B 66 (2006) 64.
[25] Bucher E., Egger A., Caraman G.B., Sitte W., J. Electrochem. Soc. 155 (2008) B1218.
[26] Martin C., Maignan A., Pelloquin D., Nguyen N., Raveau B., Appl. Phys. Lett. 71 (1997) 1421.
[27] Taskin A.A., Lavrov A.N., Ando Y., Appl. Phys. Lett. 86 (2005) 091910.
[28] Kim G., Wang S., Jacobson A.J., Yuan Z., Donner W., Chen C.L., Reimus L., Brodersen P., Mims C.A., Appl. Phys. Lett. 88 (2006) 024103.
[29] Kim J.H., Cassidy M., Irvine J.T.S., Bae J.M., J. Electrochem. Soc. 156 (2009) B682.
[30] Takeda Y., Nishijima M., Imanishi N., Kanno R., Yamamoto O., Takano M., J. Solid State Chem. 96 (1992) 72.
[31] Skinner S.J., Kilner J.A., Solid State Ionics 135 (2000) 709.
[32] Boehm E., Bassat J-M., Dordor P., Mauvy F., Grenier J-C., Stevens P., Solid State Ionics 176 (2005) 2717.
[33] Munnings C.N., Skinner S.J., Amow G., Whitfield P.S., Davidson I.J., Solid State Ionics 176 (2005) 1895.
[34] Sayers R., De Souza R.A., Kilner J.A., Skinner S.J., Solid State Ionics 181 (2010) 386.

Chapter 1:

Experimental considerations.

The microstructure of each of the SOFC components, anode, cathode and electrolyte, has a significant effect on the performance of the cell. In the next paragraphs, experimental considerations will be discussed, and the deposition techniques used to deposit the different layers and also the characterization techniques are presented.

1. Deposition techniques.

For the work described in this thesis different deposition techniques have been used to produce thin films. Screen printing and tape casting are two traditional techniques used to produce SOFCs. Screen printing is a technique used to deposit the interlayer and the porous cathodes of cells characterized in this work. Tape casting is used to produce the substrate of the cells characterized in this work, either the electrolyte of symmetrical cells, or the anode of anode supported cells.

Pulsed laser deposition is also used in this work in order to obtain special microstructures. This last technique is mainly used to gain insights into materials properties but also to improve the performance of the SOFCs. The experimental Pulsed Laser Deposition setup consists of a KrF excimer laser with a wavelength of 248 nm, a maximum pulse energy of 700mJ and a repetition rate between 1 and 50 Hz. For a better homogeneity and control of the plasma, a mask is used to shape the beam profile. The laser beam enters the vacuum chamber (base pressure P = 10^{-7} mbar) after being focused with a lens on a rotating target of the material that is to be deposited. The beam hits the target at a 45° angle with a spot size varying between 1 and 5 mm^2, depending on the desired fluence and plasma expansion dynamics. During the deposition, oxygen, argon and nitrogen can be introduced as background gas and the pressure in the vacuum system is controlled at the desired value, typically between 10^{-2} and 1 mbar. The target - substrate separation can be adjusted to the desired distance between 35 and 90 mm. Targets of different materials are placed on a chariot in order to be able to deposit different materials in one run. The substrate is clamped onto a heater in order to control the deposition temperature between room temperature and 950°C. After deposition, oxygen background pressure is

fixed to 100 mbar and the temperature of the heater is brought back to room temperature with a ramp of 1°C/min.

2. Characterization techniques.

Building the electrochemical cell of a SOFC consists of depositing thin layers of different materials on top of each other using the deposition techniques described in the previous paragraph. Surface morphology, cross sections, crystallinity, composition, and performance of the deposited materials are checked by using Scanning electron microscopy (SEM), X-Ray Diffraction (XRD), Transmission Electron Microscopy (TEM), Scanning Photoelectron Spectroscopy (XPS), Low Energy ion Scattering Spectroscopy (LEIS) and Electrochemical Impedance Spectroscopy (EIS).

EIS is used to measure the electrical performance of the cells and to characterize the processes that are occurring in the cells. The basic principle of EIS is to measure the impedance of a system by applying a single-frequency voltage or current to the interface and measure the phase shift and the amplitude (or the real and imaginary parts) of the resulting response at that frequency. The analysis of the response is done by using either an analog circuit or fast Fourier transform. It is possible to measure the impedance of a system as a function of frequency. Impedance spectroscopy can thus be used to study any property that influences the conductivity of an electrode or materials system. Materials properties can be obtained: conductivity, dielectric constant, mobilities of charges, equilibrium concentrations of charged species, bulk generation-recombination rates are examples. Information about the electrode / electrolyte interface can also be obtained: adsorption-reaction rate constants, capacitance of the interface region, diffusion coefficient of species in the electrode are examples.
This technique has been used extensively, not only to measure the performance of the cell, but also to gain understanding of the processes occurring in the cells. A special section is thus devoted to this technique.

3. Experimental set-up.

The experimental set-up is adapted from the experimental set-up presented by Baukje de Boer [1]. The set-up was originally built to test anodes of Solid Oxide Fuel Cells. It was adapted to test cathodes of SOFCs, it is suitable to perform impedance and polarization measurements as a function of gas conditions (especially pO_2), temperature and polarization. Figure 1 shows a diagram of the different important parts of the experimental set-up.

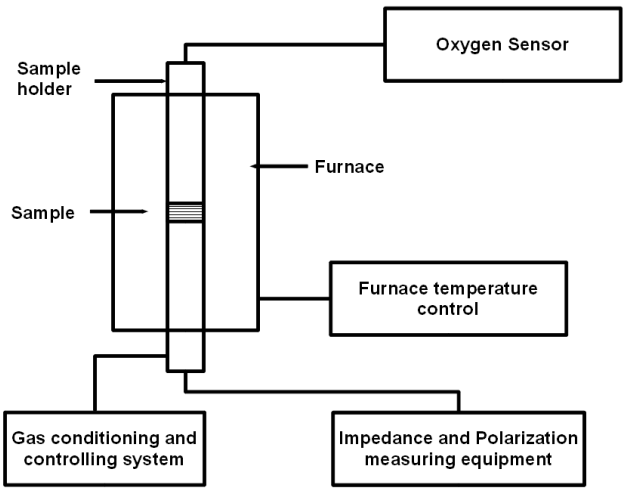

Figure 1. Overview of the experimental set-up.

The electrochemical cell is designed to be able to perform half cell measurements. As the study of this book will mainly concentrate on the study of the cathode of the SOFCs, there is no need to operate in a fuel cell mode. Half cell measurements on cathodes do not need the presence of a hydrogen chamber and an oxygen chamber with gas tight sealing.

Impedance measurements are performed in a two-terminal mode for symmetric cells which are composed of identical cathodes on both sides of a thin electrolyte. This allows the characterization of the electrodes as function of temperature and partial pressure at zero bias. To study the electrode properties also as function of applied potential a three electrode set-up is used. Here a thick electrolyte pellet is used which is provided with a groove at half height for placement of the reference platinum electrode. On both flat

surfaces similar electrodes are deposited. The electrode under investigation is called the working electrode; its potential is controlled with respect to the reference electrode (Pt/ambient pO_2). The opposite or counter electrode provides the current for the working electrode. It is important that the polarization resistances of both electrodes are reasonably close, which is achieved by using similar configurations. A large unbalance in the polarization resistance can cause a distortion of the measured electrode impedance [2]. Using the same material for both sides has the advantage that in a single cell two different electrodes can be studied. Switching the working electrode for the counter electrode and visa versa allows the characterization of the opposite electrode.
For measurements under bias it is important to correct the applied potential for the voltage drop between reference and working electrode which is due to the electrolyte resistance.

The ceramic sample holder has an open structure to allow gas flow from and to the electrodes. A Pt/Pt-10%Rh thermocouple is placed near the electrode for temperature monitoring of the sample. Pt grids or Au grids are used as current collectors. These grids are connected to Pt wiring for connection between the current collector and the BNC cables. Good electrical contacts between the electrodes and the current collectors are obtained by placing a weight of 325g above the test cell. The ceramic sample holder is placed in a quartz tube through which gas is flowing from bottom to top of the quartz tube. The measurements can be performed as function of oxygen partial pressure. The desired gas mixture is obtained by mixing nitrogen and oxygen using Brooks 5800 Mass Flow Controllers.

The quartz cell is placed in a specially designed furnace [1]. A transformer with a grounded central tab in the secondary winding is used to create a 'virtual ground' in the center position of the bifilarly wound furnace element. This reduces the background noise significantly, improving the quality of the low frequency measurements. The temperature of the furnace is controlled with a Eurotherm 2404 temperature controller. Moreover, a metallic shield connected to earth covers the quartz tube and acts as a Faraday cage. The exhaust gas is flushed through an oxygen gas sensor SYSTECH Model Zr 893/4 in order to measure the oxygen partial pressure in the quartz cell.

The impedance and polarization measurements were carried out with a Solartron 1250 Frequency Response Analyser (FRA, frequency range 0.01 – 65535 Hz) and a Solarton 1287 Electrochemical Interface (EI), which acts as a potentiostat/galvanostat. The instruments are controlled through an IEEE-bus with the commercial programs Zplot (Scribner associates) and CorrWare (Scribner associates).

4. Electrochemical Impedance Spectroscopy (EIS).

Electrochemical Impedance spectroscopy is a powerful method for characterizing electrochemical and electrical properties of materials and interfaces. Special properties of materials arising from an electrical measurement can be obtained such as chemical reaction coefficients and diffusion coefficient of species through a given medium or an interface.

Electrochemical Impedance Spectroscopy is the main technique that has been used to characterize the performance of the cells in this book. It is my intention to present a relatively brief introduction into EIS: its principles, the measurement techniques and the necessity of data validation and the analysis technique. For more detailed information on impedance spectroscopy, the reader is advised to take a close look at the book edited by Barsoukov and Macdonald [3], which provides a complete overview of the Impedance Spectroscopy technique.

4.1. Theory - Physical modeling of the system.

4.1.1. Impedance spectroscopy.

In impedance spectroscopy a small ac-perturbation (generally an ac-voltage) is applied to the cell and the response is measured (generally an ac-current). The transfer function, or impedance, is then defined as:

$$Z(\omega) = \frac{V_0 \cdot e^{j\omega t}}{I_0 \cdot e^{j(\omega t - \varphi)}} = Z_0 \left(\cos\varphi + j\sin\varphi\right) = Z_{real} + jZ_{imag}$$

where $V_0 \cdot e^{j\omega t}$ is the applied ac voltage with ω = 2π*f* and $I_0 \cdot e^{j(\omega t-\varphi)}$ the current response with a phase lag φ. Z_0 is (V_0/I_0) and is frequency dependent, with $Z_0 = \sqrt{Z_{real}^2 + Z_{imag}^2}$. These impedance relations are presented in the complex plane of Figure 2.

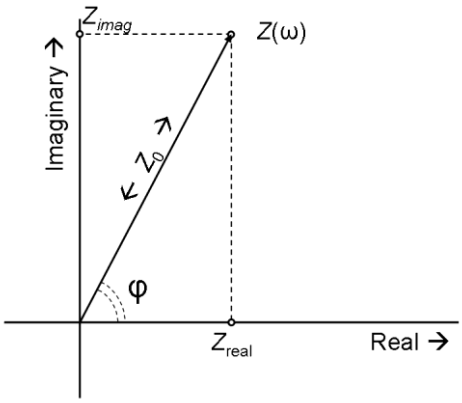

Figure 2. Representation of impedance in the complex plane.

The measurement of the impedance is performed over a wide range of frequencies, hence the term 'impedance spectroscopy'. As a simple example the impedance spectrum of a parallel combination of a resistance, *R*, and a capacitance, *C*, is presented in Figure 3. The impedance relation (or transfer function) is given by:

$$Z_{(RC)}(\omega) = \frac{1}{R^{-1} + j\omega C} = \frac{R - j\omega R^2 C}{1 + \omega^2 R^2 C^2} =$$

$$= \frac{R}{1 + \omega^2 R^2 C^2} - j\frac{\omega R^2 C}{1 + \omega^2 R^2 C^2} = Z_{real} + jZ_{imag}$$

This transfer function presents a semicircle in the complex plane which goes through the origin and has its center at the real axis at ½*R*. The top of the semicircle is given by the relation $RC\omega_{max} = 1$, with $\omega_{max}^{-1} = \tau$ is the relaxation time of the circuit. As in most cases capacitive or capacitive-like behavior is observed, it is generally accepted to plot the - Z_{imag} upward, see Figure 3.

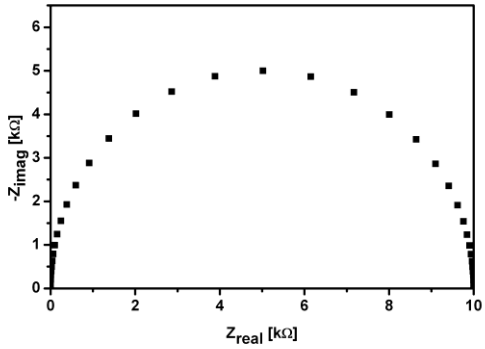

Figure 3. Impedance representation of a parallel (RC) circuit with R = 10 kΩ and C = 1 nF. Frequency range: 100 Hz – 1MHz. Fmax = 15.9 kHz.

The transfer function can be presented in several formats: impedance, dielectric, modulus or admittance. The admittance is just the inverse of the impedance and emphasizes rather the high frequency end of the spectrum, while the low frequency end is prominent in the impedance representation. The admittance representation of the parallel *RC* combination is given by:

$$Y(\omega) = \frac{1}{Z(\omega)} = \frac{1}{R} + j\omega C = Y_{real} + jY_{imag}$$

which forms a vertical straight line in the complex plane, Figure 4.

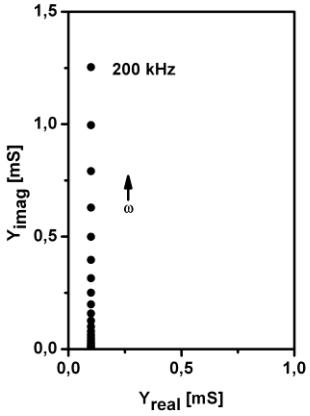

Figure 4. Admittance representation of the (RC) circuit of Figure 2. 'S' is the Siemens, the inverse of the resistance 'Ω'.

4.1.2. Processes and their representation in EIS.

4.1.2.1. Semi-infinite Diffusion - Warburg impedance.

In electrochemical impedance spectroscopy (EIS) resistances can represent various processes: ionic- and electronic conductivity, grain boundary resistance and charge transfer resistance (electrode processes). Capacitive effects result from dielectric displacement, grain boundary capacitance, electrode interface and adsorption effects at electrodes.

But in electrochemical active systems also diffusional processes can occur. The simplest form is the semi-infinite diffusion of e.g. an intercalating ion in an insertion electrode (for example Li^+ into Li_xCO_2). The transfer function can be derived directly from the Fickian laws in the case of one dimensional diffusion.

The current is given by Fick-1:

$$I(t) = -nFS\tilde{D}\left.\frac{dC(x,t)}{dx}\right|_{x=0}$$

Fick-2 gives a second relation:

$$\frac{dC(x,t)}{dt} = \tilde{D}\frac{d^2C(x,t)}{dx^2}$$

The boundary condition for $x \rightarrow \infty$ is $\lim_{x\to\infty} C(x,t) = C^0$, where C^0 is the equilibrium concentration. The activity of the mobile ion is measured at the electrode/electrolyte interface with respect to a reference electrode:

$$V(t) = V^0 + \frac{RT}{nF}\ln a(t)$$

Through the thermodynamic enhancement factor the activity is related to the concentration. When a small perturbation, ΔV, is applied the deviation from the equilibrium concentration can be used, $\Delta c(x,t) = C(x,t) - C^0$. The solution is obtained through a Laplace transformation with s as Laplace variable:

$$\Delta I(s) = -nFS\tilde{D}\left.\frac{dc(x,s)}{dx}\right|_{x=0}$$

$$\Delta V(s) = \frac{RT}{nFC^0}\left[\frac{d\ln a}{d\ln C}\right]c(x,s)\Big|_{x=0}$$

$$s\cdot c(x,s) = \tilde{D}\frac{d^2c(x,s)}{dx^2}$$

$$c(x,s)\Big|_{x\to\infty} = 0$$

The solution for the impedance in Laplace space is:

$$\frac{\Delta V(s)}{\Delta I(s)} = Z(s) = \frac{RT}{n^2F^2SC^0\sqrt{s\tilde{D}}}\left[\frac{d\ln a}{d\ln C}\right]$$

The Laplace variable can be expressed as a complex number: s = p + *j*ω, where *p* describes how the system evolves to a steady state (for *p* = 0) and ω the response to an ac-perturbation. Hence, replacing *s* by *j*ω directly yields the impedance expression:

$$Z(\omega) = \frac{RT}{n^2F^2SC^0\sqrt{j\omega\tilde{D}}}\left[\frac{d\ln a}{d\ln C}\right] =$$

$$= \frac{Z_0}{\sqrt{j\omega}} = \frac{Z_0}{\sqrt{2}}\cdot\omega^{-1/2}\left[1-j\right]$$

This semi-infinite diffusion equation is known as the Warburg impedance or transmission line impedance, the dispersion in the impedance plane is presented in Figure 5.

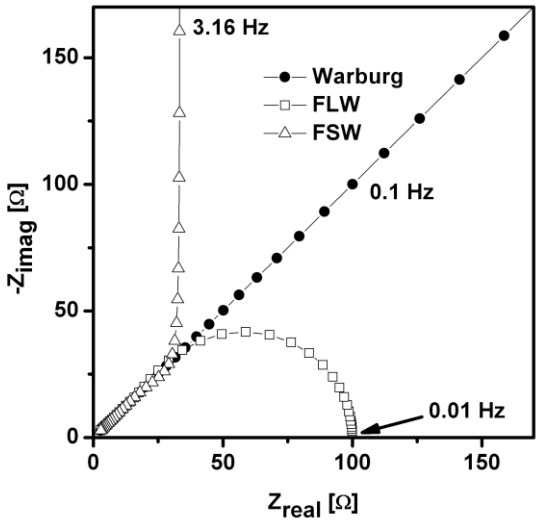

Figure 5. Impedance representations of the Warburg, Finite Length Warburg (FLW) and Finite Space Warburg (FSW). At high frequency the dispersions overlap with Z_0 = 100 Ω for all three. Argument of FLW and FSW: $d/\sqrt{\tilde{D}} = 1$.

4.1.2.2. Finite Space Warburg.

For electrochemical diffusion in a finite slab, with thickness *d*, a similar derivation can be made. The processes at the backside plane, at *x* = *d*, determine the shape of the transfer function. In case the backplane is impermeable for the mobile species the boundary condition at *x* = *d* becomes: $d\Delta c(x,t)/dx\big|_{x=d} = 0$ and the solution is the well-known 'Finite Space Warburg' (FSW) which is typical for insertion electrodes, see Figure 5:

$$Z_{FSW}(\omega) = \frac{Z_0}{\sqrt{j\omega}} \coth\left[d\sqrt{j\omega/\tilde{D}}\right]$$

4.1.2.3. Finite length Warburg.

When the concentration of the mobile species is fixed at the backside (e.g. in corrosion by the pure metal) then the boundary condition is given by:

$\Delta c(x,t)\big|_{x=d} = 0$, resulting in the 'Finite Length Warburg' (FLW), known from e.g. corrosion impedances, see Figure 5:

$$Z_{FLW}(\omega) = \frac{Z_0}{\sqrt{j\omega}} \tanh\left[d\sqrt{j\omega/\tilde{D}} \right]$$

4.1.2.4. Finite length Diffusion.

In case an exchange reaction takes place at the backplane between the ambient and the mobile species, e.g. diffusion of oxygen ions in a thin layer in contact with an ambient with oxygen, then a more complex transfer function results. The boundary condition includes the exchange reaction:

$$\tilde{D}\frac{d\Delta c(x,t)}{dx}\bigg|_{x=d} = k_{exch}\left[C_d^0 - C(x,d) \right]$$

which leads to the generic finite length diffusion equation:

$$Z_{gen.dif.}(\omega) = \frac{Z_0}{\sqrt{j\omega\tilde{D}}} \cdot \frac{\sqrt{j\omega\tilde{D}} \cdot \coth\left[d\sqrt{j\omega/\tilde{D}} \right] + k_{exch}}{k_{exch} \cdot \coth\left[d\sqrt{j\omega/\tilde{D}} \right] + \sqrt{j\omega\tilde{D}}}$$

For k_{exch} = 0 the FSW function is obtained, for $k_{exch} \rightarrow \infty$ the FLW function.

4.1.2.5. Constant Phase Elements.

So far the circuit elements have been based on fundamental principles and can be considered as 'ideal' transfer functions. A recurring phenomenological dispersion function is the 'constant phase element' (CPE). This CPE is presented in the admittance plane by:

$$Y_{CPE}(\omega) = Y_0 (j\omega)^n = \left(jY_0'\omega \right)^n = Y_0\omega^n \left[\cos\frac{n\pi}{2} + j\sin\frac{n\pi}{2} \right]$$

The parallel combination of a CPE (element symbol: 'Q') with a resistance presents a line with slope $n \cdot \pi/2$ in the admittance plane, or a depressed semicircle in the impedance plane. The CPE is a generic transfer function: for n = 1 it represents a capacitance, for n = 0 a resistance, for n = -1 an inductance and for n = ½ the semi infinite diffusion or Warburg impedance.

Figure 6 and Figure 7 show the impedance and admittance representation of a parallel combination of a CPE with a resistance.

Generally, values of *n* somewhat lower than 1 are considered as non-ideal capacitances. Values around 0.5 are assumed to represent diffusion related responses. The origin of the CPE is still not well understood, but one should realize that in most applications of EIS it is assumed that transport processes are one-dimensional where lateral influences between moving species are ignored.

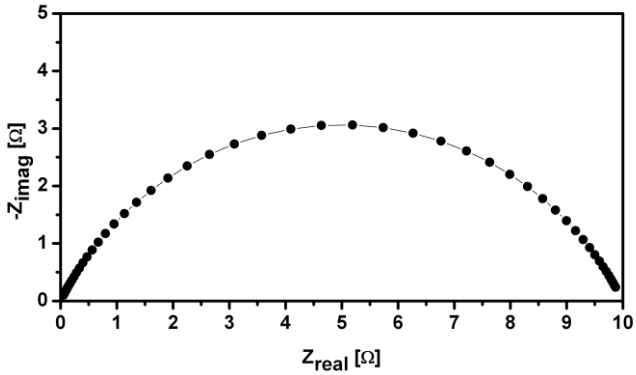

Figure 6. Impedance representation of a (RQ) combination with R = 10 kΩ and CPE: $Y_0 = 3 \cdot 10^{-8}$ S·s^n, n = 0.7.

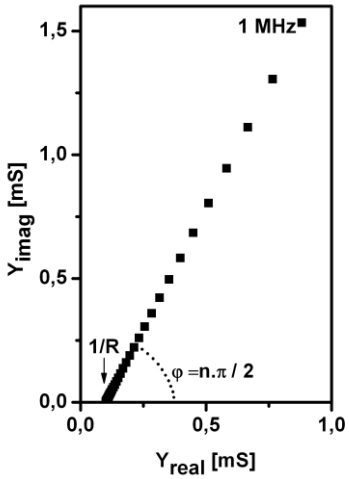

Figure 7. Admittance representation of (RQ) circuit of Figure 6.

4.1.2.6. Gerischer impedance.

Diffusion is a dominating process in the porous cathodes, but the oxygen diffusion can be influenced by various side processes, e.g. immobilization of oxygen vacancies through associate formation [4], or bulk exchange with surface diffusion [5,6]. In those cases, Fick's second law must be extended with a reaction term:

$$\frac{d\Delta c(x,t)}{dt} = \tilde{D}\frac{d^2\Delta c(x,t)}{dx^2} - k_a \Delta c$$

In case of semi-infinite diffusion the frequency domain impedance has the form:

$$Z_G(\omega) = \frac{Z_0}{\sqrt{k_a + j\omega}} = \frac{Z_0}{\sqrt{2}}\left[\sqrt{\frac{\sqrt{k_a^2+\omega^2}+k_a}{k_a^2+\omega^2}} - j\sqrt{\frac{\sqrt{k_a^2+\omega^2}-k_a}{k_a^2+\omega^2}}\right]$$

which is also known as the 'Gerischer impedance' (element symbol 'G'). An interesting aspect of this function is that the semi-infinite diffusion leads to a finite dc-resistance for ω → 0. Furthermore this function is able to model electrode behavior quite well for non-ideal porous cathode structures [7,8]. Figure 8 shows the difference between the FLW and the Gerischer impedances, the same Z_0 value (100 Ω) is used with k_a = 1 for the Gerischer and $d/\sqrt{\tilde{D}} = 1$ for the FLW.

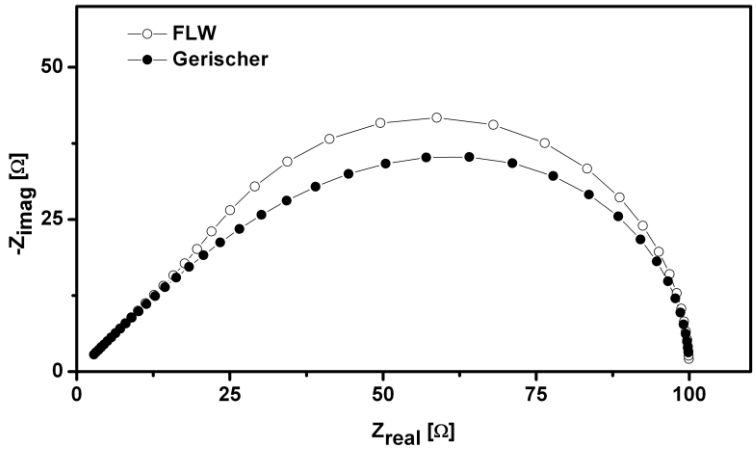

Figure 8. Comparison of the Gerischer impedance with the FLW impedance.

4.2. Data validation

A combination of the above presented elements or transfer functions in an 'Equivalent Circuit' arrangement (EqC) can be used to analyze the EIS-data, which should yield the relevant parameters describing the transfer and transport processes. With complex systems, like the porous cathodes, the determination of the correct EqC is not always straight forward. It is important to be able to distinguish between an inappropriate EqC and bad data. The Kramers-Kronig relations [9-11] provide a useful tool to validate the data. These relations state that the imaginary part is determined by the dispersion of the real part from 0 to ∞ frequency:

$$Z_{imag}(\omega) = \frac{2\omega}{\pi}\int_0^{\infty}\frac{Z_{real}(x) - Z_{real}(\omega)}{x^2 - \omega^2}\,\mathrm{d}x$$

Conversely the real part is determined, apart from a constant, R_∞, by the imaginary dispersion:

$$Z_{real}(\omega) = R_\infty + \frac{2}{\pi}\int_0^{\infty}\frac{xZ_{imag}(x) - \omega Z_{imag}(\omega)}{x^2 - \omega^2}\,\mathrm{d}x$$

These transforms are only valid when the following four conditions are met:
- *Causality*: the response must be related to the excitation signal only;
- *Linearity*: the response must scale with the excitation signal; no second harmonics may be present. Hence with inherently non linear systems like electrodes a small excitation voltage must be used in order to stay in a linear regime.
- *Stability*: the system may not change with time, i.e. it must be either in equilibrium, in a steady state condition or changing at a time scale much larger than the measurement time.
- *Finite*: for all frequencies including $\omega \rightarrow 0$ and $\omega \rightarrow \infty$. However, this condition is not essential for impedance measurements.

Especially the 'stability' is of importance for impedance measurements on SOFC electrodes. Even when the electrochemical cell has reached a stable temperature after a temperature step, it may still evolve to a new equilibrium situation by release or uptake of oxygen from the ambient. The same holds

for a change in partial pressure. When the system is still changing, this will be observed in the KK-transform test. The transforms will not match with the original data, especially in the low frequency regime. This is easily observed in a so-called residuals graph [12] where the relative differences, Δ_{real} and Δ_{imag}, are plotted versus log frequency:

$$\Delta_{real}(\omega) = \frac{Z_{real}(\omega) - KK_{real}(\omega)}{\left|KK(\omega)\right|} \text{ , and : } \Delta_{imag}(\omega) = \frac{Z_{imag}(\omega) - KK_{imag}(\omega)}{\left|KK(\omega)\right|}$$

Valid data should show a random noise distribution around the frequency axis, a clear trace with respect to the frequency axis indicates non-KK behavior. An example is presented in Figure 9 for a cathode measured shortly after temperature stabilization (lower part) and after appropriate equilibration time (upper part).

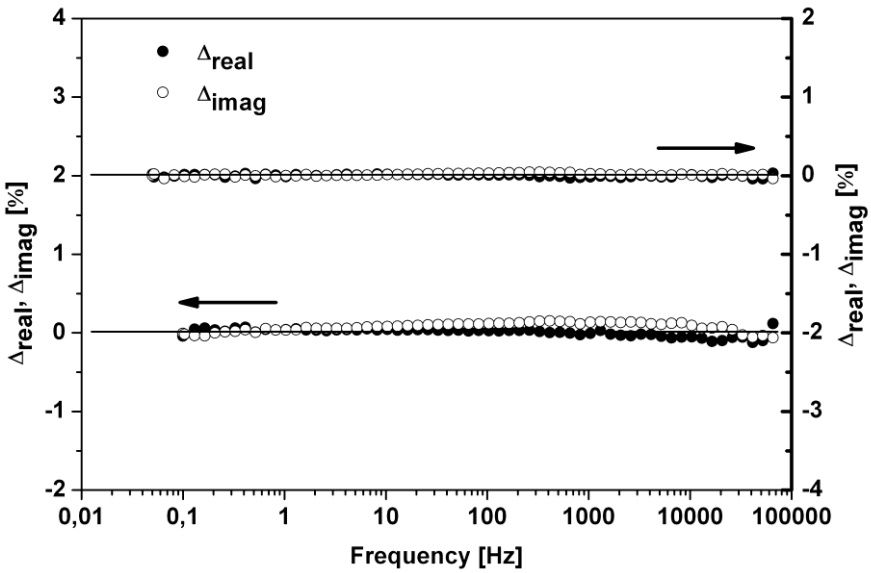

Figure 9. Residuals plot for the KK-validation of an impedance measurement shortly after temperature stabilization (lower) and after equilibration (upper).

4.3. Complex Nonlinear Least Squares Analysis.

In the past mainly simple graphical methods were available for the analysis of impedance or dielectric data [13-17]. However, as more complex systems

were studied an increasing need for advanced data analysis methods evolved. Since the eighties of the last century several computer programs were introduced that are based on a Complex NonLinear Least Squares fit algorithm (CNLLS) [18-20]. Generally an 'Equivalent Circuit' is used as modeling function whose adjustable parameters are fitted simultaneously, by minimizing an object function or error sum, *S*:

$$S = \sum_{i=1}^{N} \left\{ w_i^{'}[Z_i^{'} - Z_C^{'}(\omega_i)]^2 + w_i^{''}[Z_i^{''} - Z_C^{''}(\omega_i)]^2 \right\}$$

where $Z_i^{'}$ and $Z_i^{''}$ are the real and imaginary parts of the measured impedance at the frequencies ω_i, $Z_C^{'}(\omega_i)$ and $Z_C^{''}(\omega_i)$ are the values the real and imaginary parts of the model, $w_i^{'}$ and $w_i^{''}$ are statistical weights of the data, and the summation runs over all N frequencies used in the experiment.

Essential for the CNLLS-procedure is, besides a proper model function (EqC), an appropriate set of starting values for the adjustable parameters. A proven method to obtain these is the so-called partial-fit and subtraction procedure which allows a stepwise de-convolution of the frequency dispersion. In this method recognizable parts of the dispersion are fitted with a simple model over a limited frequency range. Subsequently the appropriate circuit elements are subtracted either in series or in parallel with the remainder. This method has the advantage that small but significant contributions to the overall dispersion become visible.

As an example this procedure is demonstrated with the impedance of a Gd-doped ceria sample with gold electrodes measured at 349°C (see chapter 2). Figure 10 shows the impedance. The high frequency semicircle is modeled with a R(RQ) circuit over a small frequency range (solid dots and line). The dispersion of the (RQ) circuit is then subtracted from the overall impedance dispersion, assuming that it can be treated as being in series with the remainder.

This results in a changed dispersion as shown in Figure 11. The dispersion shows a diffusion type low frequency slope (Warburg-like) and a high frequency semicircle which can be modeled with the well-known Randles circuit [21], see Figure 11.

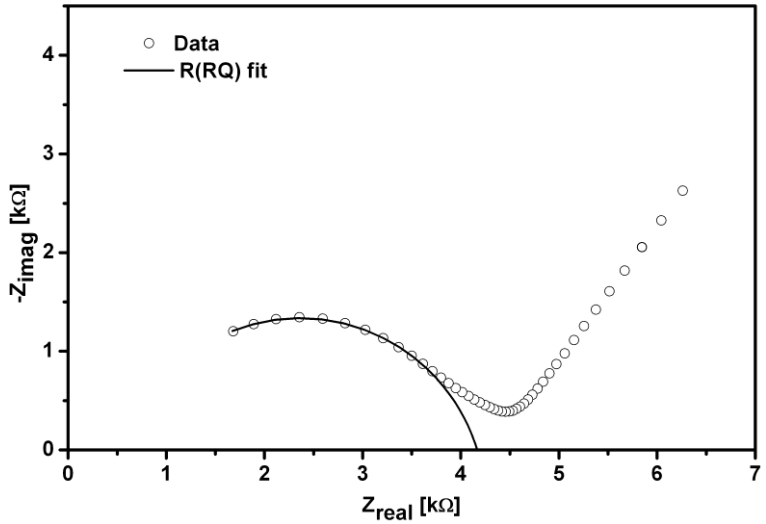

Figure 10. Impedance of an Au/CGO10/Au sample at 349°C. The high frequency arc is modeled with a R(RQ) circuit.

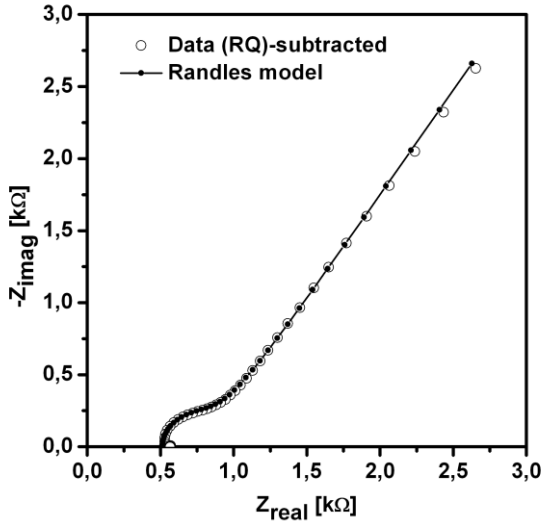

Figure 11. Dispersion after series subtraction of the (RQ) dispersion. The resulting impedance can be modeled with a Randles circuit: R(C[RQ]), solid dots and line.

This pre-analysis thus yields a set of starting parameters and a possible equivalent circuit for the CNLS-fit of the complete data set. The final result of the CNLS-fit is presented in Figure 12, together with the residuals plot (insert). The residuals plot shows, with an average error of less than 0.1%, a very good match between data and model.

Comparing the pseudo χ^2 from the K-K validation, $6 \cdot 10^{-7}$, with the χ^2 for the CNLS-fit, $1 \cdot 10^{-6}$, also indicates that the R(RQ)(Q[RQ]) model is a viable representation of the impedance. Based on the values of the parameters, Table 1, the high frequency (RQ) can be assigned to the grain boundary dispersion. The Randles circuit is assigned to a reversible electrode reaction.

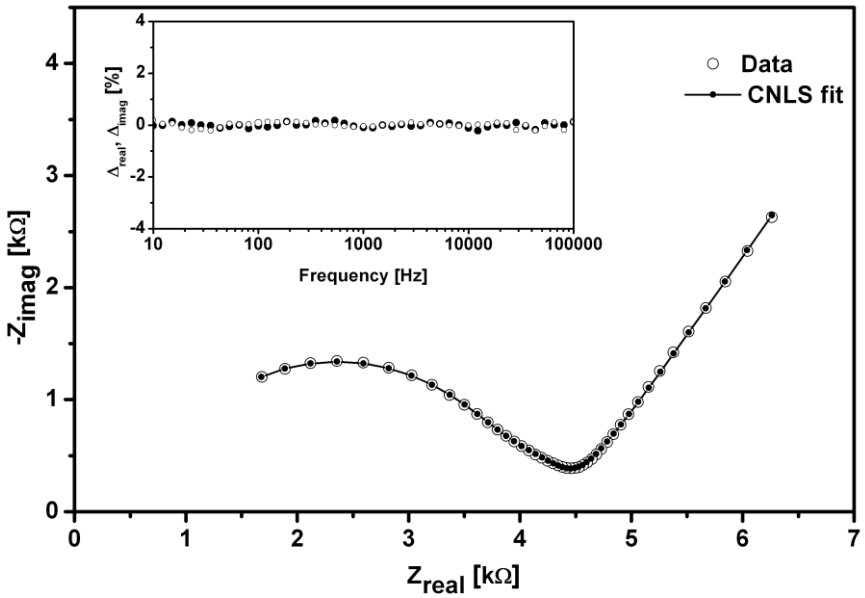

Figure 12. Original data (○) and CNLS-fit (-●-) of the Au/CGO10/Au sample at 349°C. The residuals plot is presented in the insert.

It is often possible to model the data with more than one equivalent circuit. Fletcher [22] has presented a list of different sets of EqC's that can have exact identical dispersions. But also within the experimental error different EqC's could yield virtually indistinguishable dispersions. It is of course essential that an EqC has a physical interpretation. Furthermore it should be applicable to a whole range of measurements under different conditions

(temperature, partial pressure, etc.). Sometimes it may be necessary to compare the data analysis of identical systems where one parameter has been changed, e.g. dimension, grain size, in order to obtain the most reliable EqC.

Table 1. Starting values from the pre-analysis and final parameter values of the CNLS-fit with error estimates for the dispersion of Figure 11.

Parameter	Starting values	CNLS results	Relative error [%]	Dimension
$R_{el'lyte}$	513	648	1.4	[Ω]
R_{gb}	3610	3314	0.8	[Ω]
Q_{gb}, Y_0	$9.3 \cdot 10^{-9}$	$5.98 \cdot 10^{-9}$	3.9	$[S \cdot s^n]$
Q_{gb}, n	0.811	0.848	0.4	[-]
Q_{dl}, Y_0	$0.17 \cdot 10^{-6}$	$0.16 \cdot 10^{-6}$	15	$[S \cdot s^n]$
Q_{dl}, n	1	0.948	2.2	[-]
R_{ct}	381	503	4.7	[Ω]
Q_{diff}, Y_0	$24 \cdot 10^{-6}$	$24.8 \cdot 10^{-6}$	0.5	$[S \cdot s^n]$
Q_{diff}, n	0.615	0.606	0.17	[-]

References.

[1] Boer B. de, PhD thesis, University of Twente, 1998.

[2] Boukamp B.A., Hildenbrand N., Nammensma P., Blank D.H.A., Solid State Ionics, doi:10.1016/j.ssi.2010.05.037 (2010 on line, in press)

[3] Barsoukov E., Macdonald J.R., Impedance Spectroscopy Theory, Experiment and Applications, Second Edition, ISBN 0-471-64749-7.

[4] Boukamp B.A., Bouwmeester H.J.M., Solid State Ionics, 157 (2003) 29.

[5] Atangulov R.U., Murygin I.V., Solid State Ioncs 67 (1993) 9.

[6] Boukamp B.A., Verbraeken M., Blank D.H.A., Holtappels P., Solid

State Ionics 177 (2006) 2539.
[7] Adler S.B., Lane J.A., Steele B.C.H., J. Electrochem. Soc., 143 (1996) 3554.
[8] Lu Y., Kreller C., Adler S.B., J. Electrochem. Soc. 156 (2009) B513.
[9] Kronig R. de L., J. Opt. Soc. Am., 12 (1926) 547.
[10] Kramers H. A., Z. Phys., 30 (1929) 521.
[11] Bode H. W., Network Analysis and Feedback Amplifier Design, Chap. 14, Van Nostrand, New York (1945).
[12] Boukamp B.A., J. Electrochem. Soc., 142 (1995) 1885.
[13] Cole K.S., Cole R.H., J.Chem. Phys. 9 (1941) 341.
[14] Vetter K.J., Electrochemical Kinetics, Academic Press, New York, 1967.
[15] Macdonald J.R., J. Electroanal. Chem., 53 (1974) 1.
[16] Macdonald J.R., J. Chem. Phys., 61 (1974) 3977.
[17] Böttcher C.J.F., Bordewijk P., Theory of Electric Polarization, Vol.II, Dielectrics in Time-Dependent Fields, Elsevier, Amsterdam, 1978.
[18] Macdonald J.R., Impedance Spectroscopy Emphasizing Solid Materials and Systems, Wiley, New York, 1987.
[19] Macdonald J.R., Schoonman J., and Lehnen A.P., J. Electroanal. Chem., 131 (1982) 77.
[20] Boukamp B.A., *Solid State Ionics*, **20** (1986) 31.
[21] Randles J.E.B., *Discuss. Farad. Soc.* **1** (1947) 11.
[22] Fletcher S., *J.Electrochem.Soc.* 141 (1994) 1823.

Chapter 2.

Characterization of Gadolinium Doped Ceria as electrolyte for SOFC.

Abstract.

The effect of the complexing agent during the synthesis of $Ce_{0.9}Gd_{0.1}O_{2-\delta}$ via a complexation route is shown. A small amount of Fe loading (0.5 at.%) is used as a sintering agent to reduce sintering temperature and improve electrochemical behavior. The iron additive is introduced in two different ways, either via ball milling of iron oxide with CGO ceramics or via addition of iron nitrate directly during the synthesis of CGO ceramics. This last route is a novel way of mixing the sintering agent with the CGO ceramics.

Introducing iron oxide by ball milling reduced the sintering temperature by at least 100°C and up to 300°C when compared to pure samples. Introducing the iron during the synthesis of CGO even further decreases the sintering temperature. With the introduction of iron, smaller grain growth is observed. The electrical behavior is strongly depending on the complexing agent used during the synthesis, but also on how the iron addititive is introduced. With this introduction, bulk and grain boundary conductivity are affected in a different way for the two complexing agents.

1. Introduction.

Solid Oxide Fuel Cells (SOFCs) are attractive systems because of their high efficiency and their zero or very low emission of pollutants. SOFCs consist of three important parts: a cathode, an electrolyte and an anode. The most standard solid oxide electrolyte is yttria stabilized zirconia (YSZ). At temperatures above 900°C, it presents a very high oxygen ionic conductivity in both oxidizing and reducing atmosphere and good mechanical properties. However, for reasons related to fabrication costs and long term stability of SOFCs, it is important to decrease the operation temperature down to 500-700°C, so called intermediate-temperature as defined by Steele [1]. An increased electrolyte ionic conductivity is thus one of the requirements to reach these lower operation temperatures.

Different materials are investigated to replace YSZ, such as ceria-based oxides, lanthanum-gallate-based oxides and bismuth-based oxides. Ceria based oxides were found to be a very promising electrolyte since their ionic conductivity is higher than YSZ in the intermediate temperature regime. It can be further increased with the use of dopants such as Ca^{2+}, Sr^{2+}, Y^{3+}, Gd^{3+} and Sm^{3+}, different dopant concentrations and different ways to introduce the dopant can be used [2-6]. Butler et al. [7] showed that the ion size has a major effect on dopant-vacancy interactions in fluorite oxides, thus also in ceria based oxides. The minimum binding energy was calculated to be for Gd^{3+} which makes gadolinium doped ceria (CGO) a strong candidate for fast ionic conductivity.

However, ceria-based oxides are known to be unstable in reducing environment (e.g. on the anode side of SOFC). The reduction of CGO leads to the increase of the electronic conductivity, which lowers the open circuit voltage of the SOFC. This problem can be overcome by introducing a thin YSZ layer between the anode and the CGO. Another problem is the difficulty to densify ceria-based oxides below 1500°C [8-9]. Some transition metal oxides, such as cobalt, copper, manganese, iron and nickel oxides are known to be effective sintering aids for the densification of ceria-based sample [10-12] and it was shown that the sintering temperatures can be

decreased below 1000°C by addition of small quantities (typically 0.5 mol.% $FeO_{1.5}$) of transition metal oxides (TMO).

In several contributions [11, 13, 14, 15], it was also shown that the addition of some transition metals not only decreases the sintering temperature but also can modify the electrochemical behavior in ceria ceramics. Kleinlogel et al. [13] investigated the electrochemical properties of nanosized ceria solid solutions by adding small amounts (< 5 mol.%) of Co_3O_4. They did not obtain any Co_3O_4 rich grain boundary layer which might block ionic conduction, although for low oxygen partial pressure the material becomes a mixed ionic-electronic conductor due to partial reduction of Ce^{+4} to Ce^{+3}. Fagg et al. [14] observed that CGO containing small amounts (~2 mol.%) of Cu, Co and Fe oxides exhibit similar conductivity values with pure CGO.
However, Zhang et al. [11] reported that the additions of Fe and Mn oxides had very small effect on the grain boundary behavior while the addition of Co oxide exhibited a slight decrease in the grain boundary conductivity compared to pure CGO, indicating as well a small decrease in the lattice conductivity, probably due to the dissolution of TMOs in CGO crystallites. In a later publication, Zhang et al. [15] performed impedance measurements on pure CGO and modified CGO with 0.5 mol.% Fe_2O_3. In the impedance plot, they reported that the grain boundary arc of the modified CGO with 0.5 mol.% Fe_2O_3 was much smaller than that of the pure CGO. In pure CGO, impurities were forming a thin layer in the grain boundaries prohibiting a good oxygen ionic transport. On the contrary, CGO modified with Fe_2O_3 showed a higher grain boundary ionic conductivity, which was confirming their previous observation [11] of the scavenging effect of Fe_2O_3 on SiO_2 impurities. The addition of the iron oxide had no effect on the lattice conductivity, since the bulk conductivity for both modified and pure CGO was identical.

In this contribution, soft chemistry complexation routes are used to synthesize CeO_2-10%Gd_2O_3 nano-powders (CGO10). The effect of different parameters is shown: the type of complexing agent, the concentration of the rare earth element during the complexation route, the addition of iron as sintering additive and the way to introduce the sintering additive. Citric acid and ethylene glycol are used as complexing agent, 0.5 at.% $FeO_{1.5}$ is

introduced as sintering agent either as iron oxide in a ball milling step with CGO powders, or directly during the CGO synthesis as iron nitrate. Those parameters directly influence the densification behavior of CGO ceramics and the electrochemical behavior.

2. Experimental.

2.1. Synthesis of CGO powders.

The CGO powders were synthesized by two different complexation methods, using either citric acid, or ethylene glycol as a complexing agent. Iron was used as a sintering additive, it was added either after the synthesis of CGO powders during ball-milling step, or directly during the synthesis of CGO (further denoted by in situ addition of iron oxide). The CGO powders were then pressed into pellets using first a uniaxial press and an isostatic press at a final pressure of 0.4 GPa. All the samples were finally sintered together in an alumina boat at 800°C and their density was measured using an Archimedes method in water. This procedure was reproduced after sintering at 900°C, 1000°C, etc… until 1500°C or until the relative density of the CGO pellet was higher than 94%. This method could give a quick overview of the sintering behavior for all the samples. One must keep in mind that the results from this method can also deviate from a single sintering step at the right sintering temperature.
For all those samples, NAME_A means that no sintering agent is used; NAME_B means that 0.5 at.% Fe as iron oxide was added during ball-milling; NAME_C means that 0.5 at.% Fe as iron nitrate was added during the synthesis of CGO.

2.2. Complexation route using citric acid.

Figure 1 describes schematically this method and the nomenclature for the different samples. The right amounts of cerium nitrate $Ce(NO_3)_3 \cdot 6H_2O$ and gadolinium nitrate $Gd(NO_3)_3 \cdot 6H_2O$ were dissolved in distilled water. Citric acid was added to this solution, the molar ratio rare earth element to citric acid was equal to 1.5. 5mL of nitric acid and 5mL of ammonium hydroxide were added to this solution under constant stirring. In the case of in situ

addition of iron (route_C), 0.5 mol.% of iron nitrate $Fe(NO_3)_3 \cdot 9H_2O$ was also added. The solution was then heated to 200°C for 4 hours in order to evaporate the solvent. The obtained material was then pyrolyzed at 275°C under constant air flow and finally calcined at 850°C for 6 hours. The obtained powder was ball-milled in ethanol using zirconia balls. For samples in which iron oxide is used as sintering agent, 0.5 at.% iron oxide Fe_2O_3 was added during ball-milling step (route_B). Following the ethanol evaporation, the powders were pressed into pellets and sintered according to the procedure described previously.

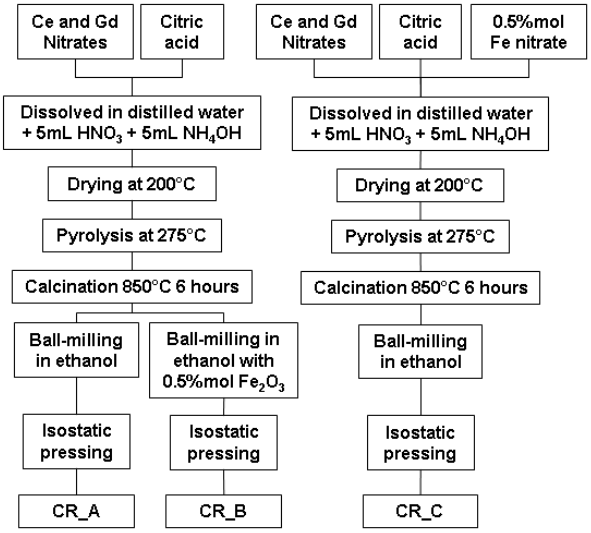

Figure 1. Schematic description of the complexation route using citric acid and nomenclature of the different samples.

2.3. Complexation route using ethylene glycol.

Figure 2 describes schematically this method and the nomenclature for the different samples. The right amounts of cerium nitrate $Ce(NO_3)_3 \cdot 6H_2O$ and gadolinium nitrate $Gd(NO_3)_3 \cdot 6H_2O$ were dissolved in distilled water. Two different cerium nitrate and gadolinium nitrate concentrations were used, either 0.63M and 0.07M respectively, or 1.89M and 0.21M respectively. The concentration in nitrates is increased by a factor of 3 in case of the high concentration complexation route. 40mL ethylene glycol and 10mL nitric acid (in case nitric acid was used) was added to the solution. In the case of in situ

addition of iron (route_C), 0.5 mol.% of iron nitrate $Fe(NO_3)_3 \cdot 9H_2O$ was also added. The complexation took place over night at 80°C. The obtained viscous solution was dried at 130°C in a stove. The obtained precursor was then calcined at 700°C for 6 hours. The obtained powder was ball-milled in ethanol using zirconia balls. For samples in which iron oxide is used as sintering agent, 0.5 at.% iron oxide Fe_2O_3 was added during ball-milling step (route_B). Following the ethanol evaporation, the powders were pressed into pellets and sintered according to the procedure described above.

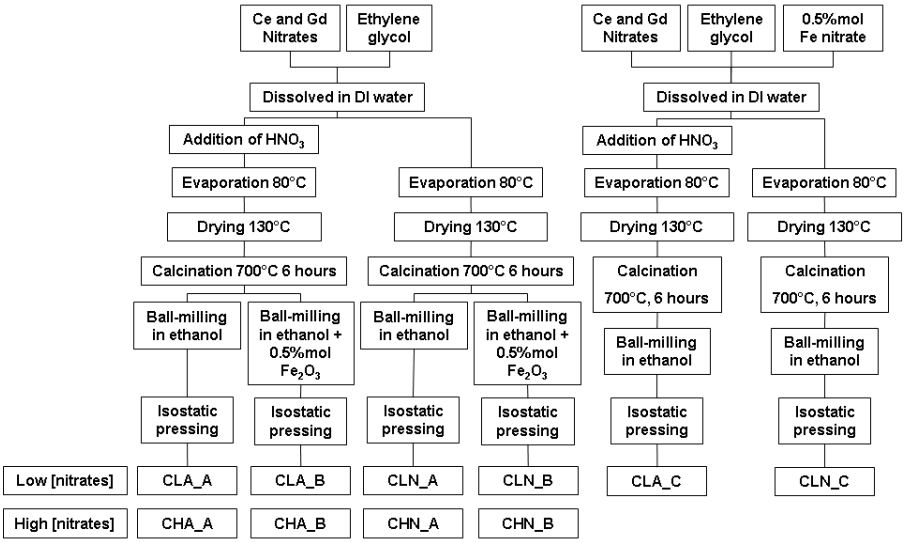

Figure 2. Schematic description of the complexation route using ethylene glycol and nomenclature of the different samples.

2.4. Characterization.

The thermal decomposition behavior of the precursor sample was studied by thermo-gravimetric analysis using a Setsys 16, Setaram. A heating rate of 5°C/min was used between room temperature and 700°C with a dwell time of 30 minutes at 700°C. The CGO phase analysis was checked by mean of X-Ray Diffraction. The crystallite size was determined by applying the Scherrer equation corrected for optical parameters of the diffractometer:
$D=K\lambda / \beta\cos\theta$ on the (111) and (220) diffraction peaks, where D is the mean crystallite size, λ is the x-ray wavelength, β is the full width at half maximum

(FWHM) of the diffraction peak, θ is the diffraction angle and K is the Scherrer constant.
The distribution and the size of the particles were measured using laser diffraction (Mastersizer 2000 Malvern). The density of the sintered samples was calculated using Archimedes method in water. The microstructures of thermally etched sintered samples were analyzed with Scanning Electron Microscopy (SEM). The lineal intercept method [16] was used to estimate the average grain size.

3. Results and Discussion.

3.1. Powder characterization.

Figure 3 shows the thermo-gravimetric curves of CGO precursor samples prepared by complexation route using ethylene glycol for two typical samples, CLA_A and CHA_A prepared at respectively low and high concentration of cerium and gadolinium. CHA samples did not show any weight loss between room temperature and 700°C whereas CLA samples showed major weight loss between 22°C and 350°C.

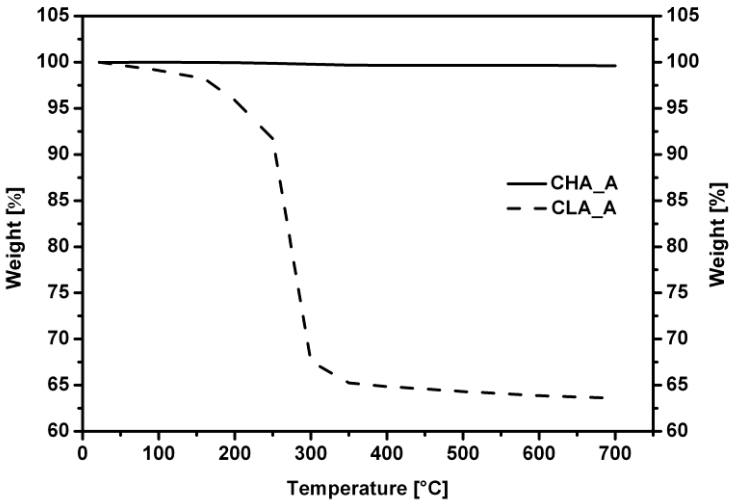

Figure 3: Thermo-Gravimetric analysis of CGO precursors from CLA_A and CHA_A synthesis routes.

During the drying process at 130°C, pyrolysis occured for sample CHA but not for sample CLA, so the combustion of organic and inorganic compounds had already occurred in sample CHA. For sample CLA, the weight loss during calcinations between 22°C and 150°C corresponds to the removal of physisorbed and chemisorbed water, the weight loss between 150°C and 350°C corresponds to the removal of organic and inorganic compounds of the precursor. At temperatures higher than 350°C, a minor weight loss is only observed. No difference in the TGA measurements could be seen between samples with and without nitric acid. As pyrolysis also occurred for samples CR, they can be compared to samples CHA.

X-Ray diffraction analysis of the different CGO powders is presented in Figure 4. Samples _B, in which 0.5 at.% Fe was added during ball-milling as iron oxide are not represented here as CGO powder is used from batch _A.
No major difference could be observed between samples _A and _C for synthesis routes CR, CHA and CHN. The expected crystal phase was obtained and the crystallite sizes were comparable between 20 and 30nm (see Table 1a).

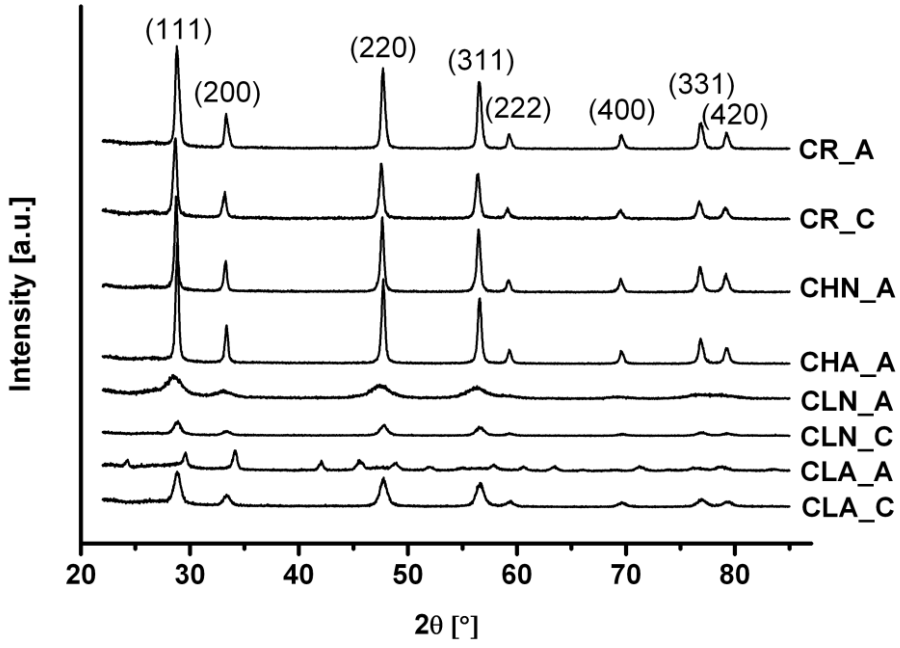

Figure 4: XRD analysis of CGO powders after calcination and ball-milling.

All CLA and CLN samples had a smaller crystallite size, between 5 and 13nm. This result was expected as no pyrolysis occurred during the drying process of samples CLA and CLN. However, CLA_A samples did not show the typical cubic fluorite structure of CGO and a second and undefined phase could be observed. Crystallites of CGO from CL routes are two to three times smaller than the crystallites of CGO from CR and CH routes.
The particle size was measured with laser diffraction. Mono-dispersed distributions were obtained for all synthesis routes. With a ball-milling step, particle size of the CGO powders was decreased to 150nm for most of the samples (see table 1).

Table 1: for all synthesis routes, crystallite size is calculated from XRD measurements using Scherrer equation; particle size is measured with laser diffraction; sintering temperature is the optimum sintering temperature to get a relative density >94%; relative density calculated with Archimedes method; average grain size of thermally etched sintered samples is measured with SEM. The sample types are described in paragraphs 2.2 and 2.3 of this chapter.

Sample type	Crystallite size (nm)	Particle size (µm)	Sintering temp. (°C)	Relative density (%)	Grain size (µm)
CR_A	20	0.5	1500	95	2.2
CR_B	20	0.14*	1200	97	0.9
CR_C	25	0.5	1200	98	0.46
CHA_A	29	0.5	1300	97	0.51
CHA_B	30	0.15*	1200	99	0.81
CHN_A	29	0.4	1500	94	1.40
CHN_B	29	0.3*	1200	94	0.37
CLA_A	6	0.5	1300	Cracked	0.40
CLA_B	6	0.18*	1200	Cracked	0.46
CLA_C	13	0.4	1200	100	0.45
CLN_A	5	0.2	1300	95	0.14
CLN_B	5	0.12*	1200	94	0.09
CLN_C	13	0.18	1100	97	0.07

3.2. Sintering behavior.

Figure 5 shows the sintering behavior of all samples, where the relative density is plotted as function of temperature. CLA_A and CLA_B samples are not shown because they cracked during the sintering procedure. The presence of a second phase in those samples is most likely the cause of the observed cracking.

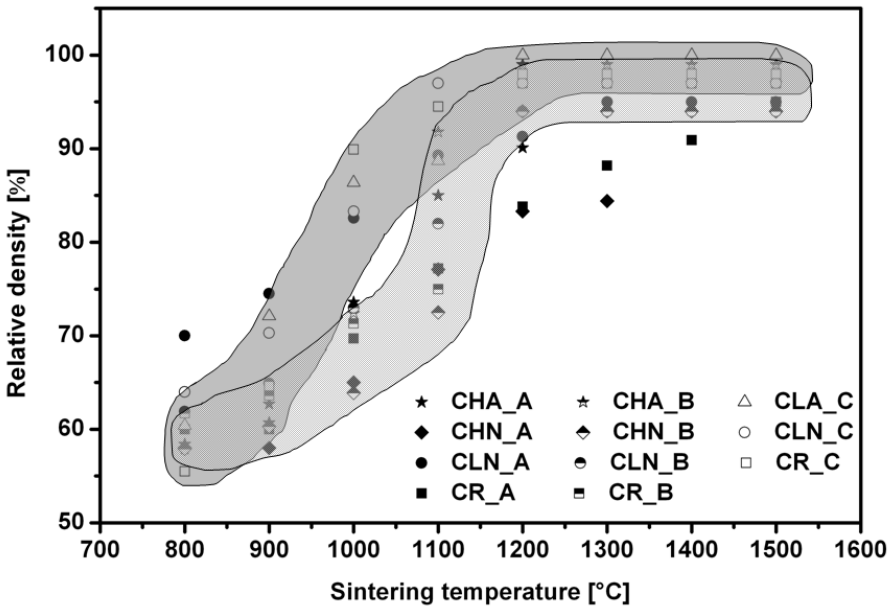

Figure 5. Sintering behavior of the different CR, CH and CL synthesis routes.

As shown in Figure 5, three different regimes could be observed. All pure CGO samples (_A type) were sintered at the highest temperatures and reached a relative density higher than 95% at temperature equal or higher than 1300°C.

The introduction with ball-milling of 0.5 at.% Fe reduced the sintering temperature to 1200°C for all samples but also modified the densification behavior as noted by Zhang et al. [15]. For example, the sintering temperature is lowered by 300°C for samples type CR_B compared to samples type CR_A.

Introducing 0.5 at.% Fe as iron nitrate during the CGO synthesis even reduced the sintering temperatures to lower temperature and accelerated the densification process. After sintering at 1000°C, the three _C type samples had a relative density higher than 80% and the CLN_C type samples had a relative density of 97% after sintering at 1100°C.

3.3. Microstructure.

As the sintering procedure of a pellet was stopped when the relative density was 95% or higher, all samples had a different sintering temperature. It can be expected that the lower the sintering temperature was, the smaller the grain size of CGO ceramics were. In other studies [11], it was observed that the introduction of transition metal oxide can reduce sintering temperature of CGO pellets, but also promotes grain growth of CGO ceramics.

The combination of those two effects can be seen in Figures 6a and 6b that are representative of the samples with particle size around 500nm. The undoped sample CHN_A was sintered at 1500°C and had average grain size 1400nm, whereas the doped sample CHN_B was sintered at 1200°C and had an average grain size smaller than 400nm. Sample type CR followed the same trend as sample type CHN but for sample type CHA the difference between sintering temperatures was probably too small so the effect of the introduction of iron oxide had increased the grain size.

For CLN type samples, the starting particle size was smaller. After sintering, undoped samples CLN_A showed an average grain size of 140nm, CLN_B type samples had an average grain size of 90nm and CLN_C type samples had an average grain size of 70nm (see Table 1 and Figures 6c, 6d and 6e).

With a sintering temperature of 1100°C, CLN_C type samples lead to the lowest sintering temperature and the smallest grain growth. For routes CLN and CR, adding the transition metal during the synthesis of CGO ceramics (routes _C) lead to smaller grain growth than adding the transition metal during the ball-milling step (route _B).

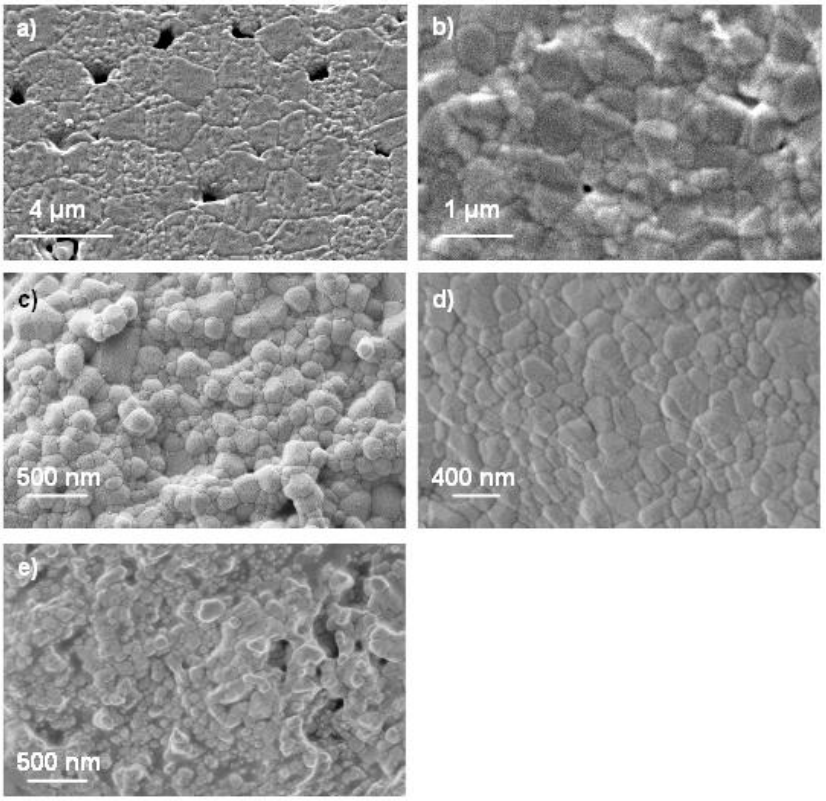

Figure 6. SEM micrographs of different samples after sintering procedure.

3.4. Conductivity measurements.

From the impedance characteristics of each sample, it was possible to extract the total conductivity and the contributions of the bulk or grain interior conductivity and of the grain boundary conductivity. Although 'grain boundary conductivity' is a misnomer, as it should pertain to the actual grain boundary dimensions, the term is used here to facilitate comparison between the samples. It also relates in this way to the overall conductivity. Figure 7 shows the Arrhenius plot of the total conductivity, of the grain boundary conductivity and of the bulk conductivity for a typical sample; here a CLN_B sample is depicted. Both grain boundary conductivity and bulk conductivity are following an Arrhenius behavior between 750°C and 300°C with activation energies of 0.98eV and 0.67eV respectively. It can be seen

that the total conductivity is following two trends between 300°C and 750°C. At high temperatures, the total conductivity is following the Arrhenius behavior of the grain interior (bulk), whereas at low temperatures the total conductivity is following the Arrhenius behavior of the grain boundary conductivity. Models for grain boundary and bulk conductivity are calculated values assuming a perfect Arrhenius behavior. The model for the total conductivity is obtained by adding the two models for grain boundary and bulk conductivity. One can see the clear match with the measurement data points over the whole temperature range.

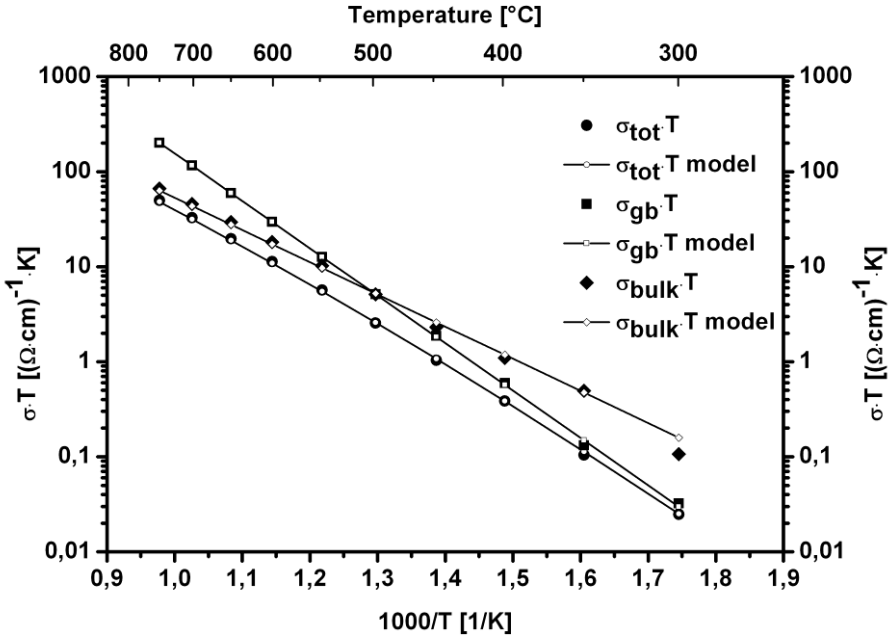

Figure 7. Arrhenius plot of the total conductivity, of the grain boundary conductivity and of the bulk conductivity for samples CLN_B samples in air. Empty signs are measurements, bold signs and lines are models.

The effect of the introduction of iron in the CGO electrolyte is shown in Figure 8 where the Arrhenius graphs of the different CR and CLN samples are depicted. A clear difference between samples CR and CLN is observed.

The total conductivity of the pure CR sample CR_A - 3.1×10^{-3} $S.cm^{-1}$ at 600°C - is much lower than the samples in which iron is introduced for CR_B and for CR_C. The total conductivity of CR_C samples - 1.7×10^{-2} $S.cm^{-1}$ at

600°C- is slightly higher than the one of sample CR_B – $1.2x10^{-2}$ $S.cm^{-1}$ at 600°C. On one hand, the bulk conductivity of the CR samples are equal ~ $6x10^{-4}$ $S.cm^{-1}$ at 350°C. On the other hand, the grain boundary conductivity of CR_B and CR_C is one order of magnitude higher than the grain boundary conductivity of CR_A – $2.1x10^{-5}$ $S.cm^{-1}$ at 350°C.

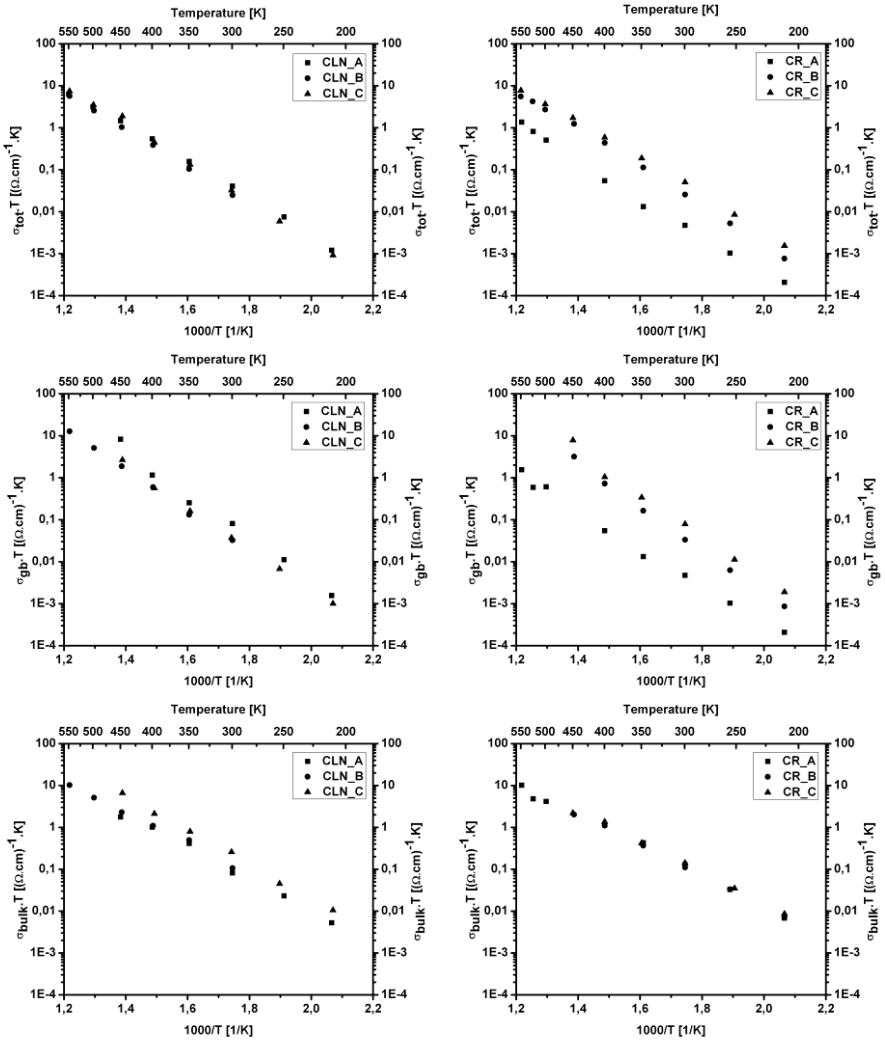

Figure 8. Arrhenius plot of the total conductivity (top), of the grain boundary conductivity (middle) and of the bulk conductivity (bottom) for samples CLN (left) and samples CR (right) in air.

As shown Figure 8, the introduction of iron is improving the grain boundary conduction but is not changing the bulk conductivity in the grains for CR samples. Moreover, the grain boundary conductivity of CR_C - $5.4x10^{-4}$ $S.cm^{-1}$ at 350°C - is twice the one of CR_B – $2.6x10^{-4}$ $S.cm^{-1}$ at 350°C whereas only the way to introduce iron is changed but not the composition. For CR_B and CR_C, activation energies for grain boundary, bulk and total conductivity are in good agreement with the values previously published [15]. However, the activation energy for the grain boundary of CR_A is much higher (1.23 eV) than for the other samples. Transmission Electronic Microscopy was used to characterize the difference between CR_B and CR_C samples, the results of this analysis is presented in the next section.

The electrical behavior for the series of CLN samples is different. The total conductivities for CLN_A and CLN_B are comparable at $1.3x10^{-2}$ $S.cm^{-1}$ at 600°C. CLN_C showed a somewhat higher total conductivity at 1.7 $x10^{-2}$ $S.cm^{-1}$ at 600°C. The highest grain boundary conductivity was measured for CLN_A samples – $4.0x10^{-4}$ $S.cm^{-1}$ at 350°C -, whereas CLN_B and CLN_C had the same grain boundary conductivity at ~$2.0x10^{-4}$ $S.cm^{-1}$ at 350°C. However, the bulk conductivity of CLN_C was higher by a factor 2 than the bulk conductivity of CLN_A and CLN_B samples. In this case, the introduction of iron is not decreasing the grain boundary conductivity but increasing the bulk conductivity.

3.5. TEM characterization.

CR_B and CR_C samples were prepared into a suitable TEM specimen by the method of dimple grinding/polishing and precision argon ion etching. Before analysis the finalized TEM specimen was given a plasma cleaning treatment for 4 minutes in a mild environment of Ar/H2. Energy Filtered TEM analysis (EF-TEM) was then carried out on several different areas each exhibiting clear grain boundary sections. In addition EF-TEM Spectrum Imaging (EF-TEM-SI) was performed to give more precise spectral information, giving clues about any artifacts encountered, and because the detection limit is better than EF-TEM using the 3-window method. Further proof was provided by Energy Dispersive X-ray analysis (EDX) in a Point-and-Shoot way i.e., by focusing the electron beam onto a small spot on and

around the grain boundary. Two parameters made this experiment rather difficult. First of all, although EDX is the most sensitive technique with detection limit of 0.1-1 at.%, a clear discrimination between Fe and the rest was very difficult due to severe overlap of Gd, Ce and Fe peaks. Secondly, the concentration of Fe (0.5 at.%) is just in the limit of the detection limit. EF-TEM micrographs and their associated iron mapping with EDX are shown in Figure 9 for CR_B and in Figure 10 for CR_C.

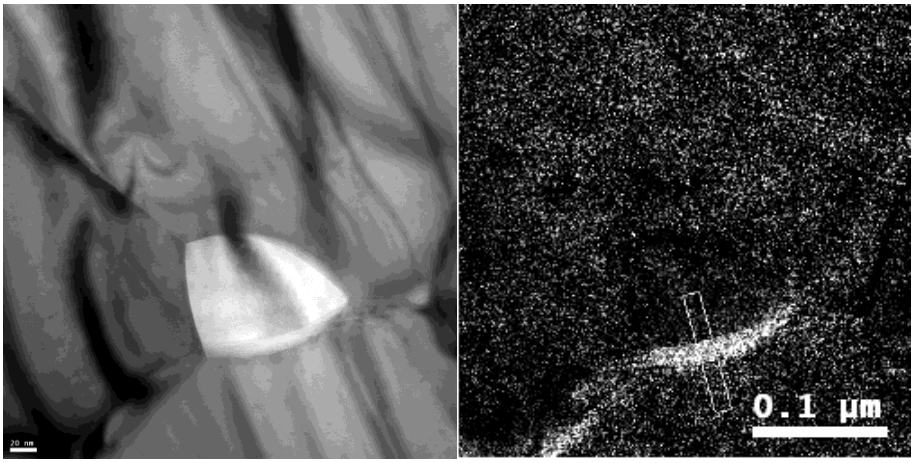

Figure 9. EFTEM of CR_B and iron mapping with EDX.

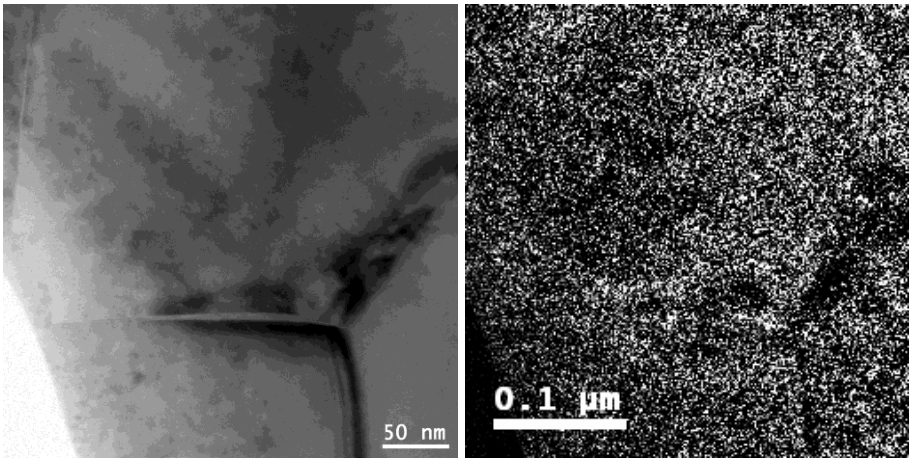

Figure 10. EF-TEM of CR_C and iron mapping with EDX.

For both samples, grain boundaries were well defined and very narrow. The best way to analyze the grain boundary was then to analyze areas were the grain boundary was just along the surface. In sample CR_B, it was possible to find trace of iron in the grain boundary as shown in figure 10a. However, the signal of iron was vanishing during the measurement. This effect could not be explained. In sample CR_C, it was not possible to spot any trace of iron in the grain boundary above the noise level as shown in figure 10b where a typical measurement is depicted. One possible explanation of the better grain boundary conductivity of CR_C compared to sample CR_B could thus be that the iron was better dispersed in the grain boundaries due to this novel method of dispersing iron in the CGO matrix.

4. Conclusions.

$Ce_{0.9}Gd_{0.1}O_{2-\delta}$ was synthesized via a complexation route using two different complexing agent, citric acid and ethylene glycol. A small amount of Fe loading (0.5 at.%) was used as a sintering aid to reduce sintering temperature and improve electrochemical behavior. The iron was introduced in two different ways, either via ball milling of iron oxide with CGO ceramics (route_B) or via addition of iron nitrate directly during the synthesis of CGO ceramics (route_C). This last route is a novel way of mixing the sintering agent with the CGO ceramics.

Introducing iron oxide by ball milling (route_B) reduced the sintering temperature of at least 100°C and up to 300°C when compared to pure samples. Introducing the iron during the synthesis of CGO even further decreased the sintering temperature. The densification up to 80% of relative density was obtained at lower temperature than with route_B. The samples loaded with iron were sintered at lower temperatures. With the introduction of iron, lower grain growth was observed with route_B and route_C than with route_A.

The electrical behavior was depending on the complexing agent used. When using ethylene glycol as complexing agent, the sample doped with route_C was having the best conductivity due to high bulk conductivity. When using citric acid, the grain boundary conductivity was improved by factor 10 with route_B and by factor 20 by route_C. This could be explained by a better

dispersion of iron in the grain boundary in samples from route_C than in samples from route_B.

References

[1] Steele B.C.H., Br Ceram. Proc. 56 (1996) 151.
[2] Blumenthal R.N., Brugner F.S., Garnier J.E., J. Electrochem. Soc. 120 (1973) 1230.
[3] Yahiro H., Eguchi K., Arai H., Solid State Ionics 21 (1986) 37.
[4] Faber J., Geoffroy C., Roux A., Sylvestre A., Abelard P., Appl. Phys., A Mater. Sci. Process. 49 (1989) 225.
[5] Balazs G.B., Glass R.S., Solid State Ionics 76 (1995) 155.
[6] Molin S., Gazda M., Jasinski P., J. Rare Earths 27 (2009) 655.
[7] Butler V., Catlow C.R.A., Fender B.E.F., Harding J.H., Solid State Ionics 8 (1983) 109.
[8] Kudo T., Obayashi H., J. Electrochem. Soc. 122 (1975) 142.
[9] H. Yahiro, K. Eguchi, H. Arai, J. Electrochem. Soc. 135 (1998) 2077.
[10] Kleinlogel C., Gaukler L.J., Advanced materials, 13 (2001) 1081.
[11] Zhang T.S., Ma J., Leng Y.J., Chan S.H., Hing P., Kilner J.A., Solid State Ionics 168 (2004) 187.
[12] Zhang T.S., Ma J., Leng Y.J., He Z.M., J. Crystal Growth, 274 (2005) 603.
[13] Kleinlogel C., Gauckler L.J., Solid State Ionics, 135 (2000) 567.
[14] Fagg D.P., Kharton V.V., Frade J.R., Journal of Electroceramics, 9 (2002) 199.
[15] Zhang T.S., Ma J., Luo L.H., Chan S.H., Journal of Alloys and Compounds, 422 (2006) 46.
[16] Mendelson M.I., J. Am. Ceram. Soc., 8 (1969) 443.

Chapter 3.

The impedance of thin dense oxide cathodes

Abstract.
The impedance is derived for a dense layer electrode of a mixed conducting oxide, assuming that the electronic resistance may be ignored. The influence of layer thickness, oxygen diffusion and surface exchange rate on the 'General Finite Length Diffusion' expression is evaluated. The thickness dependence is tested for a series of thin, dense layer electrodes of $La_{0.6}Sr_{0.4}Co_{0.2}Fe_{0.8}O_{3-\delta}$ (LSCF) deposited on a $Ce_{0.9}Gd_{0.1}O_{1.95}$ electrolyte by pulsed laser deposition (PLD). A minimum thickness is required to avoid the influence of contact points of the contacting Pt-gauze and sheet resistance, which is about 1 µm for the studied LSCF electrodes. LEISS surface analysis indicates that PLD deposition process easily leads to a significant Cr contamination of the LSCF surface. Electrochemical impedance spectroscopy analysis indicates that the influence on the exchange rate of this Cr-contamination is still negligible.

1. Introduction.

Mixed conducting oxides (MIEC's) are finding important application in solid oxide fuel cells (SOFC), both as cathode and anode, and in semi-permeable membranes for (partial) oxidation reactions. A very important aspect of these applications is the transfer and reduction of ambient oxygen at the gas/solid interface, or visa versa. The overall transfer reaction can be presented as:

$$O_{2,g} + 4e^{-} + 2V_O^{\circ\circ} \Leftrightarrow 2O_O^x \quad (1)$$

But in reality it will involve a series of steps, e.g. adsorption, dissociation, charge transfer and possibly surface diffusion. So far the exact reaction mechanism is still poorly understood. Another significant problem is the exact nature of the surface and the possibility of poisoning by foreign atoms. This is especially of significance for SOFC cathodes where chromium poisoning, which originates from the steel interconnect plates, has been recognized as a serious problem.

Using oxygen isotope ($^{18}O_2$) exchange the overall exchange rate can be determined. SIMS depth profiling can yield both the tracer diffusion coefficient and the exchange rate [1]. Gas phase analysis in a closed system [2] or in a newly developed pulse technique [3], can yield reaction rates for a two step mechanism, but requires the use of powders. Conductivity relaxation measurements [4,5] can also provide the exchange rate and chemical diffusion coefficient, but sample dimensions must be carefully chosen [6]. A third option is the study of a thin layer of the MIEC, deposited on an appropriate electrolyte in a three electrode configuration with electrochemical impedance spectroscopy (EIS) [7]. The advantage of such a system is that the study of the influence of surface poisoning can be carried out quite easily. A proper derivation of the impedance of such an electrode arrangement is not readily available in literature. One of the disadvantages of EIS measurements can be that current collectors must be used. A Pt mesh is most commonly used as current collector. However, Pt is known to be active for oxygen dissociation and hence may influence the oxygen surface exchange rate. As gold is virtually inert for oxygen dissociation it is a good alternative as current collector in these experiments. In this contribution a simple model is derived for the impedance of a thin layer and is applied to a dense $La_{0.6}Sr_{0.4}Co_{0.2}Fe_{0.8}O_{3-\delta}$ (LSCF) electrode layer,

deposited with pulsed laser deposition (PLD) on a Gd-doped ceria electrolyte. The influence of the layer thickness on the electrode property is studied and some preliminary results on chromium addition are presented. Finally the influence of the catalytic activity of the current collector is presented.

2. Theory : Generic Finite Length Diffusion (GFLD) equation.

Figure 1 presents schematically the electrochemical process in a thin dense oxide layer (MIEC) which is on one side connected to an oxygen conducting electrolyte (x = 0) and on the other side to the ambient (with fixed pO_2 at x = l). The following assumptions are made:

- The electronic conductivity is large enough to be ignored in the derivation.
- The electrode voltage, with respect to a reference electrode at the same ambient pO_2 is controlled by the oxygen activity in the MIEC at the x = 0 interface.
- The oxygen exchange rate can be represented with a single reaction rate, k (dimension: $cm \cdot s^{-1}$).
- Charge transfer and double layer charging processes at the electrolyte/MIEC interface are not included.

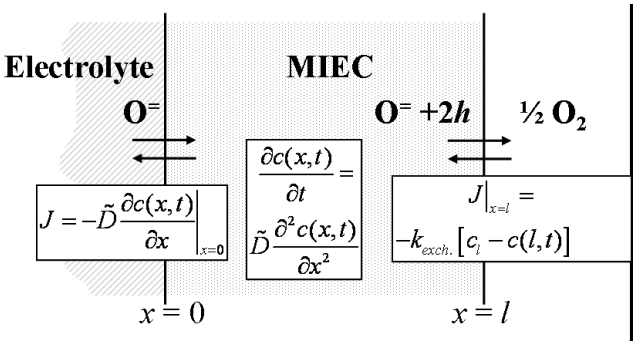

Figure 1. Reaction schematic for the oxygen transfer through a MIEC layer.

The Fickian diffusion equations are:

$$J = -\tilde{D}\frac{\partial c(x,t)}{\partial x}\bigg|_{x=0} \quad \text{and} \quad \frac{\partial c(x,t)}{\partial t} = \tilde{D}\frac{\partial^2 c(x,t)}{\partial x^2} \qquad (2)$$

The right-hand boundary condition at x = l is given by:

$$J\big|_{x=l} = -\tilde{D}\frac{\partial c(x,t)}{\partial x}\bigg|_{x=l} = -k_{exch.}\left[c_l - c(l,t)\right] \tag{3}$$

where c_l is the (apparent) equilibrium concentration in the ambient. With electrochemical impedance spectroscopy only a small perturbation is applied, hence it is useful to define the concentration variation, $\Delta c(x,t)$:

$$\Delta c(x,t) = c(x,t) - c_O^{\circ} \tag{4}$$

Here c_O° is the equilibrium oxygen concentration, hence c_l = c_O°. After transformation of the diffusion equations to the Laplace space, a general solution for eq. (2) can be given:

$$C(x,p) = A\cosh x\sqrt{p/\tilde{D}} + B\sinh x\sqrt{p/\tilde{D}} \tag{5}$$

with p the Laplace variable. Inserting (5) in the boundary condition equation (3) yields a relation between the coefficients A and B:

$$B = -A\frac{\sqrt{p\tilde{D}} + k_{exch.}\coth l\sqrt{p/\tilde{D}}}{\sqrt{p\tilde{D}}\cdot\coth l\sqrt{p/\tilde{D}} + k_{exch.}} \tag{6}$$

The current at x = 0 is, after Laplace transformation of eq. (2), defined by:

$$I(p) = n\cdot F\cdot S\cdot J(p) = -n\cdot F\cdot S\cdot B\sqrt{p\tilde{D}} \tag{7}$$

where n is the charge of the diffusing ion (n=2 for oxygen), F is the Faraday constant and S is the surface area. The electrode voltage is directly related to the oxygen activity, $a_O(x,p)$, which is the sum of the equilibrium value and the electrochemical perturbation, $a_O(x,p) = a_O^{\circ} + a(x,p)$. This is expressed in Laplace space with:

$$V(p) = \frac{RT}{nF}\ln\left(\frac{a_O^{\circ} + a(x,p)}{a_O^{\circ}}\right)_{x=0} \approx \frac{RT}{nFa_O^{\circ}}a(x,p)_{x=0} \tag{8}$$

assuming that the perturbation is much smaller than the equilibrium activity. The relation between concentration and activity is given by the thermodynamic enhancement factor, W :

$$W = \frac{\partial \ln c}{\partial \ln a} = \frac{c}{a} \cdot \frac{\partial a}{\partial c} \tag{9}$$

This factor can be obtained from TGA or coulometric titration experiments. Now eq. (8) can be expressed in $C(x, p)$ by combining eqs (8) and (9):

$$V(p) = \frac{RT}{nFc_i^\circ}\left[\frac{\partial \ln a_O^\circ}{\partial \ln c_O^\circ}\right] C(x, p)_{x=0} = \frac{RT}{nFc_O^\circ}\left[\frac{\partial \ln a_O^\circ}{\partial \ln c_O^\circ}\right] A \tag{10}$$

Dividing the voltage by the current yields the impedance in Laplace space. Assuming steady state conditions, $j\omega$ can be substituted for the Laplace variable p , resulting in the final impedance equation for the 'GFLD':

$$Z(\omega) = \frac{Z_0}{\sqrt{j\omega \tilde{D}}} \frac{\sqrt{j\omega \tilde{D}} \coth l\sqrt{j\omega / \tilde{D}} + k_{exch.}}{k_{exch.} \coth l\sqrt{j\omega / \tilde{D}} + \sqrt{j\omega \tilde{D}}} \tag{11}$$

with:

$$Z_0 = \frac{RT}{n^2 F^2 c_O^\circ}\left[\frac{\partial \ln a_O^\circ}{\partial \ln c_O^\circ}\right] = \frac{RT}{8F^2 S \cdot c_O^\circ}\left[\frac{\partial \ln P_{O_2}}{\partial \ln c_O^\circ}\right] \tag{12}$$

The high frequency limit yields the well-known Warburg or semi-infinite diffusion relation. It is easy to see that for very fast surface exchange ($k \to \infty$) equation (11) simplifies to the finite length Warburg (FLW, [8,9]), while for blocking conditions ($k = 0$) the finite space Warburg (FSW, [8,9]) evolves.

The low frequency semicircle can be parameterized (for $\omega < 0.01 \cdot \frac{\tilde{D}}{2l^2}$) through:

$$Z(\omega) = Z_0 \frac{\frac{\tilde{D}}{l} + k}{\frac{\tilde{D}}{l}k + j\tilde{D}\omega} = Z_0 \frac{\left[\frac{1}{k} + \frac{l}{\tilde{D}}\right]\left[1 - j\omega\frac{l}{k}\right]}{1 + \omega^2 \frac{l^2}{k^2}} \quad (13)$$

which is the model of a capacitance parallel to a resistance:

$$R_{dc} = Z_0\left[\frac{1}{k} + \frac{l}{\tilde{D}}\right] \text{ and } C_{chem} = \frac{1}{Z_0\left[\frac{1}{l} + \frac{k}{\tilde{D}}\right]} \quad (14)$$

In case $k << \tilde{D}$, i.e. surface exchange limitation, then C_{chem} will be directly proportional to the thickness of the electrode layer l. The time constant, $\tau = R_{dc} \cdot C_{chem} = \frac{l}{k}$, is independent of the diffusion coefficient. $\tilde{D}$ can be obtained from the slope of R_{dc} vs. l.

3. Experimental procedure.

Dense LSCF cathodes with different thicknesses l were deposited by Pulsed Laser Deposition (PLD) on 2.5 mm thick $Ce_{0.9}Gd_{0.1}O_{1.95}$ pellets in a three electrode arrangement, see Figure 2. The pulsed laser deposition was performed with a KrF excimer laser, using a fluency of 2.6 J/cm^2 and a frequency of 20 Hz. The LSCF target was an isostatically pressed LSCF pellet on a rotating holder. The laser ablation occurred in a vacuum chamber in 0.02 mbar oxygen ambient. The CGO substrates were heated to 750°C during deposition.

The reference electrode was provided by a Pt wire bonded with a little Pt-ink into a grove at half height at the cylindrical side of the CGO pellet. For the counter electrode a similar PLD layer with different thickness was applied. The use of a porous Pt-counter electrode is not advisable as the electrode properties are inferior to the LSCF electrodes (see e.g. [10]). Two types of

current collectors were used, either platinum grid or gold grid with 85.5 mesh. Each sample was measurement with a new grid.

The electrode impedance was measured with a Solartron 1250 FRA combined with a 1287 electrochemical interface over a frequency range of 65535 Hz to 10 mHz. The data is validated with a Kramers-Kronig test [11] and analysed with the CNLS-program 'Equivalent Circuit' [12]. Thickness dependent measurements were carried out 750°C in air. Earlier obtained results for a 15 µm thick PLD layer of LSCF [15] are also included in the discussion.

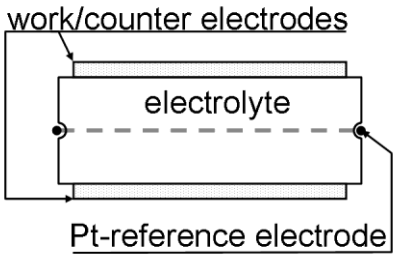

Figure 2. Schematic arrangement of the three electrode cell with two PLD layers.

4. Results and discussion.

4.1. Effect of the electrode layer thickness.

Figure 3 shows a close up of the PLD electrode and a SEM micrograph of the surface area. The typical impedance of a 1 µm thick electrode is presented in Figure 4. The high frequency Warburg behavior cannot be observed. The analysis results for R_{dc} and C_{chem} are presented in Figure 5.

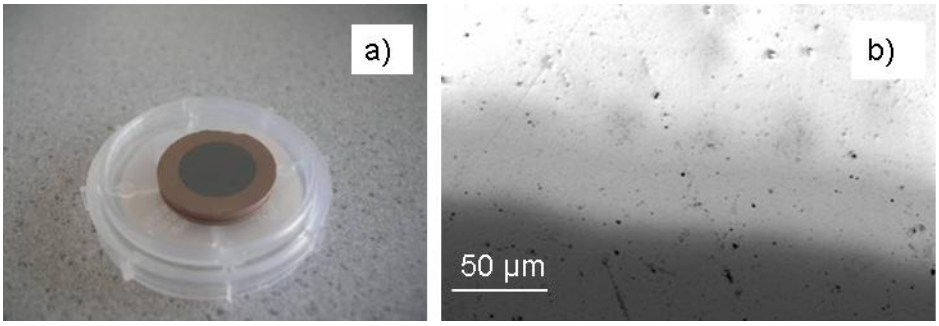

Figure 3. a) Photograph of a PLD LSCF layer on a CGO electrolyte. b) SEM image of the LSCF surface.

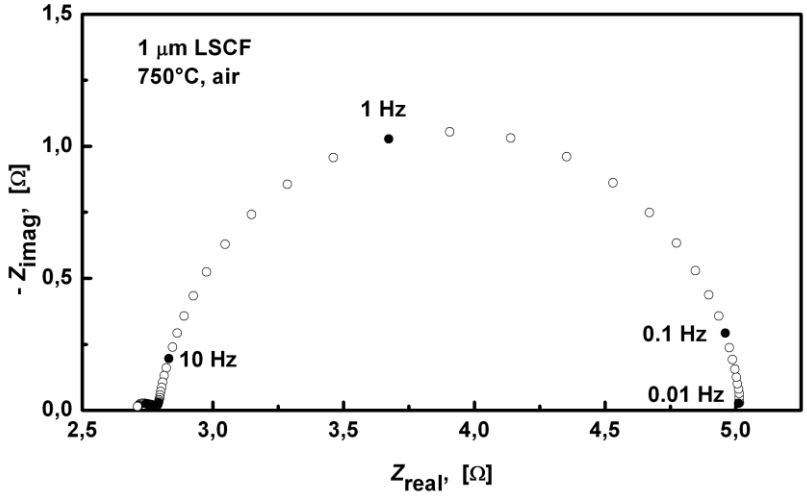

Figure 4. Typical impedance diagram for a 1µm thick PLD LSCF layer at 750°C in air.

For electrode thicknesses below 1 µm, the chemical capacitance shows a clear linear thickness dependence, which is consistent with surface exchange limitation, i.e. $k << \tilde{D}$, see eq. (14). However, for electrode thicknesses above 1 µm, $\frac{1}{l} << \frac{k}{\tilde{D}}$ and the chemical capacitance tends to a

constant value $C_{chem} = \frac{\tilde{D}}{Z_0 k}$. This value is actually a pseudo chemical capacitance as there is a clear competition between k and $\tilde{D}$.

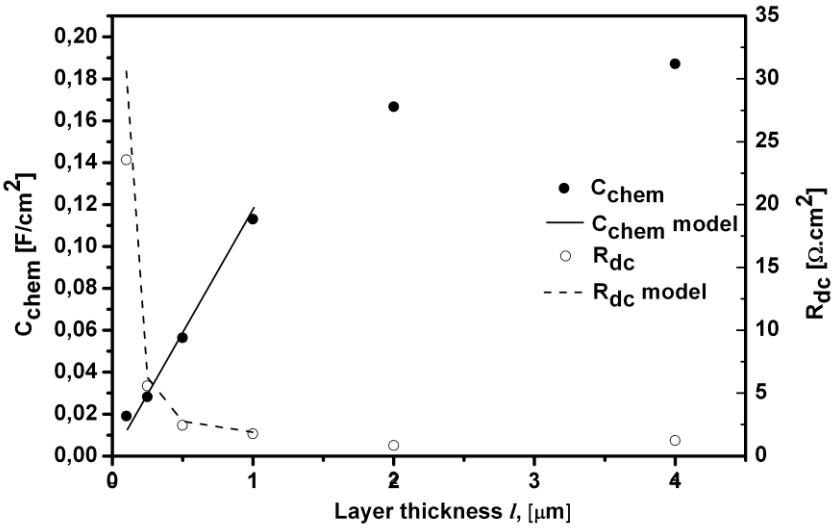

Figure 5. Thickness dependence of R_{dc} and C_{chem} at 750°C in air. Model values are calculated according to eq.(14) and eq.(15).

The electrode resistance R_{dc}, however, seems to be inversely proportional to the electrode thickness, which is neither consistent with diffusion limitation nor with surface exchange limitation. The observed dependence can be modeled (see Figure 5) with:

$$R_{dc} = R_{exch} + R_{elect} \cdot l^{-2} \tag{15}$$

with: R_{exch} = 2.0 Ω (1.6 Ω·cm^2) and R_{elect} = 2.9·10^5 Ω·nm^{-2}. This effect is caused by the distance between contact points of the Pt-mesh with respect to the layer thickness. Because of the sheet resistance a significant polarization drop evolves along the surface from each contact point, causing

a concentration/activity gradient. Hence the 'apparent effective' surface area for the exchange decreases with diminishing layer thickness. For the 100 nm layer the electrode impedance shows clearly a more diffusive behavior (depressed semicircle, close to 45°) which is consistent with this proposed model. This effect should be further analyzed using a Finite Element Modeling approach. From these results it is at least evident that the surface exchange reaction is rate determining for the dense electrodes.

4.2. Effect of current collector.

The current collector has a strong effect on the measurements performed on the thin dense electrodes. Figure 6 shows the temperature dependence of R_{dc} for the LSCF thin electrodes with thicknesses 2 µm and 4 µm with either platinum grid or gold grid as current collector. With a Au-grid the activation energy obtained for R_{dc} is 191 kJ·mol-1. This value corresponds well to published data on the surface exchange rate for LSCF as obtained from conductivity relaxation measurements [13,14]. It is also identical to the value obtained by Giesbers [15] on a 15 µm thick PLD sample (190 kJ·mol-1), although here a Pt mesh was used as current collector. The Pt mesh was, however, not 'pristine' as it had been used many times with LSCF samples and most likely had a significantly contaminated surface. Measurements with fresh, clean Pt grids on the 2 and 4 µm thick samples showed a much lower activation energy of 126 kJ·mol-1, clearly indicating the catalytic enhancement by the Pt grid.

Moreover, the R_{dc} values measured with Pt grid are much lower than those measured with the Au grid. This effect can be explained by an enhanced dissociation rate of oxygen due to the presence of the Pt-catalyst (clean Pt-grid). The observed k-value with Pt present is much less related to the surface exchange rate of LSCF.

According to eq.(14), R_{dc} contains both k and $\tilde{D}$, hence it does not provide a direct value for the surface exchange rate. However, the time constant of the low frequency semicircle ($\omega < 0.01 \cdot \tilde{D} / 2l^2$) is, according to the

developed model, inversely proportional to k: $\tau = R_{dc} \cdot C_{chem} = l / k$. Using this equation somewhat lower values for the activation energy of k are obtained for both the Pt-grid and the Au-grid results, see Figure 7.

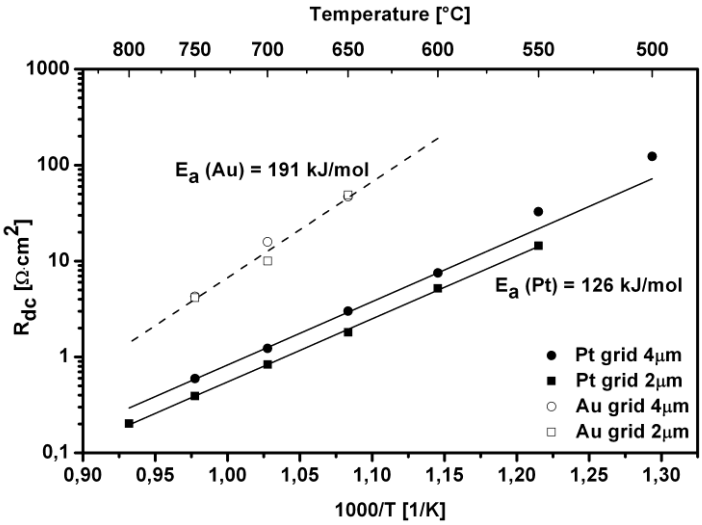

Figure 6. Arrhenius graph of the electrode resistances for different current collectors.

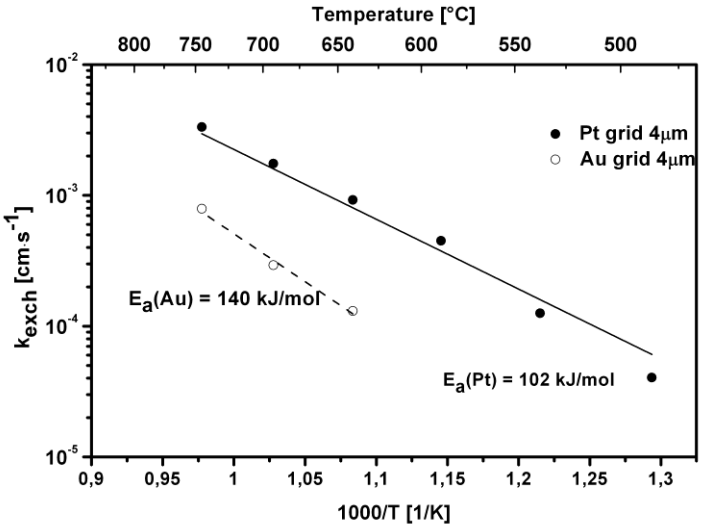

Figure 7. Arrhenius graph of the surface exchange coefficent for different current collectors.

4.3. Effect of Cr poisoning.

A preliminary poisoning study was carried out by adding a small amount of chromium by PLD to a fresh LSCF surface. The surface analysis was performed with Low Energy Ion Scattering Spectroscopy (LEISS) at Calipso b.v., Eindhoven (now in Münster). This sample showed a large Sr peak and a small Cr peak. A 'pristine' sample, used as reference, showed a more significant Cr peak, while the Sr peak virtually had disappeared, see Figure 8. This PLD LSCF layer had been the first layer deposited on the CGO electrolyte and, subsequently, had been in contact with the stainless steel heating plate on which the sample was mounted during PLD deposition. This clearly indicates that chromium is easily transferred by contact. Two of the four layers had thus already a Cr surface contamination. The trend in the thickness dependence of R_{dc} does not indicate a serious influence of this Cr-poisoning, possibly indicating that more than a surface layer is needed for an appreciable effect.

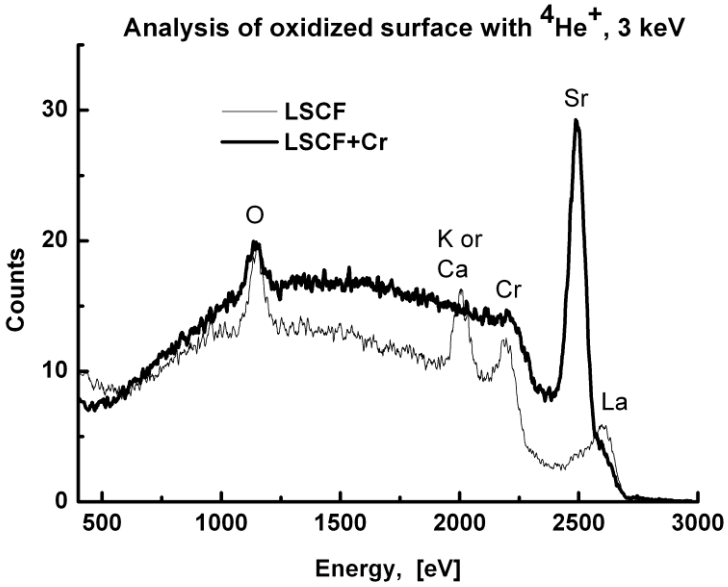

Figure 8. LEIS spectrum of intentionally 'Cr-poisoned' LSCF surface (gray line) and pristine surface, but inadvertently poisoned by stainless steel heater plate (black line).

5. Conclusions.

The surface exchange rate of mixed conducting oxides can be studied easily on well-defined thin and dense layers deposited with pulsed laser deposition. Same type working and counter electrodes are strongly advised for a standard 3-electrode set-up. The polarization resistance of the counter electrode may not be significantly larger than the working electrode.
An important criterion for the minimal required thickness is the relation between the density of contact points (gauze mesh), the layer thickness, the electronic conductivity and the exchange rate. For the studied LSCF compound a minimum thickness of 1 µm is required with the use of a standard Pt-gauze. The effect of the current collector plays an important role and can affect the measurements. As fresh grid have an activity for oxygen dissociation, it is advisable to use gold grid as current collector. A theory was developed to access diffusion coefficient and surface exchange coefficient from the EIS measurements. This theory was developed for materials in which electronic resistivity is negligible. It can thus not be used for all materials and all thicknesses of electrodes.
Great care must be taken during the PLD-procedure to avoid inadvertent contamination from the sample support/heater system. In direct contact chromium is already transferred from stainless steel to the backside of the cell.

References.

[1] Chater R.J., Carter S., Kilner J.A., Steele B.C.H., Solid State Ion. 53-56 (1992) 859.

[2] Boukamp B.A., Vinke I.C., de Vries K.J., Burggraaf A.J., in 'Fast Ion Transport in Solids', eds Scrosati B., Magistris A., Mari C.M. and Mariotto G., NATO ASI Series, Series E: Appl. Sci. Vol. 250 (Kluwer Academic, Dordrecht, 1993) p. 167.

[3] Bouwmeester H.J.M., Song C., Zhu J., Yi J., van Sint Annaland M., Boukamp B.A., Chem. Phys. Phys. Chem., DOI: 10.1039/B912712G.

[4] Yasuda I., Ishinuma M., in: Ramanarayanan T.A., Worrell W.L., Tuller H.L. (eds) Proceedings of the 2nd Int. Symp. on ionic and mixed

conducting ceramics (Electrochem. Soc. proceedings series PV 1994-12) pp 209.

[5] ten Elshof J.E., Lankhorst M.H.R., Bouwmeester H.J.M., Solid State Ion. 99 (1997) 15.

[6] Boukamp B.A., den Otter M.W., Bouwmeester H.J.M., J. Solid State Electrochem, 8 (2004) 592-598.

[7] Kim G.T., Wang S., Jacobson A.J., Yuan Z., C. Chen, J. Mater. Chem. 17 (2007) 1316.

[8] Levi M.D., Lu Z., Aurbach D., Solid State Ion. 143 (2001) 309-318.

[9] Mohamedi M., Takahashi D., Uchiyama T., Itoh T., Nishizawa M., Uchida I., J. Power Sources 93 (2001) 93-103.

[10] Boukamp B.A., Solid State Ion. 143 (2001) 47.

[11] Boukamp B.A., J. Electrochem. Soc., Vol. 142 [6] (1995) 1885-1894.

[12] Boukamp B.A., Solid State Ion. 20 (1986) 31-44.

[13] Bouwmeester H.J.M., den Otter M.W., Boukamp B.A., J. Solid State Electrochem, 8 (2004) 599-605.

[14] Bucher E., Sitte W., Solid State Ion. (2010), doi:10.1016/j.ssi.2010.01.006.

[15] Giesbers A., Master thesis, Development of cathodes for low temperature SOFC, University of Twente, 2004.

Chapter 4.

The effect of microstructure on the performance of LSCF cathodes.

Abstract.

Symmetrical two-electrode cells with different porous microstructures of LSCF cathodes were studied with Electrochemical Impedance Spectroscopy. Different microstructures were obtained by varying the sintering temperature after screen-printing. The microstructure of the LSCF cathode has a strong influence on the cell's performance. Cells sintered at 1200°C showed the lowest apparent electrolyte resistance and the lowest Area Specific Resistance for the cathode, with values as low as 0.70 $\Omega \cdot cm^2$ at 550 °C. Both temperature and oxygen partial pressure dependences showed that the surface oxygen exchange reaction is the rate limiting step. The impedance characteristics of the cells sintered at 1200 °C was analyzed with a CNLS procedure, using different equivalent circuits from literature. Analysis shows that the inclusion of a Gerischer impedance in the equivalent circuit for modeling the LSCF electrodes not only presents a physically realistic understanding of the electrode processes, but also results in lower error estimates for the circuit parameters.

1. Introduction.

In the research for materials that can be used as cathodes in Solid Oxide Fuel Cells, strontium substituted lanthanum cobaltite are interesting perovskites to study because of their relevancy as potential electrocatalysts for oxygen reduction. When used in porous oxygen electrodes, very low polarization resistances were measured for different materials within the family: $(La_{1-x}Sr_x)CoO_{3-\delta}$, $(La_{1-x}Sr_x)(Co_{1-y}Fe_y)O_{3-\delta}$, $(La_{1-x}Sr_x)(Co_{1-y}Ni_y)O_{3-\delta}$, etc. Electrochemical Impedance Spectroscopy (EIS) is often used to understand the physical transport and transfer processes within these Mixed Ionic Electronic Conductor (MIEC) electrodes. Equivalent circuits are used to perform the analysis of the impedance spectra of those electrodes. However, the relationship between the physical processes and the different elements of the equivalent circuit is very often subject to debate. Cathodes of the same material with apparently similar types of microstructures have been modelled with quite different equivalent circuits (EC's).

The equivalent circuit ECa presented in Figure 1 is most commonly used to model the impedance characteristics of MIEC porous electrodes [1-4]. Kournoutis et al. [1] characterized $La_{0.8}Sr_{0.2}Co_{0.2}Fe_{0.8}O_{3-\delta}$ electrodes with thickness of 90μm with impedance spectroscopy as function of temperature and oxygen partial pressure. The impedance characteristics were determined by up to three different processes corresponding to overlapping depressed arcs (semicircles) in the Nyquist plots. The system was modelled using a simple equivalent circuit consisting of an ohmic resistance in series with three (R_iQ_i) sub-circuits. The authors underline that there is no exact physical reasoning behind this equivalent circuit, its choice was dictated by the general features of the Nyquist plots, taking into account its flexibility to describe the distributed response of real world electrochemical systems [5]. However, they attributed a process to each feature. The high frequency arc was identified as ionic diffusion in the electrode bulk and possibly a noncharge transfer surface exchange at the electrode / gas interface. The R_{hf} had a weak dependence on oxygen partial pressure, the activation energy value ~1.57eV was close to the one reported for oxygen self diffusion in $La_{0.6}Sr_{0.4}Co_{0.2}Fe_{0.8}O_{3-\delta}$, ~1.9eV [6, 7], the calculated pseudocapacitance C_{hf} was in the order of 5×10^{-4} $F \cdot cm^{-2}$, close to the low limit of the pseudocapacitance values (10^{-3} $F \cdot cm^{-2}$) estimated by Adler et al.[8]. The

authors note that there is no contradiction with the model developed by Adler et al. [8-10] that predicts a Gerischer impedance in the case that the rate controlling steps of the oxygen reduction reaction are chemical surface exchange and solid state oxygen diffusion. Indeed, a Gerischer element can be approximated over a finite range of frequencies by a series combination of two (R_iQ_i) sub-circuits with corresponding exponents n_i for the constant phase elements close to 0.5 and 1.

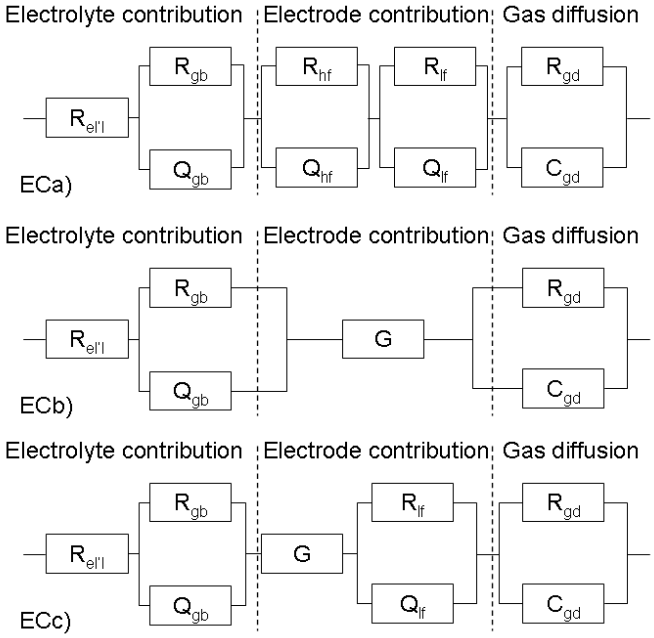

Figure 1. Different equivalent circuits used to analyze the impedance spectra. ECa and ECb are obtained from litterature, ECc evolved from this study.

The intermediate frequency arc was related to interfacial charge transfer involving atomic oxygen as R_{if} had an oxygen partial pressure dependence close to 0.25 [11-14]. The calculated pseudocapacitance C_{if} ranged from ~10^{-3} F·cm^2 under pure oxygen to 0.15 F·cm^2 at pO_2 = 0.7 kPa.

The low frequency arc was associated with gas diffusion limitation were R_{lf} showed an oxygen partial pressure dependence between 1.14 and 1.35. This low frequency arc is only observable at high temperatures, the apparent

activation energy is low: ~0.35eV, showing a nearly non activated step. The calculated pseudocapacitance values C_{lf} ranged between 0.4 and 8 $F \cdot cm^{-2}$.

As underlined by Kournoutis et al., Adler et al. [8-10] predict a Gerischer impedance for the same type of electrodes in case rate limiting steps of the oxygen reduction reaction are chemical surface exchange and solid state oxygen diffusion. Even when surface diffusion is considered in the electrode [10], a Gerischer like impedance is predicted and measured. According to Boukamp et al. [15], Gerischer impedances are observed when a chemical process and an electrochemical process are co-limiting. For example, the competition between surface diffusion and bulk diffusion, related to each other via the oxygen surface exchange process lead to a Gerischer impedance. Also slow adsorption coupled with surface diffusion can lead to a Gerischer impedance [16]. Sluyters-Rehbach and Sluyters [17-18] first presented the general impedance expression for CE-type reaction (chemical reaction followed by electrochemical reaction) and for CEC-type reaction (chemical – electrochemical – chemical reactions). For special conditions the quite complex impedance expression can be reduced to [19]:

$$Z_G(\omega) = \frac{Z_0}{\sqrt{K_a + j\omega}} = \frac{1}{Y_0\sqrt{K_a + j\omega}} \quad (1)$$

where K_a represents the effective transfer rate of the chemical reaction. The Gerischer impedance has been used to analyze the response of various types of electrode [19]. For the cathode of the SOFC, Adler et al. [8-10] arrived on basis of a formal modelling of the reaction steps at a ‘chemical impedance which is equivalent with a Gerischer impedance. Their model is presented by the equivalent circuit ECb, see Figure 1.

In this work, the effect of the LSCF cathode microstructure on the performance is studied. The impedance characteristics of the cathodes are analyzed by mean of Complex Non Linear Least Squares analysis with different equivalent circuits. The pertinence of those different analyses is discussed.

2. Experimental.

Symmetrical two-electrode cells were prepared by tape-casting and screen printing processes. Tape-casted yttria-partially stabilized zirconia (3YSZ, Tosoh) was used as electrolyte. Yttria-doped ceria (YDC, Praxair) was applied as interlayer by screen printing on both sides of the tape-casted 3YSZ electrolyte, followed by sintering at 1400 °C Two identical porous electrodes of $La_{0.6}Sr_{0.4}Co_{0.2}Fe_{0.8}O_{3-\delta}$ (LSCF, Praxair) were then screen printed on both sides of the electrolyte. Samples were sintered at different temperatures: 1100 °C, 1200 °C and 1300 °C.

The measurement of the electrochemical properties of the different cells were performed at open-circuit voltage in synthetic air as a function of temperature between 800 °C and 500 °C at 25 °C intervals, and as a function of oxygen partial pressure at 600 °C. The impedance characteristics were measured with a Solartron 1250 FRA combined with a 1287 electrochemical interface over a frequency range of 65,535 Hz to 10 mHz in a pseudo 4-electrode set up (separate current and voltage probe leads). The impedance data were validated with a Kramers–Kronig transform program [20] and analyzed with the software package 'Equivalent Circuit' [21,22].

3. Results and discussion.

3.1. Microstructure.

The cathode microstructure is highly depending on the sintering temperature, as shown by the SEM micrographs (see Figure 2). Due to densification during sintering, the cathodes sintered at 1100 °C, 1200 °C and 1300 °C have different thicknesses: 50 µm, 49 µm and 31µm, respectively. The grain growth is depending on the sintering temperature. The average grain size is 0.5 µm, 1 µm and 5 µm for sintering temperatures 1100 °C, 1200 °C and 1300 °C, respectively.

The samples sintered at 1300 °C present a strong grain growth that closes most of the pores of the cathode. These closed pores are not reachable for the gas phase. One can expect that an important part of the cathode is

electrochemically inactive and thus an important polarization resistance can be expected.

The samples sintered at 1100 °C present a fine microstructure with the smallest average grain size but a slight delamination can be observed at the interface between the electrolyte and the cathode. This delamination can be due to thermal treatment during testing the electrode but it can also occur during the fracture of the symmetrical cell for SEM analysis.

The samples sintered at 1200 °C present a fine microstructure, good connectivity between the grains. The adhesion of the cathodes to the electrolyte surface is very good.

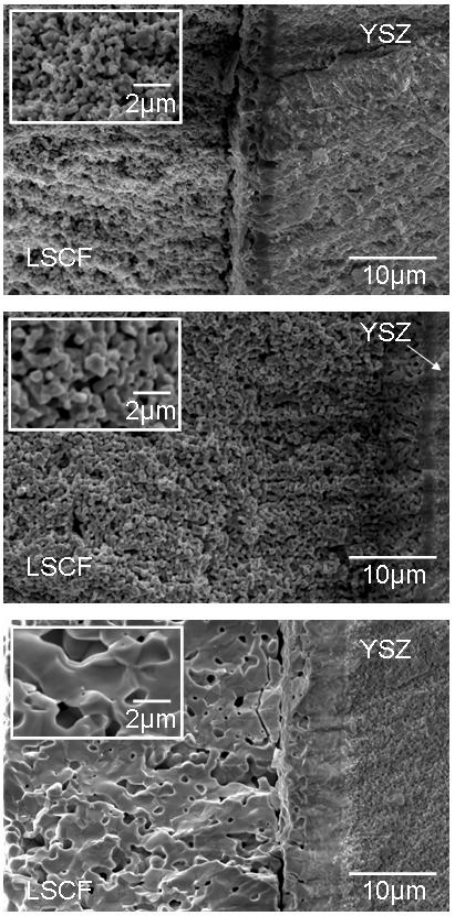

Figure 2. SEM micrographs of the fractured symmetrical cells sintered at different temperatures: (top) 1100°C, (middle) 1200°C and (bottom) 1300°C.

3.2. Effect of sintering temperature on the cathode's performance.

The impedance characteristics of the LSCF cathodes sintered at 1100 °C, 1200°C and 1300 °C in synthetic air at 550 °C are shown in Figure 3. As expected, the polarization resistance of the samples sintered at 1300 °C is much higher - 30 $\Omega \cdot cm^2$ at 550 °C – than those of the samples sintered at 1100 °C and 1200 °C. Major part of the cathode is not active because the gas phase cannot access it. Only the upper part of the cathode is active in the oxygen reduction reaction. Once oxygen gas is reduced, the diffusion path towards the electrolyte is long, resulting in a complex impedance characteristic. Because of this poor performance, the samples sintered at 1300 °C will not be further considered.

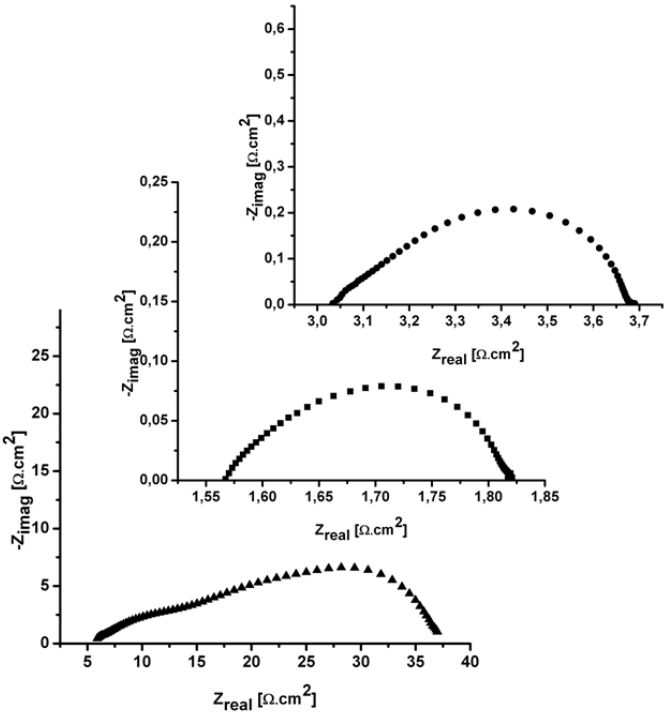

Figure 3. Impedance characteristics of porous LSCF cathode in air at 550°C sintered at (▲)1300°C, (■) 1200°C and (●)1100°C.

The samples sintered at 1100 and 1200 °C have a similar behaviour but the Area Specific Resistance (ASR) of the LSCF cathode sintered at 1200 °C –

0.70 Ω·cm^2 at 550 °C – is three times smaller than the ASR of the cathode sintered at 1100°C – 2.22 Ω·cm^2 at 550 °C.

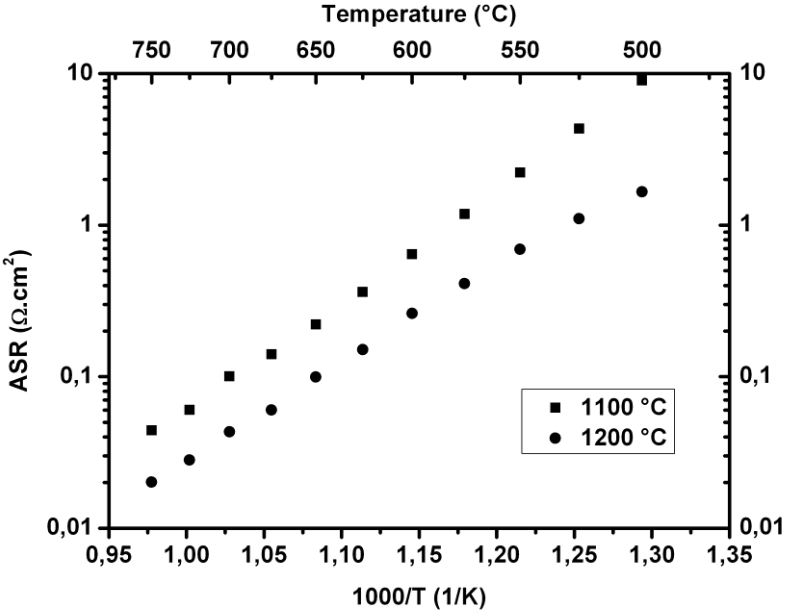

Figure 4. Evolution of the Area Specific Resistance ASR of samples sintered at 1100 and 1200 °C as a function of temperature.

Figure 4 shows the evolution of the ASR as function of temperature for samples sintered at 1100 and 1200 °C; over the whole studied temperature range, both types of samples show Arrhenius behaviour with activation energies of 140kJ/mol or 1.45eV and 120kJ/mol or 1.25eV, respectively. The activation energy of samples sintered at 1100 °C is consistent with literature values [13, 23-25] whereas the activation energy of samples sintered at 1200°C was slightly lower and closer to that of the surface exchange coefficient, 1.01eV according to [26]. In the chapter 3, it was shown that the activation energy of the surface exchange coefficient for dense thin layer was depending on the current collector, 1.45eV for a fine gold mesh current collector and 1.05eV for an identical platinum mesh current collector (difference due to the enhanced dissociation rate of oxygen in presence of the Pt-catalyst). The large Pt-mesh used as current collector might have a small effect on the LSCF sample sintered at 1200°C. This effect is not

observed for sample sintered at 1100°C as it has a higher surface area than the sample sintered at 1200°C.

Figure 5 shows the evolution of the ASR as a function of oxygen partial pressure for samples sintered at 1100 and 1200°C. Both types of samples follow the same trend: the ASR is increasing with decreasing oxygen partial pressure. At high oxygen partial pressure, the ASR is independent of the oxygen partial pressure, whereas at low oxygen partial pressure, a power dependence near -1 is found that indicates a transition to gas diffusion limitation according to [27].

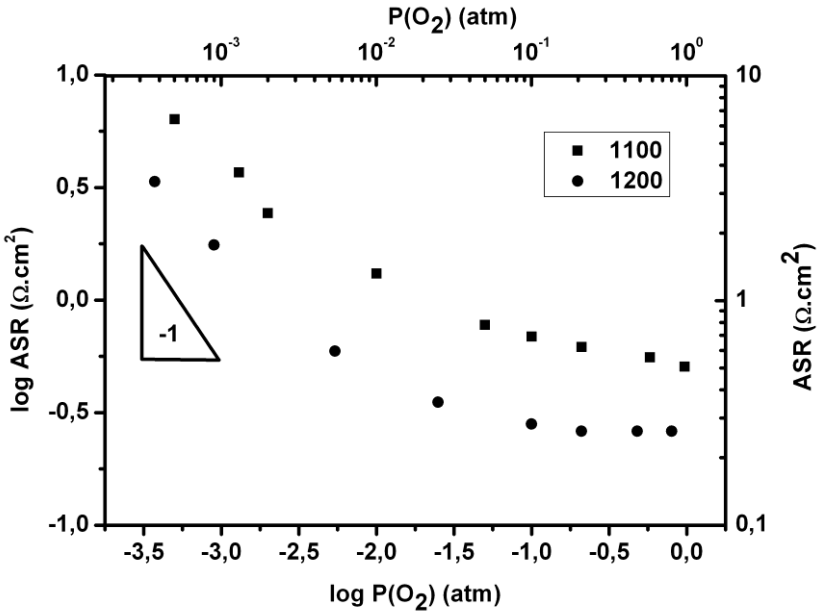

Figure 5. Evolution of the Area Specific Resistance ASR of samples sintered at 1100 and 1200 °C as a function of oxygen partial pressure.

3.3. Modeling with different equivalent circuits.

For all temperatures and oxygen partial pressures, the impedance spectra were fitted with three different equivalent circuits as shown in Figure 1. Here the “Circuit Description Code” developed by Boukamp [22] is used. The first two equivalent circuits have been presented in the introduction. The third one was developed in this study. These 3 different equivalent circuits will be

briefly described. The physical interpretation of the different elements has been described in the introduction and will be discussed in the next paragraphs.

The equivalent circuit ECa consists of a resistance $R_{el'l}$ in series with an inductance L and with two (R_iQ_i) sub-circuits and three (R_iQ_i) sub-circuits at high temperatures only. The inductance is due to the holder, wiring and measuring instrument and was subtracted at first instance when fitting the data. R_{hf}, R_{if} and R_{lf} refer to the high, intermediate and low frequency resistances, respectively.
The equivalent circuit ECb consists of a resistance $R_{el'l}$ in series with an inductance L and with the Gerischer impedance in series with one ($R_{gd}Q_{gd}$) sub-circuits at high temperatures only.

The equivalent circuit ECc consists of a resistance $R_{el'l}$ in series with an inductance L and with the Gerischer impedance in series with one (R_{lf}Qlf) sub-circuit and one ($R_{gd}Q_{gd}$) sub-circuit at high temperatures only. After the Complex Non-Linear Least Squares (CNLS) analysis with the software package “Equivalent Circuit”, residual plots are obtained in which one can see in which frequency domain the model may differ from the measurement.

3.4. Temperature and oxygen partial pressure dependences.

Figure 6 shows the impedance characteristics at 750°C of the sample sintered at 1200 °C and the modelled values corresponding to the different equivalent circuits shown in Figure 1. For the three equivalent circuits considered in this work, the residual plots (see inserts of Figure 6) show that the error remains lower than 1% over the whole frequency range. The three different equivalent circuits are thus more than acceptable.
However, it can be clearly seen that the analysis with equivalent circuit ECb leads to higher residuals than analysis with equivalent circuits ECa and ECc. Already at 750 °C (temperature at which the dispersion is small anyway!), one can observe a shift in the real and imaginary residual plot at frequencies higher than 100Hz indicating that some information is lost during modelling. This problem becomes even more important at lower temperatures. Equivalent circuit ECb is thus clearly not suitable to fit the electrodes

whereas equivalents circuits ECa and ECc both shows very small residuals with errors lower than 0.1% over the whole frequency range.

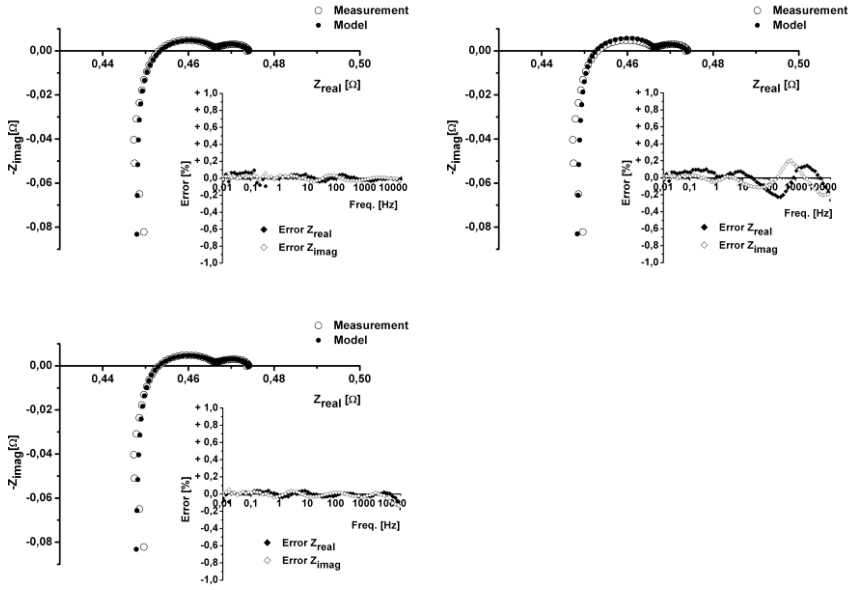

Figure 6. Impedance diagrams for the LSCF samples sintered at 1200 °C measured at 750 °C. Open circles are data points, closed circles are modelled values corresponding to the different equivalent circuits; (top left) ECa, (top right) ECb and (bottom left) ECc. Inserts are the errors plots for each model.

The high frequency cut-off resistance is normally determined by the electrolyte resistance. For the measurements at the lowest temperatures, an additional high frequency semicircle is observed which is attributed to the grain boundary dispersion of the electrolyte. The apparent electrolyte resistance shows Arrhenius behaviour with an activation energy of 64 kJ/mol in accordance with typical values for YSZ electrolytes.

For the measurements at the highest temperatures (see Figure 7: R_{gd} and Q_{gd}), an additional semicircle is observable at the lowest frequencies. As both resistance R_{gd} and constant phase element Q_{gd} are virtually temperature independent this contribution diminishes quickly with decreasing temperature. It shows, however, a strong pO_2 dependence, hence this feature is clearly due to gas diffusion limitation in the porous

electrode. The R_{gd} of ~0.007Ω and a calculated pseudo capacitance C_{gd} of ~15F for the CPE with an *n*-value of ~0.9 in air, strongly support this assignment.

Figure 7 presents the temperature dependence and the oxygen partial pressure dependence of the different parameters of constituting equivalent circuit ECa. The electrode response is modelled with two (RQ) is series. Both resistances R_{hf} and R_{if} follow an Arrhenius behaviour with activation energies of 96 kJ/mol and 131 kJ/mol, respectively. R_{hf} and R_{if} are almost independent of the oxygen partial pressure. Q_{hf} and Q_{if} also show Arrhenius behaviour with activation energies of 80 kJ/mol and 48 kJ/mol respectively and also a strong dependence on the oxygen partial pressure. The coefficient “n” associated to these constant phase elements are around 0.5 and 0.9 for Q_{hf} and Q_{if} respectively. $(RQ)_{hf}$ could thus be ascribed to diffusion and $(RQ)_{if}$ to a capacitive dispersion. In the CNLS analysis, error estimates are calculated for each element (error bars in Figure 7).

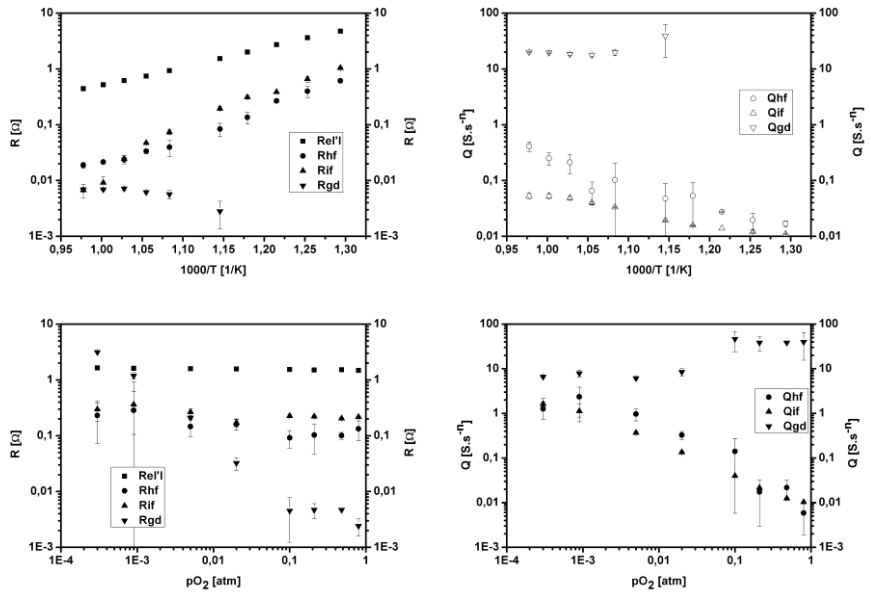

Figure 7. Temperature and oxygen partial pressure dependencies of the element parameters of equivalent circuit ECa for cathodes sintered at 1200°C.

Figure 8 presents the temperature dependence and the oxygen partial pressure dependence of the different parameters from equivalent circuit ECc. The electrode response is modelled with a Gerischer impedance in series with a (RQ). The two parameters of the Gerischer impedance Y_0 and K_a show Arrhenius behaviour with activation energies of -100 kJ/mol and -87 kJ/mol respectively. A small deviation from Arrhenius behaviour can be observed for the lowest temperatures. The oxygen partial pressure dependence order is -0.47 and 0.85, values that are higher than those observed by Adler et al. [8]. R_{hi} and Q_{hi} are also thermally activated and follow Arrhenius behaviour with activation energies of 95 kJ/mol and -64 kJ/mol respectively. The value of "n" for Q_{hi} is lower or equal to 0.5, indicating a diffusion process. In this case, the electrode performance is limited by surface exchange and bulk diffusion.

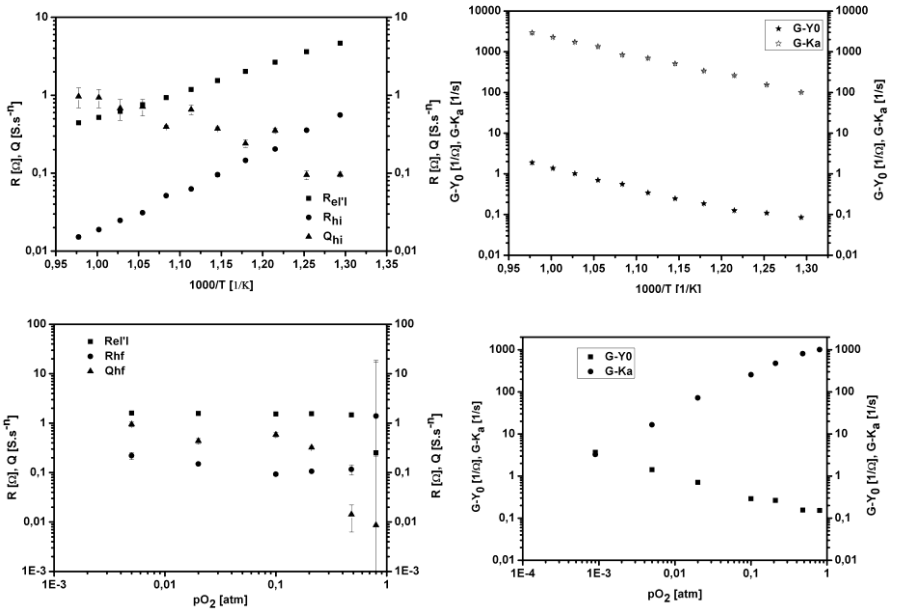

Figure 8. Temperature and oxygen partial pressure dependencies of the element parameters of equivalent circuit ECc for cathodes sintered at 1200°C.

This observation is indicative of a complex reaction mechanism, probably involving more than one rate determining process (*n* values lower or equal to 0.5). It should be realized that porous electrodes are non ideal as compared

to the thin dense electrodes studied in Chapter 3 which were used to study the materials properties.

For the two equivalent circuits, ECa and ECc, the full frequency range χ^2_{CNLS}-values for the different temperatures and different oxygen partial pressures are comparable (see Figure 9), varying between 10^{-6} at low temperatures or low oxygen partial pressure and 10^{-8} at high temperatures. However, the error estimates obtained for each element of the circuit show some major differences (see Figures 7 and 8). Due to a strong overlap of their dispersion, the high frequency and intermediate frequency (RQ) of ECa show significant errors over the whole temperature and oxygen partial pressure range. These errors are much lower for equivalent circuit ECc. Not only offering a phenomenological analysis of the oxygen reduction in the cathode, the CNLS analysis with a Gerischer impedance leads to more trustful values of the equivalent circuit.

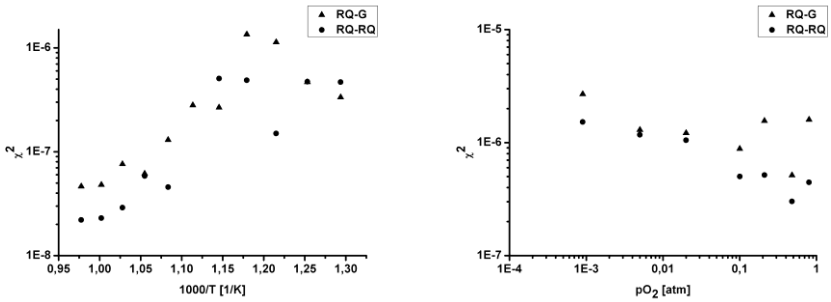

Figure 9. Temperature and oxygen partial pressure dependence of the χ^2_{CNLS}-values obtained in the CNLS analysis over the entire frequency range.

4. Conclusions.

Symmetrical two-electrode cells with different porous microstructures of LSCF cathodes were tested by mean of Electrochemical Impedance Spectroscopy. The different microstructures were obtained using various sintering temperatures after screen-printing. The microstructure of the LSCF cathode had a strong influence on the cell's performance. Cells sintered at 1200°C showed the lowest apparent electrolyte resistance and the lowest Area Specific Resistance with values as low as 0.70 $\Omega \cdot cm^2$ at 550 °C. Both

temperature dependence and oxygen partial pressure dependences showed a limitation by surface exchange. The impedance characteristics of the cell sintered at 1200 °C was analyzed with the CNLS method using different equivalent circuits found in literature. The use of the Gerischer impedance to model LSCF electrodes should be preferred. Not only offering a phenomenological understanding of the electrode processes, the errors inherent to the CNLS analysis are minimized.

References.

[1] Kournoutis V.Ch., Tietz F., Bebelis S., Fuel Cells 09, 6 (2009) 852.

[2] Hjalmarsson P., Soegaard M., Mogensen M., Solid State Ionics 179 (2008) 1422.

[3] Grunbaum N., Dessemond L., Fouletier J., Prado F., Mogni L., Caneiro A., Solid State Ionics 180 (2009) 1448.

[4] Hansen K.K., Hansen K.V., Mogensen M., J. Solid State Electrochem. 14 (2010) 2107.

[5] Barsoukov E., Macdonald J.R., Eds., Impedance Spectroscopy, 2nd Ed., Wiley-International, 2005, pp. 87.

[6] Benson S.J., Chater R.J., Kilner J.A., Proc. 3rd Intern. Symp. on Ionic and Mixed Conducting Ceramics III, The Electrochemical Society Proceedings Series, PV 97-24, (Eds. T.A. Ramanarayanan, W.L. Worell, H.L. Tuller, A.C. Khandkar, M.Mogensen, W.Göpel), Pennington, NJ, USA, 1998, p. 596.

[7] Steele B.C.H., Bae J.-M., Solid State Ionics 106 (1998) 255.

[8] Adler S.B., Lane J.A., Steele B.C.H., J. Electrochem. Soc., 143 (1996) 3554.

[9] Adler S.B., Chem. Rev., 104 (2004) 4791.

[10] Lu Y., Kreller C., Adler S.B., J. Electrochem. Soc., 156 (2009) B513.

[11] Takeda Y., Kanno R., Noda M., Tomida Y., Yamamoto O., J. Electrochem. Soc. 134 (1987) 2656.

[12] Ringuedé A., Fouletier J., Solid State Ionics 139 (2001)167.

[13] Esquirol A., Brandon N.P., Kilner J.A., Mogensen M., J. Electrochem. Soc. 151 (2004) A1847.

[14] Kim Y., Pyun S., Kim J., Lee G., J. Electrochem. Soc. 154 (2007)

B802.
[15] Boukamp B.A., Verbraeken M., Blank D.H.A., Holtappels P., Solid State Ionics 177 (2006) 2539.
[16] Atangulov R.U., Murygin I.V., Solid State Ioncs 67 (1993) 9.
[17] Sluyters-Rehbach M., Sluyters J.H. in: A.J. Bard (Editor), Electrochemical Chemistry vol. 4, Marcel Dekker, New York (1970), p.68.
[18] Sluyters-Rehbach M., Sluyters J.H. in: E. Yeager et al., Comprehensive Treatise of Electrochemistry vol. 9, Plenum, New York (1984), p.274.
[19] Boukamp B.A., Bouwmeester H.J.M., Solid State Ionics 157 (2003) 29.
[20] Boukamp B.A., J. Electrocchem. Soc. 142 (1995) 1885.
[21] Boukamp B.A., Solid Sate Ionics 18-19 (1986) 136.
[22] Boukamp B.A., Solid State ionics 20 (1986) 31.
[23] Sirman J.D., Lane J.A., and Kilner J.A., in Ionic and Mixed Conducting Ceramics III, T. A. Ramanarayanan, W. L. Worrell, H. L. Tuller, A. C. Khandkar, M. Mogensen, and W. Gopel, Editors, PV 97-24, p. 57, The Electrochemical Society Proceedings Series, Pennington, NJ (1997).
[24] Jiang S.P., Solid State Ionics 146 (2002) 1.
[25] Bae J.-M., Steele B.C.H., Solid State Ionics 106 (1998) 247.
[26] Benson S.J., Chater R.J., Kilner J.A., Steele B.C.H., in *3rd Ionic and Mixed Conducting Ceramics III*, T. A. Ramanarayanan, W. L. Worrell, H. L. Tuller, A. C. Khandkar, M. Mogensen, and W. Gopel, Editors, p. 596, The Electrochemical Society Proceedings Series, Pennington, NJ (1997).
[27] Takeda Y., Kanno R., Noda M., Tomida Y., Yamamoto O., J. Electrochem. Soc. 134 (1987) 2656.

Chapter 5.

Improved cathode / electrolyte interface of SOFC

Abstract.

The electrochemical performance of porous $La_{0.6}Sr_{0.4}Co_{0.2}Fe_{0.8}O_{3-\delta}$ (LSCF) cathodes is improved by inserting a dense LSCF layer. A 200 nm thin, layer is deposited on the electrolyte substrate by pulsed laser deposition, prior to the screen printing process. This procedure enhances the adherence of the porous cathode layer to the electrolyte and allows a lower sintering temperature, which reduces grain growth during sintering. In air a decrease in polarization resistance with a factor of 3 is observed for electrodes sintered at 1100°C. The apparent electrolyte resistance is also reduced with the dense PLD layer. A remarkable change in P_{O_2} dependence is observed for the Gerischer parameters that describe part of the electrode impedance, indicating a possible change in the oxygen transfer mechanism.

1. Introduction.

The optimization of the SOFC performance at intermediate temperatures (600-800°C) depends strongly on efficient cathode materials and structures. The $La_{0.6}Sr_{0.4}Co_{0.2}Fe_{0.8}O_{3-\delta}$ perovskite material (LSCF) is an interesting candidate. Its reactivity with the standard zirconia electrolyte can be suppressed by using an yttria-stabilized ceria interlayer. The polarization resistance of the cathode is also dependent on the microstructure and thus on the preparation process [1,2]. In chapter 3, the influence of the sintering temperature on microstructure and polarization resistance of screen printed LSCF cathodes is presented [3]. A very strong sintering temperature dependence was noted, cathodes sintered at 1100°C showed poor adherence, while cathodes sintered at 1300°C suffered from excessive grain growth, leading to a low porosity structure and hence a high polarization resistance. The optimum in cathode properties was found for a sintering temperature of 1200°C. Lowering the sintering temperature has the advantage of smaller grain sizes, which will increase the active surface area for the oxygen exchange and reduction reaction. To improve the adherence of the porous electrode to the electrolyte it is proposed to apply a thin, dense LSCF layer to the electrolyte before the screen printing process. Pulsed Laser Deposition (PLD or laser ablation) has the advantage of stoichiometric transfer and a strong bonding with the substrate of the deposited composition. In this report the performance of a PLD-enhanced cathode structure is studied with electrochemical impedance spectroscopy (EIS) as function of temperature and oxygen partial pressure. The results are compared with the performance of the regular screen printed cathode.

2. Experimental.

Symmetrical two-electrode cells were prepared by tape-casting and screen printing processes. Tape-casted yttria-partially stabilized zirconia (3YSZ, Tosoh) was used as electrolyte. Yttria-doped ceria (YDC, Praxair) was provided as interlayer by screen printing and sintered at 1400°C on both sides of the tape-casted 3YSZ electrolyte. Two identical porous electrodes of $La_{0.6}Sr_{0.4}Co_{0.2}Fe_{0.8}O_{3-\delta}$ (LSCF, Praxair) were then screen printed on both sides of the electrolyte and sintered at 1100°C to complete the reference

samples (further denoted by P). For the PLD-enhanced samples (denoted by DP) dense thin layers of LSCF were deposited by pulsed laser deposition on the YDC interlayer, prior to the screen-printing of the porous LSCF electrodes. The pulsed laser deposition was performed with a KrF excimer laser, using a fluency of 2.6 J/cm^2 and a frequency of 20 Hz. The LSCF target was provided by placing an isostatically pressed LSCF pellet on a rotating holder. The laser ablation occurred in a vacuum chamber in 0.02 mbar oxygen ambient. The YDC/3YSZ/YDC substrates were heated to 750°C during deposition. Schematic representation of the two different samples (P and DP) is presented in Fig. 1.

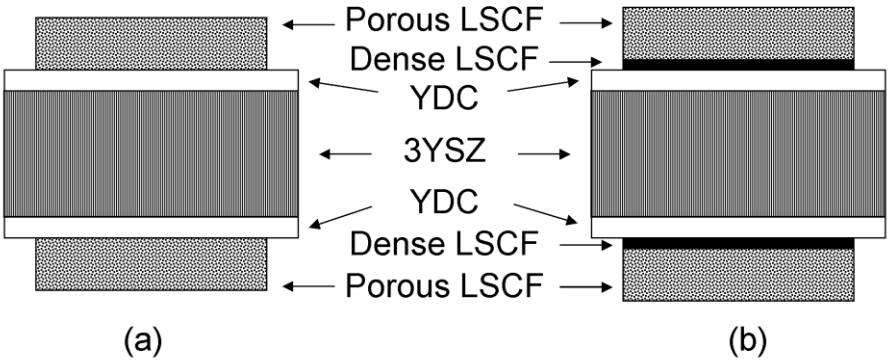

Figure 1. Scheme of (a) sample P and (b) sample DP.

The measurement of the electrochemical properties of the different cells were performed at open-circuit voltage in synthetic air as a function of temperature between 800° and 300°C at 50°C intervals, and as a function of oxygen partial pressure at 600°C. The impedance characteristics were measured with a Solartron 1250 FRA combined with a 1287 electrochemical interface over a frequency range of 65535 Hz to 10 mHz in a pseudo 4-electrode set up (separate current and voltage probe leads). The impedance data were validated with a Kramers-Kronig transform program [4] and analysed with the software package 'Equivalent Circuit' [5].

3. Results and discussion.

3.1. Microstructure.

The cross section of a typical symmetrical cell is shown in the SEM micrograph in Figure 2. The electrolyte thickness is 92μm, the electrodes on both sides of the cell are 53μm thick, the electrode and the electrolyte are separated by a YDC interlayer approximately 3μm thick. Mean grain size of the porous LSCF cathode sintered at 1100°C is 0.50μm (see Figure 3).

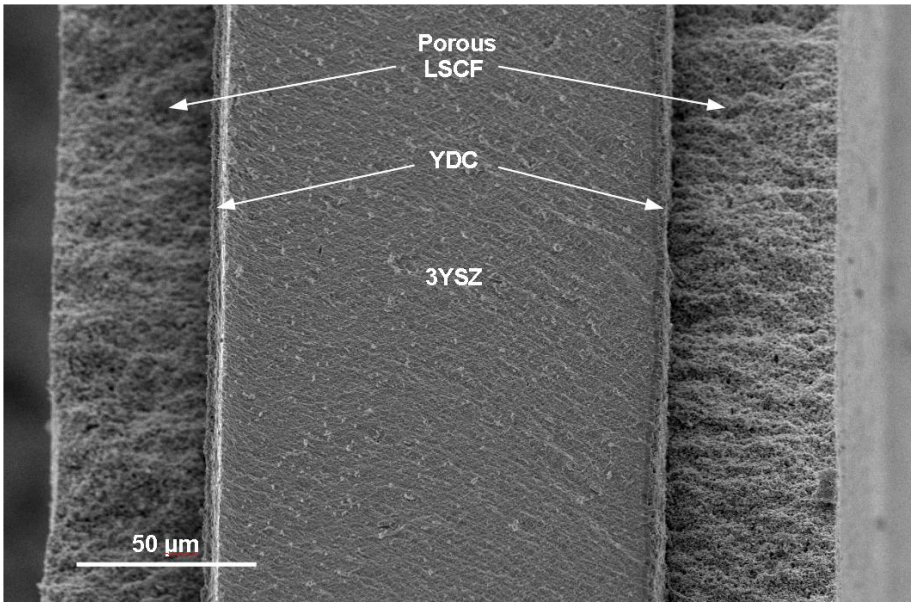

Figure 2. SEM micrograph of a cross section of the symmetrical cell.

In the DP sample the dense PLD-LSCF layer is 200 nm thick, completely covering the rough YDC surface. Figure 4 shows that there is a very good adhesion to the YDC interlayer.

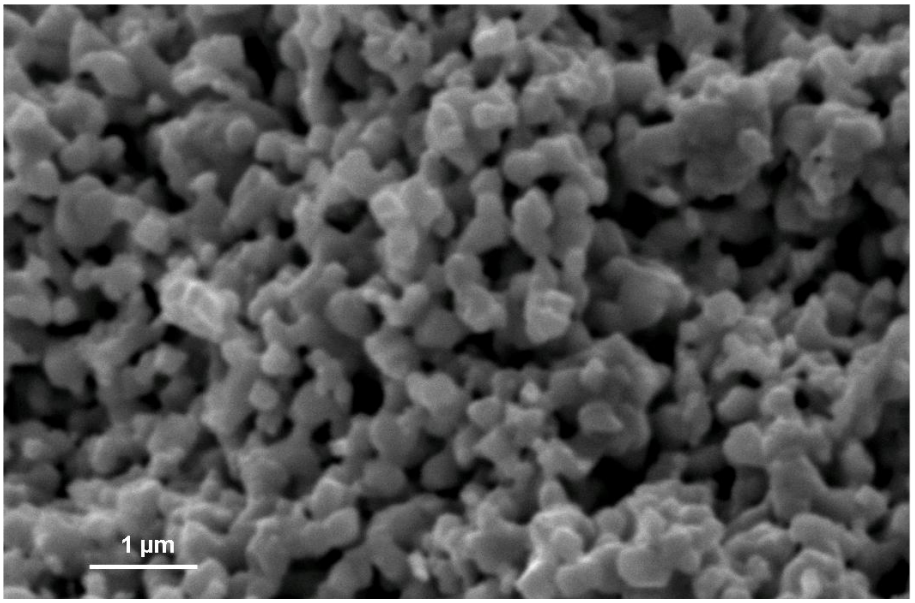

Figure 3. SEM micrograph of the microstructure of the LSCF porous cathode

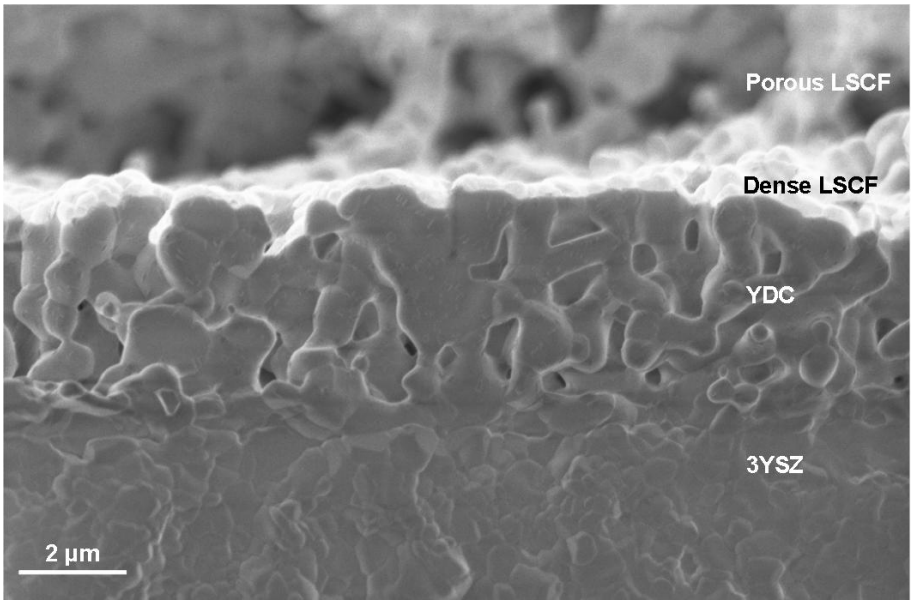

Figure 4. SEM micrograph of a cross section of a symmetrical cell with a LSCF layer deposited by Pulsed Laser Deposition.

3.2. Temperature dependence.

Figure 5a shows the impedance characteristics of the samples D and DP at 400°C in air. The high frequency semicircle that becomes visible at low temperatures is attributed to the grain boundary dispersion of the electrolyte. The low frequency dispersion represents the electrode response. Figure 5b shows the impedance characteristics at 600°C in air. In this range of temperature, only the electrode response can be observed. At high temperatures (800°C, Figure 5c) a low frequency semi-circle develops which can be attributed to gas phase limitation in the porous electrode.

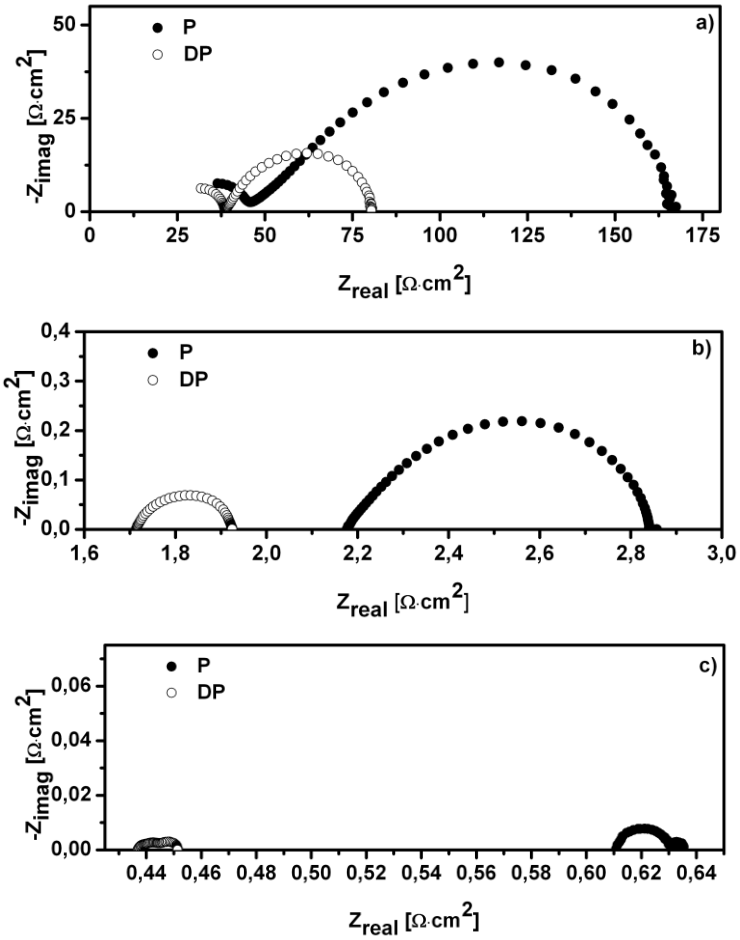

Figure 5. Impedance characteristics of sample D and DP in air at (a) 400°C, (b) 600°C and (c) 800°C.

The introduction of the PLD-LSCF layer results in a decrease of the apparent electrolyte resistance $R_{el'l}$ by a factor 1.25 and of the polarization resistance R_{pol} by a factor of 3, see Figure 5. A comparison of typical values for both samples is presented in Table 1. The temperature dependence of the electrolyte resistance $R_{el'l}$ and the polarization resistance R_{pol} is presented in Figure 6.

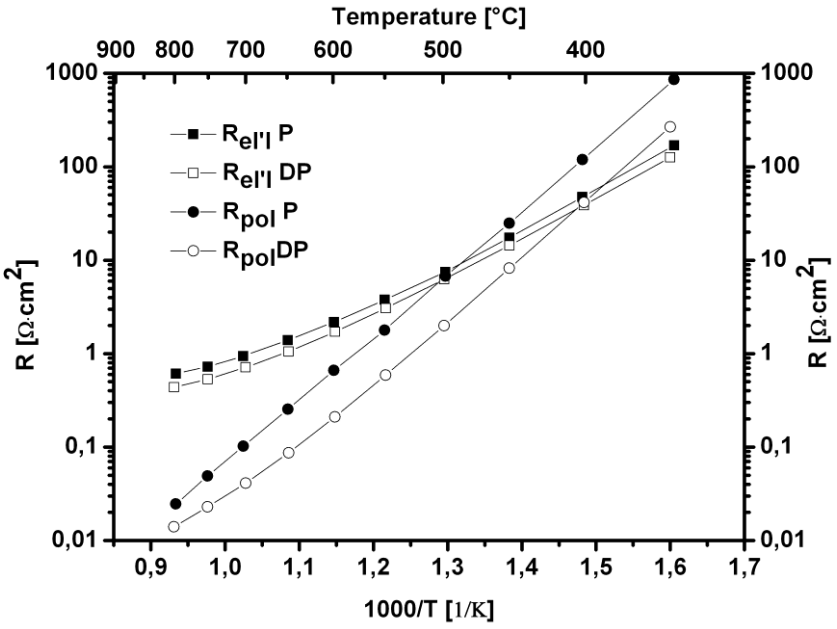

Figure 6. Electrolyte and polarization resistance as a function of temperature in air. The lines are guides for the eyes.

The observed activation energies for the electrolyte conductivity are 0.74eV (DP) and 0.73eV (P). As the YDC/3YSZ/YDC electrolytes are similar for type P and DP samples, the decrease of the electrolyte resistance by a factor of 1.25 for DP samples can only be explained by an improvement in the contact between the electrode and the electrolyte. Gazzarri et al. [6] observed a shift to the right of the electrode dispersion in the impedance graph when comparing a normal electrode and an electrode with delaminated cathode area. This phenomenon was explained by a reduction in the ion conduction area, caused by delamination thus apparently increasing the electrolyte resistance. In the case of type P and DP samples,

a porous electrode with a porosity estimated to 20% covers at most 80% of the surface. Hence by introducing a dense layer, the contact between the electrode and the electrolyte becomes 100% which is a factor 1.25 higher than 80%.

Table 1. Comparison of polarization resistances for samples P and DP in air.

Temperature [°C]		800	600	500
R_{pol}(P)	[Ω·cm^2]	0.025	0.67	6.8
R_{pol}(DP)	[Ω·cm^2]	0.015	0.21	2.0

For the polarization resistances 1.29eV (DP) and 1.34eV (P) are found, which values are consistent with literature data [7-10]. All spectra for both types of samples could be modeled with the equivalent circuit presented in Figure 7. The high frequency grain boundary contribution is only observable at low temperatures, while the low frequency gas phase limitation dispersion is only visible at high temperatures (~800°C).

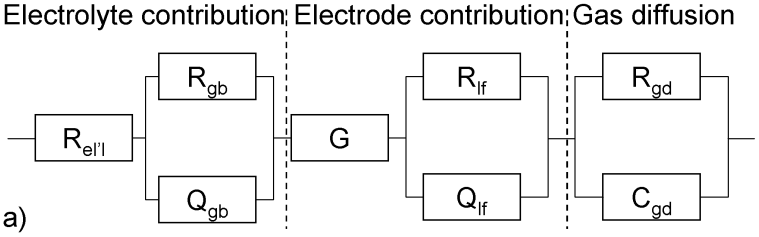

Figure 7. Equivalent circuit used to fit the impedance spectra.

The main feature is the well-documented Gerischer dispersion (or chemical impedance [11-13]), here expressed as:

$$Z_G(\omega) = Z_0 / \sqrt{K_a + j\omega} \qquad (1)$$

Besides this Gerischer element, which is typical for the LSCF-type cathodes, an overlapping semicircle contribution (R_{lf} Q_{lf}) was systematically observed. This dispersion, which has not been reported previously (see chapter 3), is tentatively assigned to the redox process in the LSCF-cathode. The overall CNLS-modelling error was generally less than 1%, as can be seen from the

typical residuals graph in Figure 8 for the measurement of DP sample at 500°C in air. For the DP and P type samples, Z_0 and R_{lf} were following an Arrhenius behaviour with activation energies equal to 0.80eV and 1.31eV, respectively. For the temperature dependence in air, the comparison of the circuit parameters for the DP and P type samples did not reveal significant differences that would directly explain the improved performance of the DP-cathodes. However, as will be shown in the next paragraph, the oxygen partial pressure dependence shows remarkable differences between the DP and P type samples.

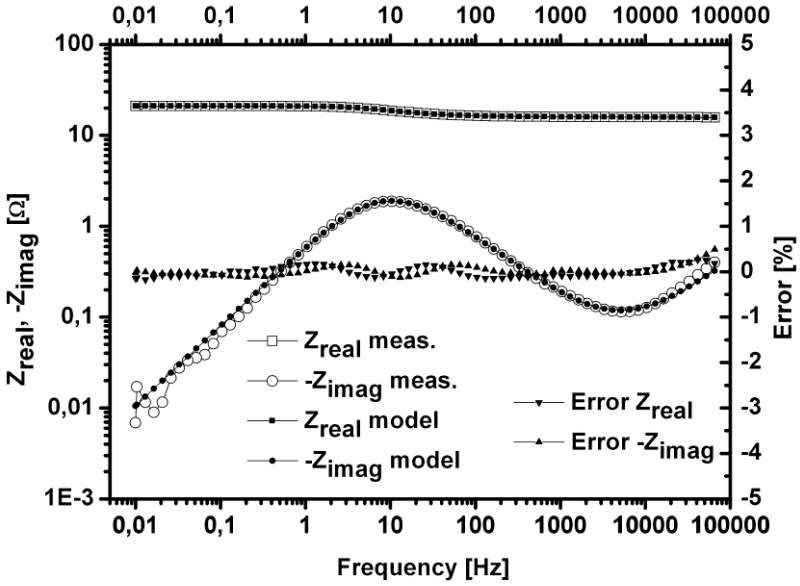

Figure 8. Error between measurement and model as function of frequency for DP sample at 500°C in air. The lines are guides for the eyes.

3.3. Oxygen partial pressure dependence.

The P_{O_2} dependence of both types of cathodes was measured at 600°C. The electrolyte resistance was, as expected, independent of P_{O_2} oxygen partial pressure. The polarization resistance decreases with increasing oxygen partial pressure obeying:

$$R_p = R_0 \cdot P_{O_2}^{-n} \qquad (2)$$

with n = 0.20 for the P-sample and n = 0.17 for the DP-sample (see Figure 9). According to Takeda et al., a $P_{O_2}^{-0.25}$ dependence can be attributed to adsorption and surface exchange limitation [14]. Again, the polarization resistance was reduced by a factor between 3 and 4 when comparing sample DP to sample P.

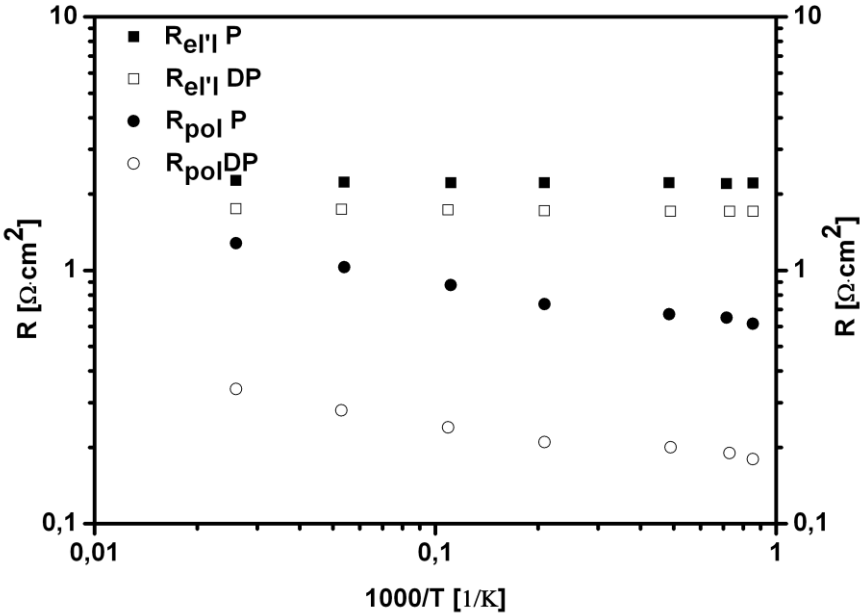

Figure 9. Electrolyte and polarization resistance as a function of oxygen partial pressure at 600°C.

The equivalent circuit presented in Figure 7 is used to model the impedance characteristics of the oxygen partial pressure dependence. The measurements are performed at 600°C, no feature related to gas diffusion limitation is observed. Following the ALS model [11] the Gerischer parameters Z_0 and K_a from eq. (1) are related to material and microstructure parameters by:

$$Z_0 = \frac{RT}{2F^2}\frac{1}{c_v(1-\varepsilon)}\sqrt{\frac{\tau}{D_v}}, \text{ and } K_a = \frac{Aar_0(\alpha_f + \alpha_b)}{c_v(1-\varepsilon)} \quad (3)$$

with c_v the vacancy concentration, ε the cathode porosity, τ the tortuosity. D_v is the vacancy diffusion coefficient, A the thermodynamic factor ($=\partial \ln(P_{O_2}) / 2\partial \ln(c_v)$), a is the specific surface area, r_0 is the exchange neutral flux density and α_f and α_b are constants of the order of unity that depend on the specific mechanism of the exchange reaction [11].

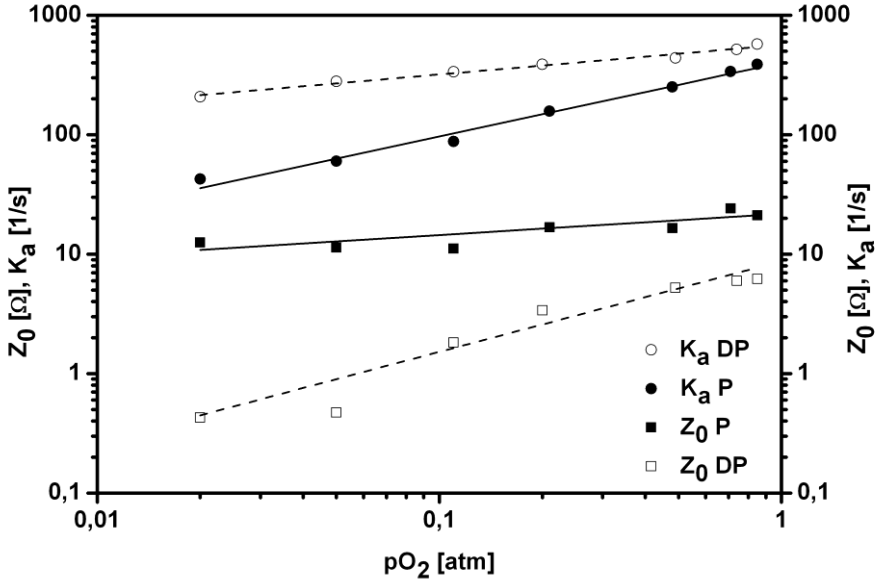

Figure 10. Evolution of Gerischer-parameters of the equivalent circuit as function of the oxygen partial pressure at 600°C. The lines are models.

Figure 10 shows the P_{O_2} dependence of the Gerischer parameters. For the regular porous cathode, P, the P_{O_2} dependence of Z_0 and K_a were $P_{O_2}^{0.17}$ and $P_{O_2}^{0.62}$ respectively. This is in reasonable agreement with the results obtained by Adler et al.: a $P_{O_2}^{0.30}$ dependence for Z_0 and a $P_{O_2}^{0.64}$ dependence for K_a

However, the DP-cathodes showed a much higher P_{O_2} dependence for Z_0, with $Z_0 \div P_{O_2}^{0.76}$, while for K_a the opposite was found: $K_a \div P_{O_2}^{0.25}$, less than half the value for the regular cathode. The addition of a thin dense layer thus seems to change the oxygen reduction/incorporation mechanism significantly. On the one hand, K_a increases by a factor 2 at low P_{O_2} and a factor of 4 at high P_{O_2} for the enhanced DP-cathode, indicating a more effective surface exchange. On the other hand, Z_0 decreases by a factor of 3 at low P_{O_2} and a factor of 30 at high P_{O_2} for the DP-cathode. As the cathode composition is the same for the DP- and P-cathode assemblies, the improvement of the surface exchange can be due to an improved 'footprint' of the cathode on the electrolyte. This allows the transfer of oxygen ions from the cathode bulk to the electrolyte over the entire interface, while the 'triple phase boundary zone' is expanded over the free surface of the thin layer enhancing the transfer through surface diffusion.
Besides the Gerischer parameters, the overlapping semicircle contribution (R_{lf} Q_{lf}) was also studied. Whereas Q_{lf} was nearly P_{O_2} independent, the values for R_{lf} were virtually identical for P and DP type samples and had a reaction order of -0.30. The (R_{lf} Q_{lf}) contribution could thus be attributed to a bulk process in the cathode rather than to the electrolyte / cathode interface.

A qualitative concept is now presented to explain what is assumed to happen in the traditional electrode and what the consequences of the introduction of the dense LSCF layer at the electrode / electrolyte interface are. Adler et al. [11-12] modeled the situation of traditional porous electrodes for mixed ionic electronic conductors such as $La_{1-x}Sr_xCoO_{3-\delta}$. One of their conclusions is that the surface path is much faster than the bulk path. After the dissociative adsorption of the oxygen on the surface of the grain, the oxygen can follow the bulk path, known as a relatively slow path compared to the surface path. The surface path is characterized by a high surface diffusion coefficient. Provided that active sites for oxygen migration are free on the surface, diffusion of adsorbed oxygen species on the surface towards the electrolyte can be fast. Once the oxygen species reaches the electrolyte / cathode interface, it has to be transferred to the electrolyte at the so-called triple phase boundary. If the oxygen species diffusing on the surface of the grain are fully reduced species (e.g. O_{ad}^{2-}), then this charge transfer to the

electrolyte should be quite easy. However, if the diffusing oxygen species are atomic O_{ad} or partly reduced O_{ad}^{-}, then this step can be slow again. The triple phase boundary can then act as a bottle-neck for oxygen transfer after a fast diffusion on the surface. The surface of the cathode grains would then slowly be covered by oxygen species from the interface electrolyte / cathode and fast diffusion can not occur anymore because active sites for diffusion are all occupied by oxygen species waiting to be transferred to the electrolyte. In this case, the oxygen adsorption can also become difficult as the surface of the grains is largely occupied. The effect of surface occupation by oxygen was further studied by Maier et al. [15]

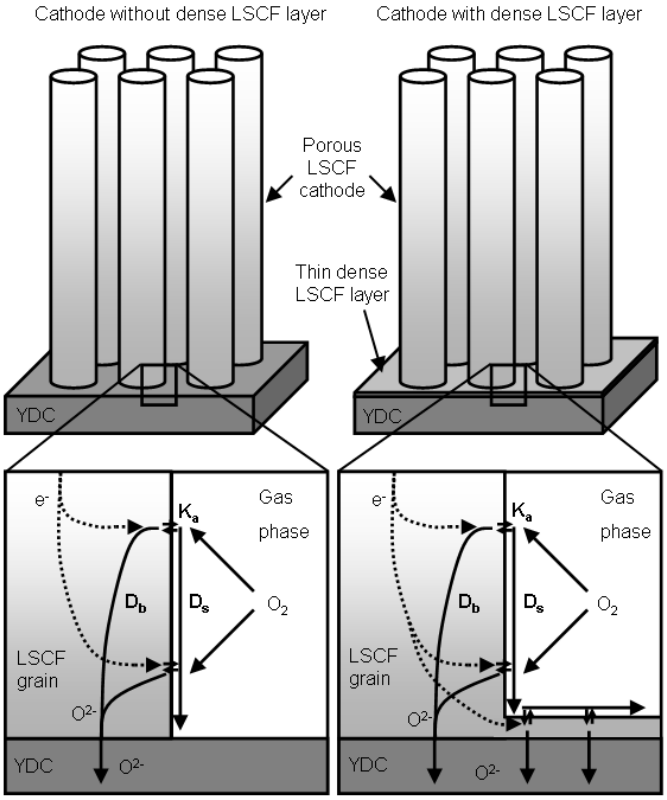

Figure 10. Schematic of the oxygen diffusion depending on the microstructure: effect of addition of a thin dense LSCF layer at the interface electrolyte / cathode.

When adding a dense LSCF layer at the electrolyte / electrode interface (see Figure 11), the triple phase boundary is replaced by the entire exposed surface of the dense layer. When oxygen species diffusing on the surface of the grains of the porous cathode reach the foot of the cathode, it can now diffuse on the surface of the dense LSCF layer. This layer is providing many active sites for oxygen exchange and charge transfer to the electrolyte at a very short distance from the electrolyte. By providing more possibilities for oxygen transfer at the base of the cathode, a higher flux of oxygen species can diffuse via the surface, because this oxygen is drained faster from the LSCF grains surface, making the surface of the grains free for diffusion of oxygen species or for adsorption of oxygen gas molecule. As the surface occupancy is changed the Gerischer parameters would be directly affected. This phenomenon could explain why G-K_a is increased and why G-Z_0 is decreased when a dense LSCF layer is introduced at the electrolyte / electrode interface.

4. Conclusions.

The cathode / electrolyte interface is playing an important role in the overall performance of the cathode. Introduction of a thin, dense $La_{0.6}Sr_{0.4}Co_{0.2}Fe_{0.8}O_{3-\delta}$ layer is introduced by Pulsed Laser Deposition at the electrolyte / cathode interface improves the adherence of the cathode to the electrolyte and allows a lower sintering temperature during the process. A thin, dense LSCF layer results in a decrease of the polarization resistance of the cathode by a factor 3. The oxygen partial pressure dependence shows that the mechanism of oxygen reduction changes possibly indicating an improvement in the surface exchange step. A qualitative concept explaining this improvement and mechanisms change is given. This concept will be further discussed in the next chapter

References.

[1] Lim H.T. et al., J. Power Sources 180 (2008) 92.
[2] Backhaus-Ricoult M., Solid State Sciences, 10 (2008) 670.
[3] Hildenbrand N., Boukamp B.A., Blank D.H.A., in preparation.

[4] Boukamp B.A., J.Electrochem.Soc. 142 [6] (1995) 1885.
[5] Boukamp B.A., Solid State Ionics, 20 (1986) 31.
[6] Gazzarri J.I., Kesler O., J. Power Sources 167 (2007) 430.
[7] Sirman J.D., Lane J.A., Kilner J.A., in Ionic and Mixed Conducting Ceramics III, Ramanarayanan T.A., Worrell W.L., Tuller H.L., Khandkar A.C., Mogensen M., Gopel W., Editors, PV 97-24, p. 57, The Electrochemical Society Proceedings Series, Pennington, NJ 1997.
[8] Jiang S. P., Solid State Ionics, 146 (2002) 1.
[9] Bae J.-M., Steele B. C. H., Solid State Ionics, 106 (1998) 247.
[10] Esquirol A., Brandon N. P., Kilner J. A., Mogensen M., J. Electrochem. Soc., 151 (2004) A1847.
[11] Adler S.B., Lane J.A., Steele B.C.H., J.Electrochem.Soc. 143 (1996) 3554.
[12] Lu Y., Kreller C., Adler S.B., J. Electrochem. Soc. 156 (2009) B513.
[13] Boukamp B.A., Bouwmeester H.J.M., Solid State Ionics 157 (2003) 29.
[14] Takeda Y., Kanno R., Noda M., Tomida Y., Yamamoto O., J. Electrochem. Soc., 134 (1987) 2656.
[15] Fleig J., Merkle R., Maier J., Phys. Chem. Chem. Phys., 9 (2007) 2713.

Chapter 6.

Investigation of $La_2NiO_{4+\delta}$ cathodes to improve SOFC electrochemical performance

Abstract.

The effect of $La_2NiO_{4+\delta}$ cathodes' microstructure on the electrochemical performance is presented. Two types of cathode microstructures are studied, either traditional screen printed porous LNO cathodes sintered at different temperatures, or a combination of a thin dense LNO layer deposited by Pulsed Laser Deposition and of a screen printed porous LNO cathode. The Area Specific Resistance (ASR) is strongly dependent on the sintering temperature of the screen printed layer. Moreover, the introduction of a thin dense LNO layer at the electrolyte / cathode interface strongly reduces the ASR. At 700°C, an ASR of 0.1 $\Omega \cdot cm^2$ is measured for samples with a 800nm thin dense LNO layer combined with a porous LNO layer sintered at 1000°C. It is observed that the Gerischer impedance used to model the electrode behavior was affected by the introduction of the dense layer. A qualitative explanation of this improvement is presented.

1. Introduction.

Intermediate-temperature solid oxide fuel cells (it-SOFC) are possibly high-efficiency and low cost power generation systems. Because of their operating temperature around 600°C, cheaper metallic alloys such as stainless steels can be used as interconnects but other materials than the state of the art $(La,Sr)MnO_{3-\delta}$ have to be used as cathode materials for oxygen reduction. Cobalt-containing perovskites such as $(La,Sr)CoO_{3-\delta}$ and $(La,Sr)(CoFe)O_{3-\delta}$ have been considered as very promising materials due to their high mixed ionic electronic conductivity and to their good oxygen exchange kinetics. However, even at the operating temperatures of it-SOFC, solid state and vapour phase chromium species are transported from the interconnects to the cathode layer [1], decreasing the cathode activity for oxygen reduction, thus degrading the cathode's performance. Various studies have considered the degradation mechanism of materials such as $(La,Sr)CoO_{3-\delta}$ and $(La,Sr)(CoFe)O_{3-\delta}$ [2-6]. Sr-segregation from LSC or LSCF bulk to the surface is playing an important role as Cr reacts with Sr to form different phases: $SrCr_2O_4$, $CoCr_2O_4$ and $(Fe,Cr)_2O_3$ and Cr_2O_3 [6]. Due to the chemical affinity of Cr for Sr and Co to form mixed oxides, cathode materials without Sr and Co might show higher resistance towards chromium poisoning.

Mixed conductors based on the Ruddlesden-Popper phases with the K_2NiF_4-type structure have shown high ionic conductivity and high electrocatalytic activity at 600°C. Skinner et al. [7] showed that the oxygen tracer diffusion coefficient of lanthanum nickelate $La_2NiO_{4+\delta}$ (LNO) is higher than that of LSM and LSCF. The ionic conductivity of $La_2NiO_{4+\delta}$ could thus be higher than that of LSM and LSCF. It should be realized, however, that LNO is a layered structure presenting strong anisotropy and with oxygen diffusion occurring mainly in two dimensions. Different studies have been performed on $La_2NiO_{4+\delta}$ to investigate its electrochemical performance on different types of electrolytes such as Yttria Stabilized Zirconia (YSZ) [8-10] or Cerium Gadolinium Oxide (CGO) [11].

This work focuses on the preparation and the characterization of $La_2NiO_{4+\delta}$ cathodes on an Yttria Doped Ceria interlayer deposited on YSZ electrolytes. Different cathode microstructures are studied; the effect of the cathode's sintering temperatures and the effect of a dense LNO layer at the electrolyte

/ electrode interface are investigated. In a previous report, we have shown for LSCF cathodes that such a dense layer enhances the electrode properties by lowering the Area Specific Resistance (ASR) [11, 12]. The aim is to reduce the ASR to a value of 0.1 $\Omega \cdot cm^2$ at the lowest temperature possible. In this study, a dense $La_2NiO_{4+\delta}$ layer is deposited by Pulsed Laser Deposition in order to obtain a well defined layer with a full coverage of the electrolyte / electrode interface.

2. Experimental.

Symmetrical two-electrode cells were prepared by tape-casting and screen printing. Tape-casted yttria-partially stabilized zirconia (3YSZ, Tosoh) was used as electrolyte. Yttria-doped ceria (YDC, Praxair) was provided as interlayer by screen printing and sintered at 1400 °C on both sides of the tape-casted 3YSZ electrolyte. Two identical porous electrodes of $La_2Ni_{4+\delta}$ (LNO, Cerpotech, mean particle size 170 nm) were then screen printed on both sides of the electrolyte and sintered at different temperatures: 900 °C, 1000°C and 1100 °C.

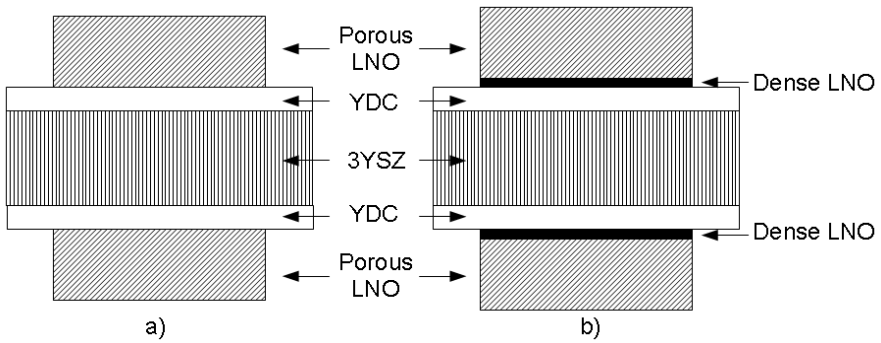

Figure 1. Schematic representation of a sample without (a) and with (b) a thin dense LNO layer between the YDC interlayer and the porous LNO electrode.

For the PLD-enhanced samples, dense thin layers of LNO of different thicknesses were deposited by pulsed laser deposition on the YDC interlayer, prior to the screen-printing of the porous LNO electrodes. The

pulsed laser deposition was performed with a KrF excimer laser, using a fluency of 1.5 J/cm^2 and a frequency of 10 Hz. The LNO target was provided by placing an isostatically pressed and sintered LNO pellet on a rotating holder. The laser ablation occurred in a vacuum chamber in 0.02 mbar oxygen ambient. The YDC/3YSZ/YDC substrates were heated to 850 °C during deposition. Schematic representation of the two different samples, either with or without dense layer is presented in Figure 1. The measurement of the electrochemical properties of the symmetrical cells was performed at open-circuit voltage using Pt mesh as current collector. The temperature dependence between 800° and 300 °C in synthetic air and the oxygen partial pressure dependence at 600 °C was studied. The impedance characteristics were measured with a Solartron 1250 FRA combined with a 1287 electrochemical interface over a frequency range of 65,535 Hz to 10 mHz in a pseudo 4-electrode set up (separate current and voltage probe leads). The impedance data were validated with a Kramers–Kronig transform program [13] and analyzed with the software package 'Equivalent Circuit' [14].

3. Results and discussion.

3.1. Microstructure.

The cross section of half of a typical symmetrical cell is shown in the SEM micrograph in Figure 2a. The electrolyte thickness is 82 µm, the electrode and the electrolyte are separated by a YDC interlayer approximately 3 µm thick.

The thickness of the electrodes on both sides of the cell and the average grain size of the porous LNO cathodes are depending on the sintering temperature (see table 1 and Figure 2b-c-d). The higher the sintering temperature is, the larger the average grain size becomes. Average grain size varies between 255 nm when sintered at 900 °C and 565 nm when sintered at 1100 °C.

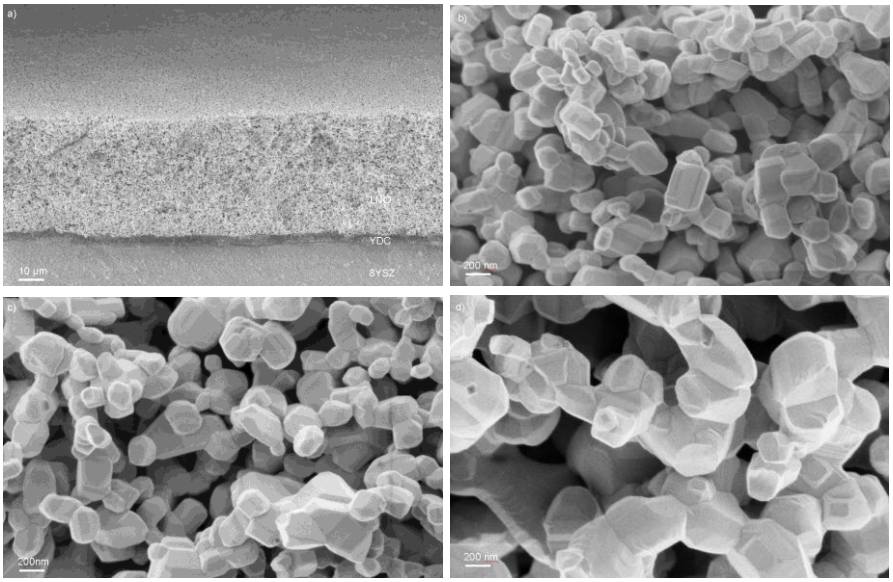

Figure 2. (a) SEM micrographs of a cross section of a symmetrical cell sintered at 1000 °C. SEM micrographs of the microstructure of a LNO porous cathode sintered at (b) 900 °C, (c) 1000 °C and (d) 1100°C.

Table 1. Name and parameters of the different samples.

Sample name	P09	P10	P11	DP2	DP4	DP8
Sintering temperature of porous electrode (°C)	900	1000	1100	1000	1000	1000
Thickness of porous electrode (µm)	50	46	37	46	46	46
Average grain size (nm)	255	340	565	340	340	340
Presence of thin dense LNO layer (by PLD)	No	No	No	Yes	Yes	Yes
Thickness of thin dense LNO layer (nm)	n.a.	n.a.	n.a.	~ 200	~ 400	~ 800

The dense PLD-LNO layers have different thicknesses ranging from 200 nm to 800 nm, completely covering the rough YDC surface. Figure 3a shows a cell with a 400nm LNO layer deposited by PLD and annealed at 900 °C for 2 hours in air prior to screen-printing of the electrode. The adhesion between the PLD-LNO layer and the YDC interlayer is excellent. The YDC interlayer is quite rough but the 400nm thick PLD-LNO layer is completely covering the

surface. The same coverage geometry was observed for samples with a 800nm thick PLD-LNO layer. However, as shown in Figure 3b, a PLD-LNO layer of 200nm is too thin to completely cover the surface because of the relative roughness of the screen-printed YDC interlayer. The surface of the YDC interlayer shows open pores. The PLD-LNO is deposited at the bottom of the pores but it does not cover or close all the pores.

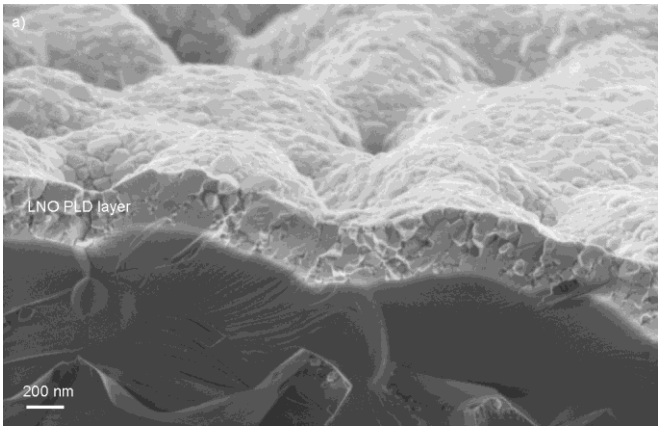

Figure 3. (a) SEM micrograph of a cross section of a symmetrical cell with a 400nm PLD-LNO layer prior to screen-printing of the electrode.

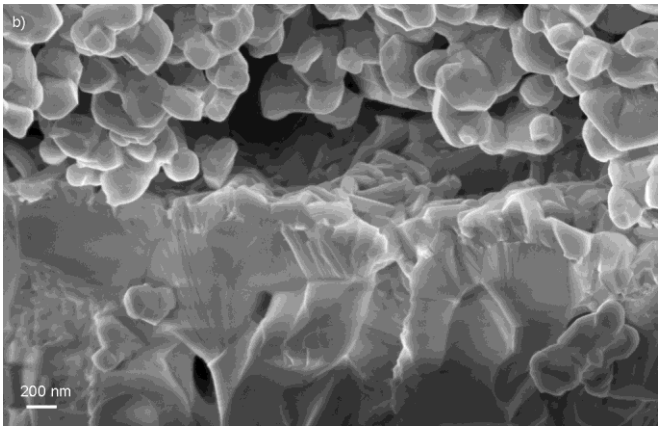

Figure 3. (b) SEM micrograph of a cross section of a symmetrical cell with a 200nm PLD-LNO layer and screen-printed electrode.

3.2. XRD characterization.

An XRD pattern of the LNO/YDC/YSZ/YDC sample shows that the lanthanum nickelate layer is mostly amorphous after pulsed laser deposition on the ceria interlayer (see Figure 4). The only, barely visible, reflections are the (004) and (103), indicating a very small grain size. Both polycrystalline YSZ and YDC patterns are visible. Next, the sample is annealed in air at 900 °C for 2 hours with a ramp of 4 °C/min. After annealing, the LNO film is clearly polycrystalline. The films are grown on polycrystalline screen printed YDC films. As expected, all (*hkl*) reflections are observed, which indicates that there is no preferred degree of orientation.

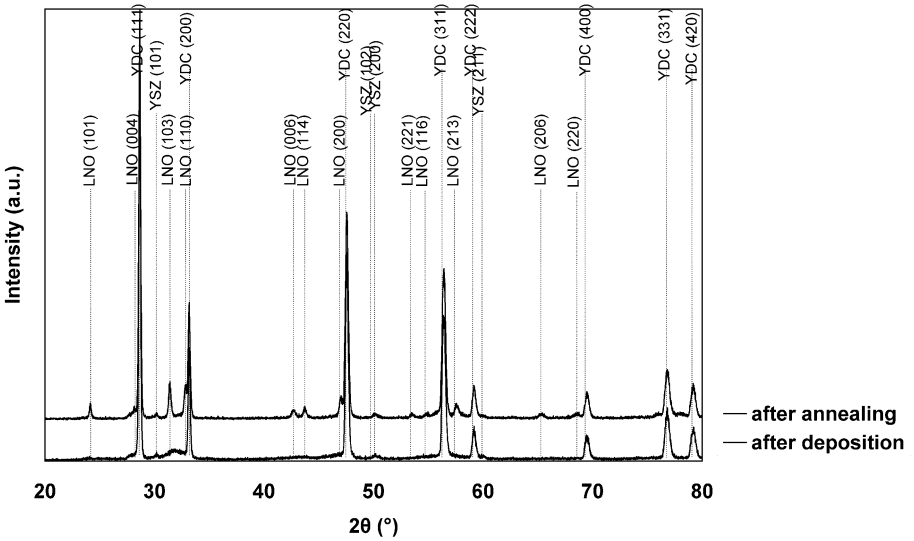

Figure 4. XRD patterns of the LNO/YDC/YSZ/YDC sample directly after Pulsed Laser Deposition and after annealing.

3.3. Effect of sintering temperature and of the PLD layer on the polarization resistance.

The effect of the sintering temperature of the samples on the polarization resistance as obtained from impedance analysis can be observed in Figure 5 and Figure 6. Samples denoted P09, P10 and P11 are sintered at 900°C, 1000 °C and 1100 °C, respectively. The polarization resistance of sample P11 is clearly the highest over the whole temperature range and oxygen

partial pressure range. Sample P10 shows the lowest polarization over the whole temperature range and oxygen partial pressure range. For the ASR, the three types of samples follow an Arrhenius behaviour over the whole temperature range with comparable activation energies around 0.90 eV. These activation energies are slightly lower than the one measured on 8YSZ electrolytes [15]. Over the oxygen partial pressure range, a power dependence around -0.3 is found for the polarization resistance which can be attributed to a limitation by adsorption and surface exchange according to Takeda et al.[16]. Other authors [17-18] interpreted this dependence as a reaction controlled by the atomic oxygen diffusion process followed by a charge transfer.

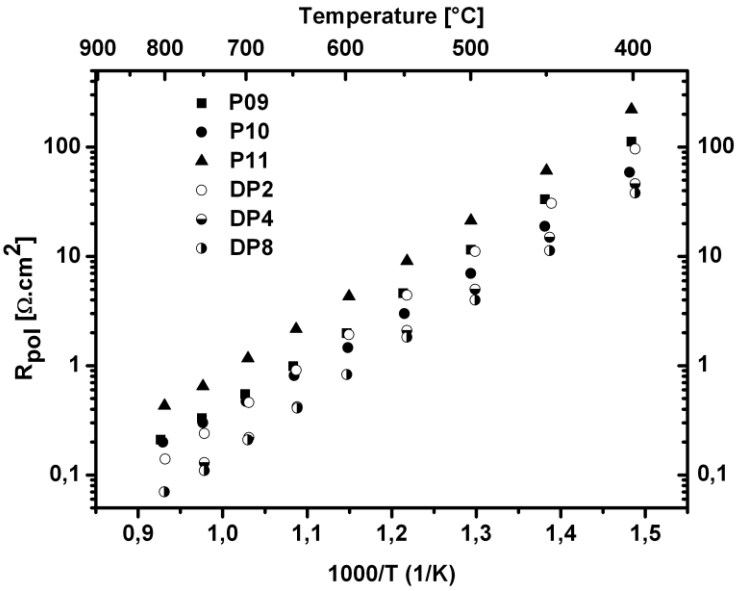

Figure 5. Temperature dependence of the polarization resistances of the different type of samples in air.

The addition of a dense LNO layer between the porous LNO layer and the YDC interlayer is not changing the activation energy of the temperature dependence and the power dependence over the oxygen partial pressure range. The samples DP2, DP4 and DP8 with a dense LNO layer of 200 nm, 400 nm and 800 nm, respectively should be compared to sample P10, as the screen printed layer on top of the dense layer was also sintered at 1000 °C. By adding a 200 nm dense LNO layer, polarization resistances were

slightly increased. However, by adding 400 nm and 800 nm dense LNO layers, polarization resistances were significantly reduced by factor 3 at high temperatures and by a factor 1.5 at low temperatures (see Figure 5 and Figure 6). Similar trends were observed by Rieu et al [11]. They explained this by considering that the increasing number of contact points at the electrode-electrolyte interface would decrease the contribution of the interface polarization resistance. This explanation cannot explain the difference between the different thicknesses and especially explain why sample DP8, with the thickest dense layer, gives the best performance. Study and modeling of the impedance spectra are needed to understand these observations.

As the measurements are performed with symmetrical cells, the measured polarization resistance must be divided by 2 to obtain the Area Specific Resistance (ASR). Without any dense LNO layer, samples P10 have an ASR of 0.7 $\Omega \cdot cm^2$ at 600°C and 0.10 $\Omega \cdot cm^2$ at 800°C. With a dense LNO layer, samples DP8 have an ASR of 0.42 $\Omega \cdot cm^2$ at 600°C and 0.04 $\Omega \cdot cm^2$ at 800°C. The target value of the ASR = 0.1 $\Omega \cdot cm^2$ is reached at 700°C for samples DP4 and DP8.

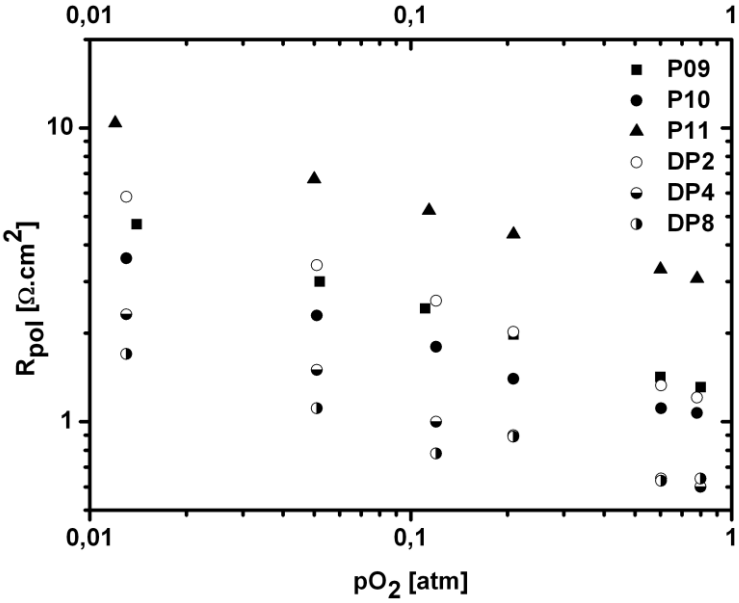

Figure 6. Oxygen partial pressure dependence of the polarization resistances of the different type of samples at 600°C.

3.4. Electrical characterization.

3.4.1. Description of the impedance spectra.

Typical impedance spectra of a LNO/YDC/YSZ/YDC/LNO symmetrical cell sintered at 1000°C are shown in Figure 7. At 750 °C in air, two distinctive features are observable, interpreted as electrode response and gas diffusion limitation in the porous cathode. The virtually temperature independent gas diffusion impedance becomes insignificant with decreasing temperature to 600°C as the polarization is strongly thermally activated and increases rapidly. At low temperatures (350 °C in Figure 7), another feature is observed at high frequencies which is attributed to a grain boundary impedance of the electrolyte. To determine the physical or chemical processes corresponding to those features, temperature dependence and oxygen partial pressure dependence are measured. The equivalent circuit used to model the impedance spectra is shown in Figure 8.

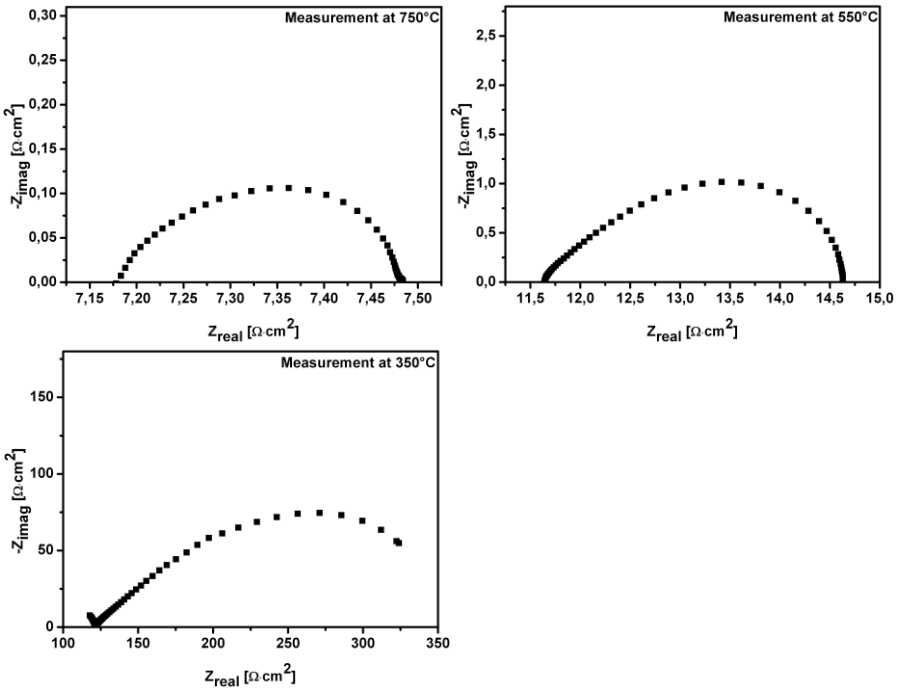

Figure 7. Impedance spectra of sample P10 in air at 750 °C, 550 °C and 350 °C in synthetic air.

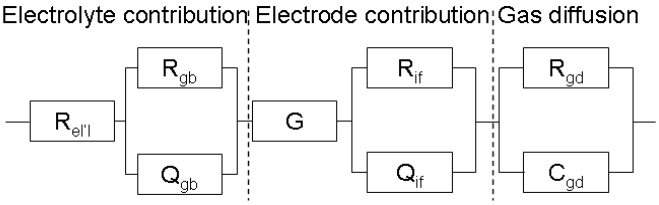

Figure 8. Equivalent circuit used to model the impedance spectra. Subcircuits and elements are arranged with increasing time constant.

3.4.2. Equivalent circuit explanation valid for all types of samples.

For the measurements at the highest temperatures, the depressed semicircle observed at low frequencies is overlapping with the electrode response as the temperature decreases. Both resistance and constant phase element CPE (R_{gd} and Q_{gd}) are independent of temperature. The power n associated with the CPE Q_{gd} is higher than 0.90, very close to the value of a real capacitance. The pseudo-capacitance that can be extrapolated from the CPE Q_{gd} has a high value around 10 F. This feature can thus be associated to gas phase limitation in the porous electrode [19-20].

The high frequency cut-off resistance is generally determined by the total electrolyte resistance. For the measurements at the lowest temperatures, a high frequency feature can be attributed to the grain boundary resistance in the electrolyte. The apparent electrolyte resistance measured at high temperatures is more than one order of magnitude higher than the one expected for the YDC/YSZ/YDC electrolytes. This resistance does not show a single Arrhenius behavior over the whole temperature range (see Figure 9). The temperature dependence can be decomposed in two domains: at low temperatures, the apparent electrolyte resistance follows an Arrhenius behavior with an activation energy E_a = 0.88eV in agreement what is expected for the YDC/YSZ/YDC electrolytes for ionic conductivity [21-22]. However, at high temperatures, the electrolyte resistance follows an Arrhenius behavior with a much lower activation energy E_a = 0.08eV. This

phenomenon points to limitation by the electronic conductivity of the LNO cathodes at high temperatures. The electronic sheet resistance of the LNO electrodes is apparently too high to be ignored.

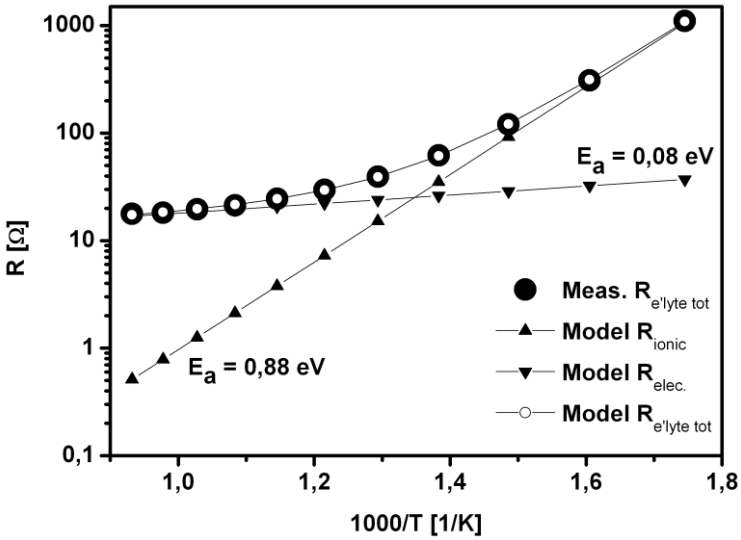

Figure 9. Measurement and modeling of the electrolyte resistance behaviour as function of temperature.

Table 2 indicates the fitting parameters from the equivalent circuit presented in Figure 8 at different temperatures and Table 3 presents the activation energies from the Arrhenius graph of each element as function of temperature, the power dependence of each element as function of the oxygen partial pressure. The parameters associated to the electrolyte (grain boundary limitation at high frequencies / low temperatures and the parameters associated to the gas diffusion limitation at low frequencies and high temperatures are not presented.

The main feature is the well-documented Gerischer dispersion (or chemical impedance [23-25]), here expressed as:

$$Z_G(\omega) = \frac{Z_0}{\sqrt{K_a + j\omega}} = \frac{1}{Y_0\sqrt{K_a + j\omega}} \qquad (1)$$

Important parameters of the Gerischer impedance were analyzed to understand this behaviour, with:

$$Z_0 = \frac{1}{Y_0} = \frac{RT}{4F^2}\frac{1}{c_0 x_v^0 (1-\varepsilon)}\sqrt{\frac{A^0}{D_v(1+2\nu)}} \quad (2)$$

$$K_a = \frac{4A^0 a R_0}{x_v^0 c_0 (1-\varepsilon)} \quad (3)$$

where c_0 is the molar concentration of oxygen lattice sites, x_v^0 is the mole fraction of oxygen vacancies in the limit of equilibrium with the ambient, A^0 is a thermodynamic factor in the limit of equilibrium with the adjoining gas, ε is the porosity, D_v is the vacancy diffusion coefficient, a is the surface area, R_0 is the exchange neutral flux density, $\nu = \frac{oxygen \cdot surface \cdot transport}{oxygen \cdot bulk \cdot transport}$ is a dimensionless number representing the competition between surface and bulk diffusion [24].

The Gerischer parameters G-Y_0 and G-K_a given by equation (2) and (3) are in the same order of magnitude for sample types P09, P10 and P11. The activation energies of the temperature dependence are around 30-40 kJ/mol and 145 kJ/mol, respectively. The activation energy of G-K_a is very close to the activation energies equal to 140kJ/mol calculated by Bouwmeester et al. from a novel pulse ^{18}O–^{16}O isotopic exchange technique for the rapid determination of the oxygen surface exchange rate of $La_2NiO_{4+\delta}$ [26]. Y_0 is independent of the oxygen partial pressure and the pO_2 dependence of K_a is around 0.25.

However, the resistance and constant phase element CPE ($R_{if}Q_{if}$) in series with the Gerischer impedance at intermediate frequencies is strongly dependent on the sintering temperature. The activation energies of the temperature dependence in air (E_a = 93 kJ/mol for R_{if}) and the power of the oxygen partial pressure dependence (m = 0.36 for R_{if}) remain similar but the order of magnitude is completely changed. R_{if} is much lower for P10 than for P09 and P11 which explains why the polarization resistance of P10 is the lowest among the three types of sample. The pseudo-capacitances that can be extrapolated from the constant phase element Q_{if} have values around

10^{-3}-10^{-4} F. They slightly increase with decreasing oxygen partial pressure and decreasing temperature. According to [27], this process could be attributed to an oxygen atom diffusion followed by a charge transfer. An alternative interpretation is a (partial) redox process in the thin layer, i.e. a chemical capacitance.

Sample type		P09	P10	P11	DP4	DP8
G-Y_0 [S]	400°C	0.0044	0.010	0.0056	0.075	0.15
	600°C	0.017	0.039	0.015	0.87	0.7
	800°C	0.027	0.033	0.012	n.a.	1.7
G-K_a [s^{-1}]	400°C	0.79	11	1.7	1.1	0.17
	600°C	1200	900	2900	250	510
	800°C	45000	61000	$1.1 \cdot 10^5$	n.a.	6700
R_{if} [Ω]	400°C	23	120	450	100	77
	600°C	3.5	2.2	10	2.0	2.0
	800°C	0.47	0.44	1.1	0.21	0.16
Q_{if} [$S.s^{-n}$]	400°C	0.0037	0.0076	0.0026	0.021	0.039
	600°C	0.0023	0.0045	0.022	0.010	0.018
	800°C	0.0013	0.0035	0.017	0.0068	0.010

Table 2. Values of the electrode's parameters with the different microstructures at different temperatures.

Sample type		P09	P10	P11	DP4	DP8 high temp	DP8 low temp
G-Y_0	E_a	32	29	42	40	4	68
	pO_2	0	0	0	0.13	0.12	
G-K_a	E_a	141	145	157	94	153	
	pO_2	0.23	0.23	0.24	-0.7	0	
R_{if}	E_a	92	93	87	93	94	
	pO_2	-0.36	-0.37	-0.36	-0.34	-0.25	
Q_{if}	E_a	15	15	11	17	16	
	pO_2	-0.20	-0.19	-0.19	0.01	0	

Table 3. Activation energies (kJ/mol) of the temperature dependence and power dependence as function of oxygen partial pressure (order: n) of the electrode's parameters.

3.4.3. Equivalent circuit explanation valid for samples with a dense LNO layer.

The introduction of a dense LNO layer at the interface between the electrolyte and a porous LNO layer similar to P10 is clearly changing the Gerischer parameters. The DP4 and DP8 cathodes showed a pO_2 dependence for G-Y_0 (m = 0.13) whereas it was independent of the oxygen partial pressure for P09, P10 and P11. The values of G-Y_0 were increased by a factor 10 compared to P10. The values of G-K_a for DP4 and DP8 showed similar or lower values than that for P10, the activations energies of the temperature dependence and the power of the oxygen partial pressure dependence were hardly changed. Both R_{if} and Q_{if} showed the same temperature dependence for DP4 and DP8 and for P10 but the values of Q_{if} are increased by a factor 2 for DP4 and by a factor 4 for DP8 compared to P10. Q_{if} becomes pO_2 independent with the introduction of a dense LNO layer and the pO_2 dependence of R_{if} is hardly changed.

Finally, with the introduction of a dense LNO layer, a feature modeled with a ($R_{hf}Q_{hf}$) appears at the high frequencies. The resistance of this arc increase with decreasing temperatures, Q_{hf} has values between 0.01 and 1 $(F.s)^{1-n}$ with n values around 0.5, an activation energy of 42 kJ/mol and is almost independent of oxygen partial pressure. These high Q values indicate that it is probably related to a bulk process and because n ~ 0.5 it can be interpreted as a diffusion process.

3.5. Discussion.

3.5.1. Discussion of the LNO samples.

Compared to samples P10, the polarization resistances of the samples DP4 and DP8 are improved by a factor up to 3 for both types of samples at high temperatures and at low temperatures by a factor 1.28 – 1.55, respectively. As shown previously, this improvement is mainly due to the increase of the parameter G-Y_0 at the different temperatures and oxygen partial pressures. On the other hand, with the introduction of a dense layer at the interface, a high frequency feature appears at high frequencies and should be

associated with a bulk process according to the capacitance values and the contribution of ($R_{if}Q_{if}$) is slightly increasing. The chemical capacitance associated to the dense layer was evaluated according to the analysis performed in Chapter 3 [28]:

$$C_{chem} = \frac{1}{Z_0\left[\frac{1}{l} + \frac{k}{\tilde{D}}\right]}$$

where k = K_a is the surface exchange coefficient, $\tilde{D}$ is the chemical diffusion coefficient of oxygen and l is the thickness of the dense layer. For a 800nm dense LNO layer, the chemical capacitance was calculated to be C_{chem} = 2.3 F at 800°C in air. The capacitance associated to the high frequency ($R_{hf}Q_{hf}$) is equal to 1 F at 800°C, a value in reasonable agreement with the evaluation according to theory.

The improvement of G-Y_0 by a factor 10 explains the reduction of the polarization resistance. It is important to note that the expression of Y_0 given in equation (2) is a simplification of Y_0 that does not consider surface diffusion as explained by Boukamp and Bouwmeester [25]. When the surface diffusion of oxygen species is considered, two parallel paths for oxygen diffusion towards the electrolyte are possible, either surface diffusion or surface exchange and bulk diffusion. Adler et al. [23-24] modeled this situation for mixed ionic electronic conductors such as $La_{1-x}Sr_xCoO_{3-\delta}$. One of their conclusions is that the surface path is much faster than bulk path. Figure 10 represents a qualitative concept of what is assumed to happen in the traditional porous electrode. After the dissociative adsorption of the oxygen on the surface of the grain, the oxygen can follow the bulk path, know as a relatively slow path compared to the surface path. The surface path is characterized by a high surface diffusion coefficient. Provided that active sites for oxygen migration are free on the surface, diffusion of adsorbed oxygen species on the surface towards the electrolyte can be fast. Once the oxygen species reaches the electrolyte / cathode interface, it has to be transferred to the electrolyte at the so-called triple phase boundary. If the oxygen species diffusing on the surface of the grain are fully reduced

species (e.g. O_{ad}^{2-}), then this charge transfer to the electrolyte should be quite easy. However, if the diffusing oxygen species are atomic O_{ad} or partly reduced O_{ad}^{-}, then this step can be slow again. In that case, the triple phase boundary will act as a bottle neck, forcing most of the oxygen flux to pass through the bulk of the porous structure. In fact, the surface concentration gradient will be almost 'flat' at the triple phase boundary. The effect of surface occupation by oxygen has been studied in details by Maier et al. [29].

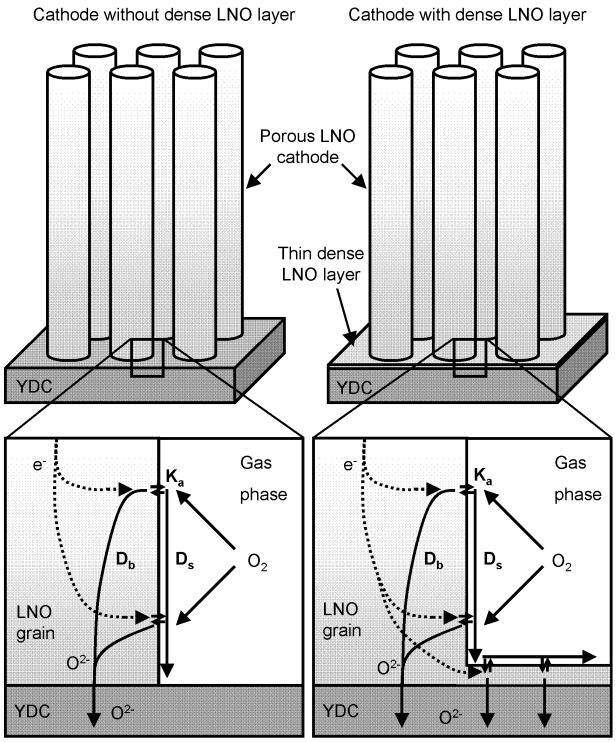

Figure 10. Schematic of the oxygen diffusion depending on the microstructure: effect of addition of a thin dense LNO layer at the interface electrolyte / cathode.

When adding a dense LNO layer at the electrolyte / electrode interface (see Fig. 10), the triple phase boundary is replaced by the entire exposed surface of the dense layer. When oxygen species diffusing on the surface of the grains of the porous cathode reach the foot of the cathode, it can now diffuse on the surface of the dense LNO layer. This layer is providing many active sites for oxygen exchange and charge transfer to the electrolyte at a very short distance from the electrolyte. By providing more possibilities for oxygen transfer at the base of the cathode, a higher flux of oxygen species can diffuse via the surface, because this oxygen is drained faster from the LNO grains surface, making the surface of the grains free for diffusion of oxygen species or for adsorption of oxygen gas molecule. As the surface occupancy is changed the Gerischer parameters would be directly affected. This phenomenon could explain why G-Y_0 is increased when a dense LNO layer is introduced at the electrolyte / electrode interface.

3.5.2. Discussion of the LNO and LSCF samples.

The equivalent circuit used to model the LSCF and LNO samples without the improved interface is represented in Figure 8. It is the combination in series of a Gerischer impedance with a ($R_{if}Q_{if}$). The low frequencies feature ($R_{if}Q_{if}$) is associated to the chemical capacitance of the porous electrode. However, an important difference should be noted between LSCF and LNO samples. The values of the CPE Q_{if} for LSCF are 1.59, 0.0454 and 0.0024 ($S{\cdot}s^{-n}$) at 800, 600 and 400°C whereas for LNO the values of the CPE Q_{if} are 0.0035, 0.0045 and 0.0075 ($S{\cdot}s^{-n}$). For LSCF, the activation energy of the temperature dependence for Q_{if} is ~173kJ/mol at high temperatures and ~20kJ/mol at low temperatures. For LNO, the activation energy of the temperature dependence for Q_{if} is ~17kJ/mol in the whole temperature range. At high temperatures, a difference of three orders of magnitude is measured. It means that a much smaller part of the bulk LNO cathode is electrochemically active than in the bulk LSCF cathode. Two parameters can explain this. First, LNO material is known to have a much higher electronic resistivity than LSCF materials, 3 Ω·cm and 0.004 Ω·cm at 800°C, respectively [9]. The other important parameter is the strong anisotropy observed in LNO for ionic diffusion. At 800°C, the self diffusion coefficient in the basal plane, so called (a,b) plane, is about two orders of magnitude

higher than the self diffusion coefficient along the [001] axis with $D^* = 2x10^{-7}$ $cm^2 \cdot s^{-1}$ and $D^* = 4x10^{-9}$ $cm^2 \cdot s^{-1}$ [30]. Because of the open structure of the porous polycrystalline cathode, the ionic path can be relatively short from the electrolyte upwards. In this case, the surface diffusion of oxygen species on the LNO grains will play a dominant role in the electrode performance.

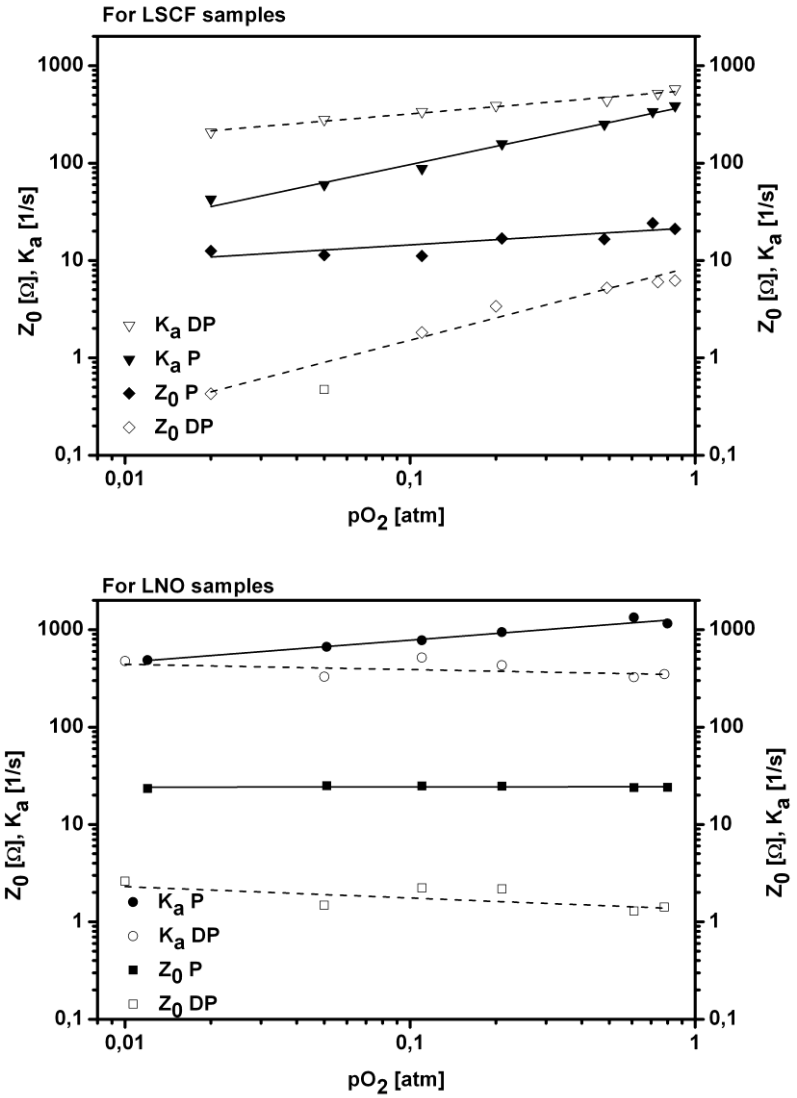

Figure 11. Oxygen partial pressure dependence of Z_0 and K_a for LSCF (top) and LNO (below) samples at 600°C.

When a dense layer is introduced, the equivalent circuit remains unchanged for LSCF samples whereas the introduction of a dense LNO layer is adding a contribution at high frequencies modeled with ($R_{hf}Q_{hf}$). As discussed previously, the value of the pseudo capacitance calculated from the CPE Q_{hf} is in agreement with the chemical capacitance evaluated for a 800nm thick dense LNO layer.

Figure 11 shows the pO_2 dependence of the two Gerischer parameters Z_0 and K_a for LSCF and LNO cathodes with and without the dense layer at the cathode / electrolyte interface. When adding a dense layer, K_a is increased for the LSCF sample and slightly decreased for LNO samples whereas Z_0 is strongly decreased for both materials. From equation (2), it is possible to understand which physical parameters are directly influencing Z_0. When oxygen surface diffusion is increased compared to bulk oxygen diffusion (ν increases), Z_0 is then decreased as observed in the Figure 11.
In the model developed by Adler et al. [24], the accumulation and transport of oxygen on the surface is expressed in terms of apparent storage capacity on the surface, fractional occupancy of the surface and apparent diffusivity. In this case, accumulation of oxygen on the surface is coupled to the rate of oxygen reduction K_a and the vacancy flux in the bulk. A change in the surface / bulk oxygen diffusion ratio is thus indirectly changing the exchange rate K_a.

4. Conclusions.

The microstructure of lanthanum nickelate $La_2NiO_{4+\delta}$ (LNO) cathodes and its effect on the electrochemical performance was presented. The electrochemical performance of LNO cathodes was characterized by means of electrochemical impedance spectroscopy in a symmetrical cell arrangement as a function of temperature and oxygen partial pressure. Two types of cathode microstructures were studied, either traditional screen printed porous LNO cathodes sintered at different temperatures, or a combination of a thin dense LNO layer deposited by Pulsed Laser Deposition and of a screen printed porous LNO cathode. The Area Specific Resistance (ASR) was strongly dependent on the sintering temperature of the screen printed layer. Moreover, the introduction the thin dense LNO layer

at the electrolyte / cathode interface reduced the ASR by a factor 3 compared to the same cathode without thin dense layer. At 700°C, an Area Specific Resistance equal to 0.1 $\Omega \cdot cm^2$ is measured for samples with a 800nm thin dense LNO layer combined with a porous LNO layer sintered at 1000°C using a large Pt mesh as current collector only. The impedance characteristics were modeled with an equivalent circuit in order to explain this improvement. It was observed that the Gerischer impedance was strongly affected by the introduction of the dense layer. A qualitative explanation of this improvement was presented. This microstructure offers more active sites for oxygen exchange towards the electrolyte and thus, the surface occupation of the LNO grains in the porous electrode might be decreased with this dense layer. Oxygen adsorption of oxygen gas and surface diffusion of oxygen species on the LNO grains is facilitated.

References.

[1] Quadakkers W.J., Greiner H., Hansel M., Pattanaik A., Khanna A.S., Mallener W., Solid State Ionics, 91 (1996) 55.

[2] Jiang S.P., Zhang S., Zhen Y.D., J. Electrochem. Soc., 53 (1)(2006) A127.

[3] Oh D., Armstrong E., Jung D., Kan C., Wachsman E., ECS trans., 25 (2) (2009) 2871.

[4] Simner S.P., Anderson M.D., Engelhard M.H., Stevenson J.W., Electrochem. Solid-State Lett., 9 (2006) A478.

[5] Yang M., Bucher E., Sitte W., Proceeding. 9th European SOFC Forum, 29 June – 2 July 2010.

[6] Komatsu T., Chiba R., Arai H., Sato K., J. Power Sourcs, 176 (2008) 132.

[7] Skinner S.J., Kilner J.A., Solid State Ionics, 135 (2000) 709.

[8] Zhao H., Mauvy F., Lalanne C., Bassat J.-M., Fourcade S., Grenier J.-C., Solid State Ionics, 179, 2000 (2008).

[9] Laberty C., Feng Z., Swider-Lyons K.E., Virkar A.V., Electrochem. Solid-State lett., 10 (2007) B170.

[10] Mauvy F., Lalanne C., Bassat J-M., Grenier J-C., Zhao H., Huo L., Stevens P., J. Electrochem. Soc., 153, A1547 (2006).

[11] Rieu M., Sayers R., Laguna-Bercero M.A., Skinner S.J., Lenormand P., Ansart F., J. Electrochem.Soc. 157 (4) (2010) B477.
[12] Hildenbrand N., Boukamp B.A., Nammensma P., Blank D.H.A., Solid State Ionics, doi:10.1016/j.ssi.2010.01.028
[13] Boukamp B.A., J.Electrochem.Soc. 142 (6) (1995) 1885.
[14] Boukamp B.A., Solid State Ionics 20 (1986) 31.
[15] Aguadero A., Alonso J.A., Escudero M.J., Daza L., Solid State Ionics 179 (2008) 393.
[16] Takeda Y., Kanno R., Noda M., Tomida Y., Yamamoto O., J. Electrochem. Soc. 134 (1987) 2656.
[17] Wang D.Y., Nowick A.S., J. Electrochem. Soc., 126 (7) (1979) 1155.
[18] Bawal S.P.G., de Bruin H.J., Franklin A.D., Solid State Ioncis, 9-10 (1983) 973.
[19] Hjalmarsson P., Soegaard M., Mogensen M., Solid State Ionics, 179 (2008) 1422.
[20] Masuda K., Kaimai A., Kawamura K., Nigara Y., Kawada T., Mizusaki J., Yugami H., Arashi H., Stimmimg U., Editor. 473, PV 97-18, (1999).
[21] Chen C.C., Nasrallah M.M., Anderson H.U., Solid State Ionics, 70 (1994)101.
[22] Heiroth S., Lippert T., Wokaun A., Döbeli M., Rupp J.L.M., Scherrer B., Gauckler L.J., J. Europ. Ceram. Soc. 30 (2010) 489.
[23] Adler S.B., Lane J.A., Steele B.C.H., J.Electrochem.Soc. 143 (1996) 3554-64.
[24] Lu Y., Kreller C., Adler S.B., J.Electrochem.Soc. 156 (2009) B513-B525.
[25] Boukamp B.A., Bouwmeester H.J.M., Solid State Ionics, 157 (2003) 29.
[26] Bouwmeester H.J.M., Song C., Zhu J., Yi J., van Sint Annaland M., Boukamp B.A., Physical Chem. Chemical Phys. 11 (2009) 9640.
[27] Escudero M.J., Aguadero A., Alonso J.A., Daza L., J. Electroanalytical Chem. 611 (2007) 107.
[28] Boukamp B.A., Hildenbrand N., Nammensma P., Blank D.H.A., Solid State Ionics, doi:10.1016/j.ssi.2010.05.037.
[29] Fleig J., Merkle R., Maier J., Phys. Chem. Chem. Phys., 9 (2007)

2713.

[30] Bassat J.M., Odier P., Villesuzanne A., Marin C., Pouchard M., Solid State Ionics 167 (2004) 341.

Chapter 7.

Pulsed Laser Deposition: A tool to produce SOFC?

Abstract.

A new method to produce a complete cell with Pulsed Laser Deposition is presented in this chapter. The cell is based on a typical cermet anode used by Energy research Center Netherlands as an anode supported cell. The proper microstructures and crystallographic phases are obtained for the electrolyte, the interlayer and the dense cathode layer at the interface. Pulsed Laser Deposition is seen as a deposition technique that can tackle different problems encountered in the current SOFC production. With PLD it is possible to grow very thin layers in a controlled way, thus minimizing the need for scarce materials and simultaneously decreasing the ohmic resistances. The PLD process is also performed at much lower temperatures than the standard sintering temperatures.

1. Introduction.

In the coming decades, energy supply to the growing economy will be a great challenge. Several solutions will have to be combined in order to sustain the demand. Fuel cells are one of the possible solutions to produce electricity from different fuels such as hydrogen, methanol or natural gas. Solid Oxide Fuel Cells (SOFCs) are working at high temperatures; they can thus use high-energy density hydrocarbon fuels such as propane and butane. In the last years, a considerable effort has been undertaken to reduced the operating temperature of the SOFCs from 1000 °C – 900 °C to 600 °C or even a lower temperature at which the degradations of the fuel cell is expected to be acceptable. A significant amount of materials research has been performed in order to find alternative materials for the cathode, the electrolyte and the anode of the SOFCs. Those different parts always involve rare earth elements.

However, the demand on these elements will only increase in the coming years, as they are used in many applications such as LEDs, car manufacturing, solar cells, etc… A report from the Materials Innovation Institute [1] was issued in November 2009, underlining the problem that can arise from material scarcity. One of the examples studied by the authors is the Zirconium element. Despite growing need for Zirconium and rising prices, the worldwide extraction rate is decreasing. A combination of two main reasons can explain this phenomenon: decrease of the mining activities that are extracting Zirconium and geopolitical decisions. A recent example (end of the year 2010) is the decision by the Chinese government to restrict or stop the export of rare earth metals to the rest of the world whereas it produces 95 % of most of these elements. In this way, the scarcity on the rare earth elements might drastically increase. The first solution given by the authors is to reduce the use of those materials, be more efficient during the production and have products with a long lifetime. At the end of the life of the product, it should of course be recycled. If one starts to produce high quantities of SOFCs with the current deposition techniques that are tape casting and screen printing, the pressure on rare earth materials will increase even more. Using techniques that lead to thinner cells can reduce the use of rare earth materials. Moreover, thinner anode, electrolyte and cathode layers have another positive effect. Not only

using less material for a given area, it is also possible to reduce the losses that reduce the power output by reducing the thickness of the electrolyte and optimizing the materials and their properties. The research done on micro-Solid Oxide Fuel Cells (µ-SOFC) is going in this direction but the target power output is in the range from 1 to 20W for portable electronic devices such as mobile phones or laptops. Planar µ-SOFCs are using thin film deposition techniques and micropatterning on silicon wafer substrates mainly [2-8]. The cell size remains small between 0.0004 and 20 mm^2 and the typical power output of such systems is comprised between 10 and 800 $mW.cm^{-2}$.

The idea presented in this chapter is to combine the techniques and material properties used to produce micro-SOFCs with the large areas of typical planar SOFCs (e.g. 100 cm^2). With Pulsed Laser Deposition (PLD) as deposition technique to build an anode supported cell, very thin and defined layers could be obtained with the right crystallographic phase directly during deposition. In principle, no sintering step is needed after the deposition of the different layers constituting the fuel cell. PLD is usually seen as a research tool only because it is impossible to deposit on large surface and slow deposition rates. A novel PLD system has been developed to deposit thin films on 4 – 6 inches wafers [9-10]. This system could be used to deposit the different layers of a SOFC. Lower amounts of the scarce materials would be used, well defined layers could be obtained, and special crystallographic orientations could be given to the different layers to obtain the best performances.

2. Experimental.

The substrate used for the deposition is a porous Nickel and Nickel oxide/Yttria-Stabilized Ziconia (Ni/YSZ) cermet anode provided by Energy research Centre Netherlands. This taped-casted cermet anode is generally used as anode for an anode supported cell. Its mechanical strength and its small contribution of the anode to the Area Specific Resistance of the whole cell make it a suitable substrate to build the anode supported cell. As received cermet anode samples were carefully cleaned in an ultrasound bath with distilled water, acetone and ethanol in order to remove any impurities present on the surface of the cell prior to deposition. The 8%

Yttria-Stabilized Zirconia (8YSZ) electrolyte, the Cerium Gadolinum Oxide (CGO) interlayer and the Lanthanum Strontium Cobalt Ferrite (LSCF) cathode are grown on the anode substrate with Pulsed Laser Deposition. The experimental Pulsed Laser Deposition setup consists of a KrF excimer laser with a wavelength of 248 nm, a maximum pulse energy of 700mJ and a repetition rate between 1 and 50 Hz. For a better homogeneity and control of the plasma, a mask is used to make a beam profile. The laser beam enters the vacuum chamber (base pressure P = 10^{-7} mbar) after being focused with a lens on the rotating target of the material that has to be deposited. The beam hits the target with a 45° angle with a spotsize varying between 1 and 5 mm^2, depending on the desired fluence and on the plasma expansion dynamics. During the deposition, oxygen, argon and nitrogen can be introduced as background gas and the pressure in the vacuum system is controlled at the desired value, typically between 10^{-2} and 1 mbar. The target substrate separation can be adjusted to the desired distance between 35 and 90 mm.

Targets of different materials are placed on a chariot to be able to deposit different materials in one run. The substrate is clamped onto a heater in order to control the deposition temperature between room temperature and 950°C. The three different layers YSZ, CGO and LSCF are deposited one after each other using different settings. A summary of these settings is presented in Table 1. After deposition, oxygen background pressure is fixed to 100 mbar and the temperature of the heater is brought back to room temperature with a ramp of 1°C/min.

Table 1. Main deposition parameters used for the deposition of the 8YSZ electrolyte, CGO interlayer and LSCF cathode.

Deposition parameters	Electrolyte 8YSZ	Interlayer CGO	Cathode LSCF
pO_2 background (mbar)	0.02	0.02	0.02
Target/substrate distance (mm)	50	50	50
Fluence ($J.cm^{-2}$)	2.2	3	3
Frequency (Hz)	50	20	20
Spotsize (mm^2)	3.4	2.7	3.4
Heater temperature (°C)	25 - 800	750	750
Deposition time (s)	600 - 600	250	250

3. Results and discussion.

3.1. Cleaning procedure.

As shown in Figure 1, the deposition of 8YSZ electrolyte layer on the as-received anode leads to an important delamination of the electrolyte layer from the anode substrate. Big particles are present at the anode / electrolyte interface. A surface analysis of the as-received anode with Scanning Electron Microscopy (SEM) shows that the whole surface is covered with crystals (see Figure 2a). Energy Dispersive X-ray Spectrocopy (EDX) performed during the SEM analysis (Figure 2b), showed clearly that these crystals were sodium chloride contaminations. Carbon-containing dust particles were also present on the surface of the as-received anode. A cleaning step is introduced prior to deposition. The anode substrates are consecutively immersed for three minutes in three different ultrasound baths. First in distilled water in order to remove any salt trace from the surface, then in acetone and finally in ethanol to remove any carbon containing impurities from the surface. Figure 3 shows the surface after the cleaning procedure. Nickel oxide inclusions in a matrix of Yttria Stabilized Zirconia are visible. All other elements (Na, Cl, C) found on the as-received anode substrate cannot be traced anymore, showing the efficiency of the cleaning procedure.

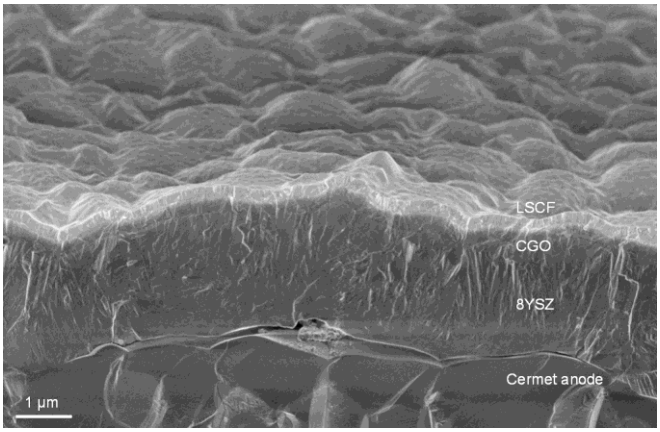

Figure 1. Cross section of the 8YSZ, CGO and LSCF layers deposited on the as received cermet anode.

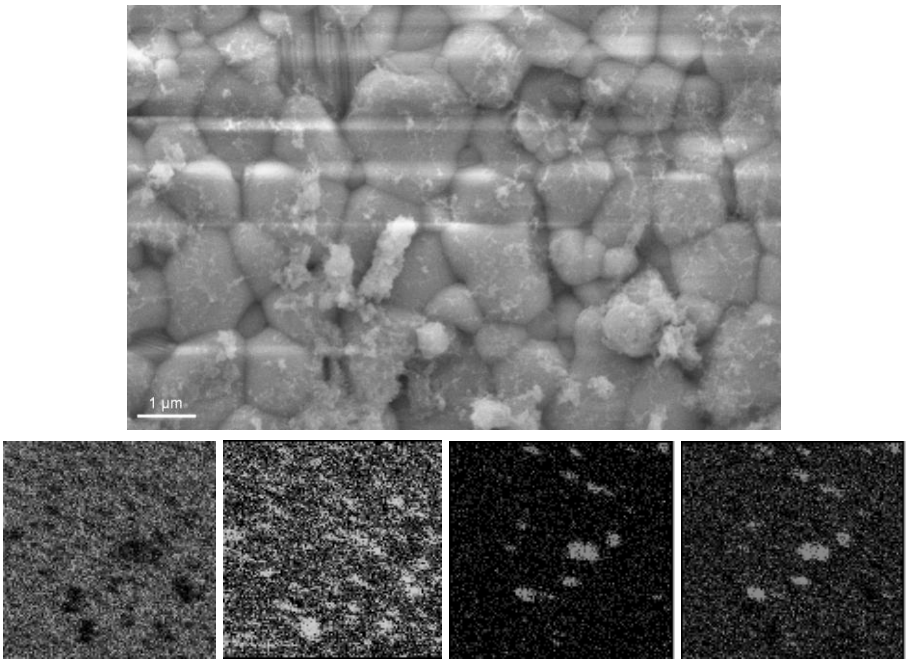

Figure 2. (a) SEM micrograph and (b) SEM element mapping analysis of the surface of the as–received cermet anode for Zr, Ni, Cl and Na (from left to right).

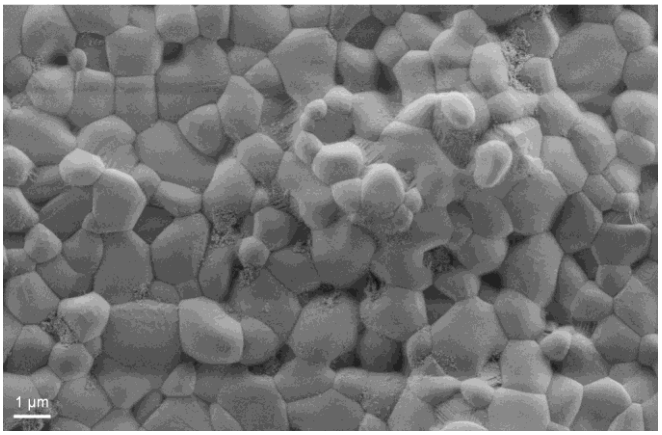

Figure 3. SEM micrograph of the surface of the cermet anode after cleaning process.

3.2. Growth of 8YSZ electrolyte thin films.

As already shown in literature, dense polycrystalline YSZ films are obtained at higher temperature than room temperature [11-14]. In case of a growth at room temperature, only amorphous films are grown because of a poor surface mobility during the growth process. 1 µm thick 8YSZ films is deposited at 800°C on the cermet anode with Pulsed Laser Deposition. Deposition parameters can be found in Table 1. The anode substrate and the deposited electrolyte are made of the same material 8YSZ. X-Ray diffraction (XRD) pattern of 1 µm thick 8YSZ films deposited at 800°C on the cermet anode is shown in Figure 4. For this measurement, omega value is fixed to 1.5° to measure only the top surface of the sample and avoid measuring the substrate.

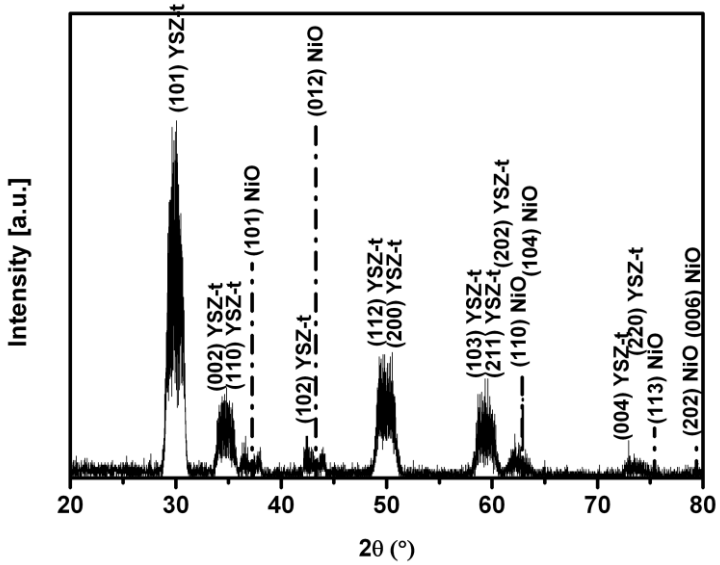

Figure 4. X-Ray Diffraction characterization of the sample after 8YSZ electrolyte deposition at 800°C.

YSZ patterns are clearly visible but also NiO reflections can be observed that might indicate the presence of Ni in the electrolyte. From a purely geometrical point of view, it is possible to calculate the thickness of the layer irradiated by the X-ray beam. It hits the surface with an omega value of 1.5° and the sample is 5 mm large, so the potentially irradiated thickness is 130

microns, a value much larger than the 1 micron YSZ deposited. It is thus not possible to exclude that the NiO peaks in the XRD pattern are due to NiO present in the substrate. No conclusion can be drawn from this XRD measurement about the presence of Ni in the electrolyte or at the electrolyte surface. X-ray Photoelectron Spectroscopy (XPS) was performed on the surface of the 1 µm thick 8YSZ films deposited at 800°C on the cermet anode is shown in Figure 5. The inset correspond to a measurement done on the surface at low a lower scanning pace on a smaller binding energy window around the main pics of nickel. According to this measurement, it can be concluded that during the growth at 800°C of a 1 µm thick 8YSZ films on a cermet anode, there is diffusion of Ni species from the substrate into the electrolyte. Other present peaks are denoted in Table 2.

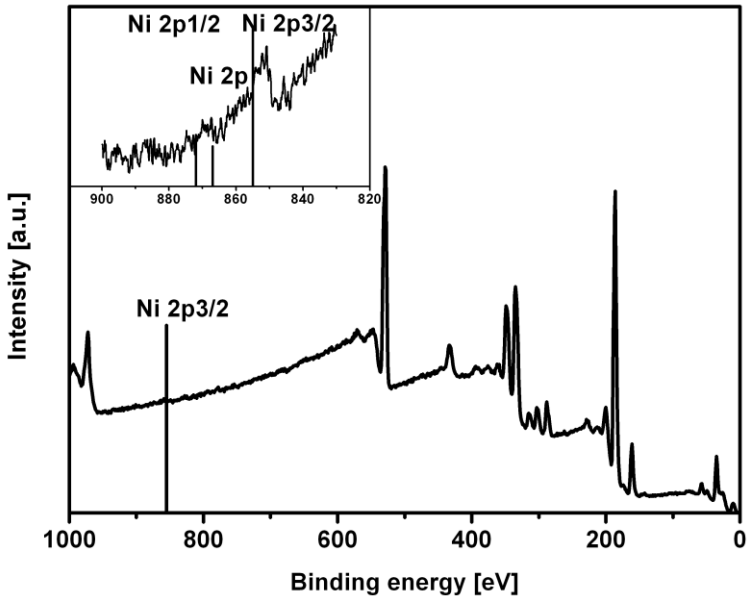

Figure 5. X-ray Photoelectron Spectroscopy analysis of the surface of the sample after 8YSZ electrolyte deposition at 800°C.

The growth of 8YSZ electrolyte is thus performed in a two-step process. The first part of the deposition is performed at room temperature in order to avoid nickel diffusion in the electrolyte. After the deposition of a 500 nm thick amorphous 8YSZ layer at room temperature, the sample is heated to 800°C before further deposition of 8YSZ. In this case, no trace of nickel could be

found on the surface of the electrolyte, either with SEM-EDX, or with XPS. CGO interlayer and LSCF dense layer are then grown according to the parameters shown in Table 1.

Table 2. Binding energies of the elements present at the surface of the sample after 8YSZ electrolyte deposition at 800°C.

Element	Electron State	Binding energy (eV)
C	1s	284
N	1s	399
O	1s	533
K	2s	377
	2p	295
		298
Ca	2s	438
	2p	347
		350
Cl	2s	270
	2p	200
		202
Ni	2s	1011
	2p	857
		873
Y	3s	395
	3p	302
		313
	3d	158
		160
Zr	3s	432
	3p	332
		345
	3d	180
		183

3.3. Full cell characterization and microstructure.

X-Ray Diffraction pattern of the cell Cermet anode / 8YSZ 1 µm / CGO 200 nm / LSCF 200nm is shown in Figure 6. All the deposited films are clearly polycrystalline. The films are grown on a rough polycrystalline substrate (Ni-YSZ cermet). As expected, all (*hkl*) reflections are observed, which indicates that there is no preferred degree of orientation.

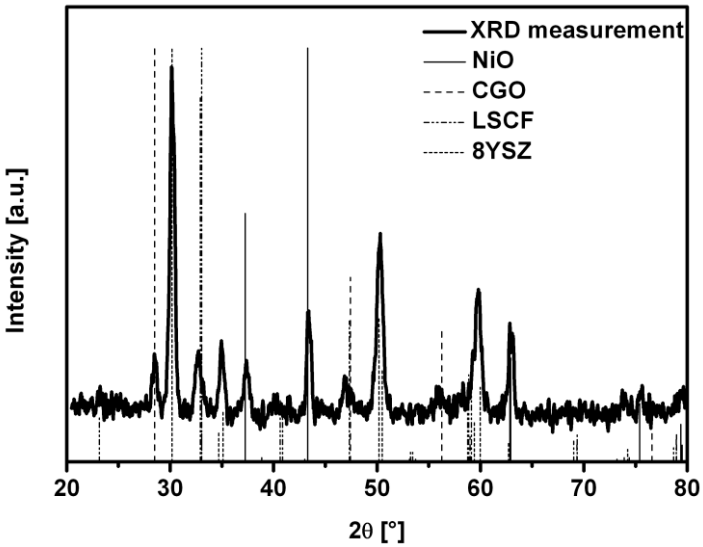

Figure 6. X-Ray Diffraction characterization of the following cell: cermet anode / 8YSZ 1 µm / CGO 250 nm / LSCF 250nm.

The analysis of the cross section of the fuel cell by mean of Scanning Electron Microscopy (see Figure 7) shows a very dense microstructure. After the deposition at 800°C and thus annealing of the layer, no difference can be made between the microstructure of the 8YSZ deposited at room temperature and the deposition of 8YSZ at 800°C. This result is rather surprising. Indeed, during a deposition at room temperature, the poor surface mobility during the growth process could lead not only to an amorphous layer but also to a quite porous layer. Moreover, despite the high frequency rate of the deposition, it still leads to a dense layer after annealing. This annealing step is thus crucial in order to obtain a dense polycrystalline 8YSZ layer. Figure 8 shows a cross section of the interlayer CGO and the LSCF dense layer deposited on the 8YSZ electrolyte. The adhesion of the films is excellent and a columnar growth can be observed for all deposited layers. No apparent porosity can be observed.

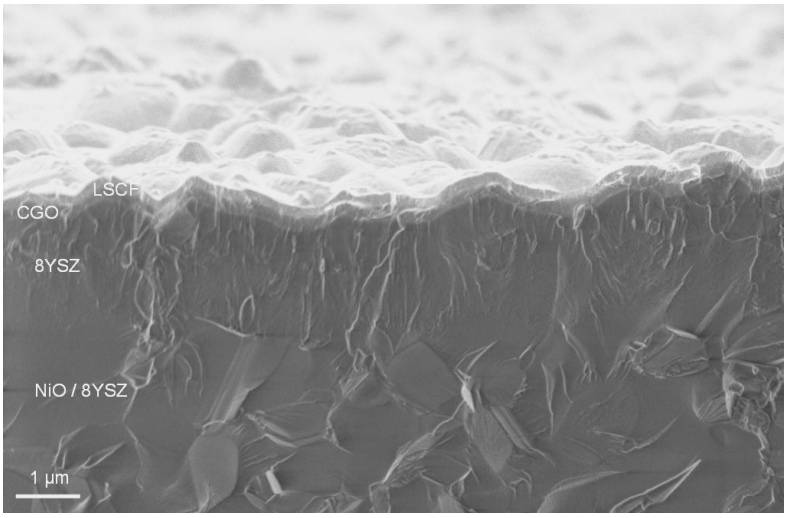

Figure 7. SEM micrographs of the cross section of the full cell produced by PLD.

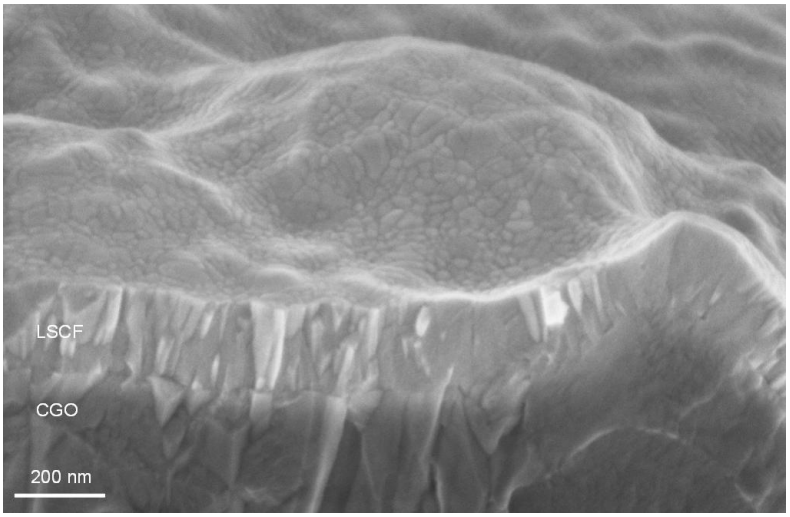

Figure 8. SEM micrograph of the LSCF and CGO thin layers produced by PLD.

4. Conclusions.

A novel way to produce a complete cell with Pulsed Laser Deposition is presented in this chapter. The cell is based on a typical cermet anode used by ECN as an anode supported cell. The right microstructures and crystallographic phases could be obtained for the electrolyte, the interlayer and a dense cathode layer at the interface. Pulsed Laser Deposition presents different advantages when coming to producing Solid Oxide Fuel Cell. It is possible to grow very thin and defined layers on top of each other in one run. A reduced amount of scarce materials is thus used in one cell and a smaller ohmic resistance can be expected from an ultra thin electrolyte. Moreover, the proper crystallographic phases are directly obtained during the deposition: sintering steps are not required any more. The possibility of reactions between the different layers of the cell is thus considerably lowered compared to the reactions that can occur during typical sintering steps at 1200-1400°C. The main drawback of Pulsed Laser Deposition, namely its limitations when it comes to up-scaling and depositing on large areas, is not a drawback anymore. It was demonstrated that large area Pulsed Laser Deposition system would be possible and would work properly to deposit materials comparable to the materials needed in a Solid Oxide Fuel Cell.

References.

[1] Huib W., Bol D., M2i report on Material scarcity, November 2009, available online www.m2i.nl/about-m2i/publications/

[2] Evans A., Bieberle-Huetter A., Rupp J.L.M., Gaukler L.J., J. Power Sources 194 (2009) 119.

[3] Shim J.H., Chao C.C., Huang H., Prinz F.B., Chem. Mater. 19 (2007) 3850.

[4] Muecke U.P., Beckel D., Bernard A., Bieberle-Hutter A., Graf S., Infortuna A., Müller P., Rupp J.L.M., Schneider J., Gauckler L.J., Adv. Funct. Mater. 18 (2008) 1.

[5] Huang H., Nakamura M., Su P.C., Fasching R., Saito Y., Prinz F.B., J. Electrochem. Soc. 154 (2007) B20.

[6] Kwon C.-W., Son J.-W., Lee D.-J., Kim K.-B., Lee J.-H., Lee H.-W., European Fuel Cell Forum (2008) pp. B0519.

[7] Su P.C., Chao C.C., Shim J.H., Fasching R., Prinz F.B., Nano Lett. 8 (2008) 2289.

[8] Rey-Mermet S., Muralt P., Solid State Ionics 179 (2008) 1497.

[9] Janssens J.A., Van De Eijkel G., Dekkers J.M., Broekmaat J.J., Te Riele P., Method for depositing a material, European Patent 08014970.1

[10] Broekmaat J.J., Dekkers J.M., Janssens J.A., Device for projecting an image on a surface and device for moving said image, European Patent 09150125.4.

[11] Zhu, J. and Liu, Z. G., Mater Lett, 57 (2003) 4297.

[12] Heiroth S., Lippert T., Wokaun A., Döbeli M., Appl. Phys. A: Mater. Sci. Process, 93(3) (2008) 639.

[13] Mengucci P., Barucca G., Caricato A. P., Di Cristoforo A., Leggieri G., Luches A., Majnia G., 478 (2005) 125.

[14] Heiroth S., Lippert T., Wokaun A., Döbeli M., Rupp J.L.M., Scherrer B., Gauckler L.J., J. Europ. Ceram. Soc. 30 (2010) 489.

Chapter 8.

Summary and Outlook

In this chapter, the main results of this thesis are briefly evaluated. Some recommendations for further research are given.

In the long road towards commercialization of Solid Oxide Fuel Cells, improving the cathode's performance is a major milestone. Achieving low Area Specific Resistances at temperatures around 600 °C are required to meet the market demands in terms of costs and lifetime. In this thesis, different research projects focusing on the electrolyte / cathode assembly are described with as aims, an improvement of the performance and a better understanding of the cells.

In the cell, the cathode is in direct contact with the electrolyte. Yttria stabilized zirconia is still the state of the art electrolyte, but for low temperature applications Gadolinium doped Ceria (CGO) shows higher ionic conductivity. This promising material shows also good stability with respect to the advanced cobaltite-ferrate cathode materials (here: LSCF). However, a major drawback for the ceria electrolytes is the required high sintering temperature (> 1500 °C) needed to obtain an acceptable density. In chapter 2 a method is shown to obtain CGO pellets with a density above 95% of the theoretical density at temperatures as low as 1100 °C. This reduction in sintering temperature is of importance as reactions between the different layers of the SOFC can easily occur at 1500 °C, but at 1100 °C the reaction rates are significantly reduced.
This new method consists of introducing a small amount (0.5 at.%) of iron (as iron oxide) that will act as a sintering agent. It not only decreases the sintering temperature, but the electrochemical performance of the CGO electrolyte is improved by the addition of iron as it also acts as an impurity scavenger, resulting in a lower grain boundary resistance. This simple synthesis method facilitates electrolyte production and improves the cell performance.

To decrease the Area Specific Resistance (ASR) of the cathodes, two solutions are explored and combined in this thesis. The first possibility is to replace the-state-of-the-art cathode materials by new and innovative materials. These materials should have a lower ASR but also prove their compatibility with the other materials of the actual cell assembly. In chapter 3, a technique using Electrochemical Impedance Spectroscopy (described in chapter 1) is shown to be able to access critical intrinsic parameters of these materials. By using a simple microstructure - a thin dense layer of the

cathode materials -, parameters such as surface exchange coefficient or oxygen diffusion coefficient can be calculated in a relatively simple manner. Great care should be taken when preparing the samples and when performing the measurements as surface contamination and arrangement of the current collector can have a serious influence on the results. In chapter 6, a study on Lanthanum Nickelate ($La_2NiO_{4+\delta}$) as a porous electrode is shown. This material is seen as potentially more stable to chromium poisoning of the cathode because of the poor affinity of chromium species for Lanthanum and Nickel. This material shows excellent oxygen surface exchange and ionic diffusion. However, its strong anisotropy and its relatively poor electronic conduction can be problematic when used as a cathode material. The microstructure of $La_2NiO_{4+\delta}$ has a strong influence on the performance of the cell. At Open Circuit Potential, ASR as low as $0.1\Omega{\cdot}cm^2$ could be measured at 700 °C. Long term measurements in fuel cell conditions should be performed to assess the real potential of this cathode material.

The second possibility is to use one of the state-of-the-art materials and improve its microstructure. In chapter 4, the performance of the cathode material $La_{0.6}Sr_{0.4}Co_{0.2}Fe_{0.8}O_{3-\delta}$ is studied. The microstructure of the LSCF cathode has a strong influence on the cell's performance. Cells sintered at 1200°C showed the lowest apparent electrolyte resistance and the lowest Area Specific Resistance with values as low as $0.70\ \Omega{\cdot}cm^2$ at 550 °C. Both temperature dependence and oxygen partial pressure dependences showed that the cathode performance is limited by surface oxygen exchange kinetics. The impedance characteristics of the cell sintered at 1200 °C were analyzed with the Complex Non-linear Least Square method using different equivalent circuits found in literature. As those equivalent circuits are constructed to understand the performance limitations of the cathodes, a discussion is presented on the appropriateness and the validity of these different equivalent circuits. For the samples presented in this thesis, the use of a Gerischer (or chemical-) impedance in series with a (RQ) impedance to model the overall LSCF electrodes response characteristics was preferred. It not only offers a phenomenological understanding of the electrode processes, the errors inherent to the CNLS analysis were minimized. From the study of porous electrodes in chapter 4 and from the simple dense

electrodes studied in chapter 3, one strong conclusion is that the oxygen surface exchange reaction is limiting the performance of the cathode. Different factors can lead to surface exchange limitation. The intrinsic maximum performance of the material is the first reason. One other possibility is that the surface of the cathode's grain is occupied or poisoned and not accessible for oxygen transfer from the gas phase to the bulk of the cathode.
By engineering the electrolyte / cathode interface, it is shown in chapter 5 for $La_{0.6}Sr_{0.4}Co_{0.2}Fe_{0.8}O_{3-\delta}$ and in chapter 6 for $La_2NiO_{4+\delta}$ that the oxygen surface transport on the cathode grains can be enhanced. The trick consists of introducing a thin dense layer of the cathode material between the porous electrode and the electrolyte. This microstructure offers more active sites for oxygen exchange towards the electrolyte in a region very close to the electrolyte. This enables an enhanced surface diffusion of charged oxygen species, as the 'triple phase boundary' bottle neck is effectively spread out over the entire free surface of the dense layer. Oxygen gas adsorption and surface transport of oxygen species on the cathode grains is facilitated. With this technique, the ASR is reduced by a factor 3 compared to the same cathode without thin dense layer. It means that for the state-of-the-art material $La_{0.6}Sr_{0.4}Co_{0.2}Fe_{0.8}O_{3-\delta}$, the working temperature can be reduced by 75°C. Long term measurements in fuel cell conditions should be performed to assess the real potential of this microstructure.

Finally, chapter 7 is presenting a new method to produce a complete cell with Pulsed Laser Deposition. Pulsed Laser Deposition is a typical example of what nanotechnology – and thus techniques associated to nanotechnology – can bring to improve Solid Oxide Fuel Cells. The cell is based on a typical cermet anode as used by Energy research Center Netherlands for the anode supported cell. The right microstructures and crystallographic phases are obtained for the electrolyte, the interlayer and a dense cathode layer at the interface. Pulsed Laser Deposition is seen as a deposition technique that can tackle different problems encountered in the current SOFC production. Growing very thin layers, use less of the scarce materials, decreasing the ohmic resistance, avoiding high temperatures during production are examples of improvements that PLD can bring. The first measurements in fuel cell conditions should be performed to see the

improvements achieved when using this deposition technique. Moreover, using the PLD technique makes it possible to grow layers in a given orientation if the layer is grown on suitable substrate. By depositing the layered structure $La_2NiO_{4+\delta}$ cathode so that the planes of fast oxygen diffusion are perpendicular to the electrolyte surface, it is then possible to take advantage of the strong anisotropy existing in this material.

Chapter 9.

Samenvatting en vooruitblik

In dit hoofdstuk worden de belangrijkste resultaten nogmaals kort beschouwd. Eveneens worden enkele aanbevelingen voor verder onderzoek gedaan.

In de lange weg naar commercieel succes voor de Vaste Stof Brandstofcellen is de verbetering van de kathode eigenschappen een belangrijke mijlpaal. Het realiseren van een veel lagere oppervlak specifieke weerstand bij temperaturen rond 600°C is noodzakelijk om aan de markt eisen qua kosten en levensduur te voldoen. In dit proefschrift worden een aantal onderzoeksprojecten beschreven met speciale aandacht voor de elektrolyt / elektrode combinatie, waarbij de doelstelling een verbetering in de werking en een beter begrip van het elektrodeproces is.

De kathode is in de brandstofcel in direct contact met het elektrolyt. Yttria gestabiliseerd zirkoonoxide is nog steeds de 'state of the art' elektrolyt, maar voor lage temperatuur toepassingen toont gadolinium gedoteerd ceriumoxide (CGO) een hogere ionengeleiding. Dit veelbelovende materiaal vertoont ook een hoge stabiliteit met betrekking tot de geavanceerde kobaltiet-ferraat gebaseerde kathodematerialen (hier: LSCF). Een groot nadeel is echter dat voor deze ceriumoxide elektrolyten een hoge sintertemperatuur (>1500°C) nodig is om een aanvaardbare dichtheid te bereiken. In hoofdstuk 2 wordt een methode beschreven waarmee CGO pillen met een dichtheid van meer dan 95% van de theoretische dichtheid worden verkregen bij veel lagere temperaturen tot 1100°C. Deze verlaging van de sintertemperatuur is belangrijk omdat reacties tussen de verschillende lagen van de SOFC gemakkelijk kunnen plaatsvinden bij 1500°C, maar bij 1100°C zijn deze reactiesnelheden aanzienlijk gereduceerd.
In deze nieuwe bereidingsmethode wordt een kleine hoeveelheid (0.5 at.%) ijzer geïntroduceerd (als ijzeroxide) dat als sinterhulp fungeert. Hierdoor wordt niet alleen de sintertemperatuur verlaagd maar ook de elektrochemische eigenschappen van het CGO worden verbeterd omdat het toegevoegde ijzer ook werkt als een binder van de onzuiverheden waardoor de korrelgrensweerstand wordt verlaagd. Deze simpele synthesemethode maakt de productie van het elektrolyt eenvoudiger en verbetert tevens de werking van de cel.

Om de oppervlak specifieke weerstand (Area Specific Resistance, ASR) van de kathodes te verlagen worden in dit proefschrift twee mogelijke verbeteringen onderzocht en gecombineerd. De eerste mogelijkheid is om

de ‘state of the art’ kathode materialen te vervangen door nieuwe, innovatieve materialen. Deze materialen moeten niet alleen tot een lagere ‘ASR’ leiden, maar ook compatibel zijn met de andere componenten in de actuele samenstelling van de brandstofcel. In hoofdstuk 3 wordt aangetoond dat het met elektrochemische impedantiespectroscopie (beschreven in hoofdstuk 1) mogelijk is om de kritische, intrinsieke parameters van deze materialen te bepalen. Door gebruik te maken van eenvoudige microstructuren – dunne, dichte lagen van de kathodematerialen – kunnen parameters zoals de oppervlakte uitwisselingscoëfficiënt of de zuurstofdiffusie coëfficiënt op een relatief eenvoudige manier bepaald worden. Grote zorgvuldigheid moet in acht worden genomen bij het maken van de samples en het uitvoeren van de experimenten omdat oppervlakteverontreinigingen en de keuze en plaatsing van het elektrische contact grote invloed kan hebben op de resultaten. In hoofdstuk 6 wordt een onderzoek naar lanthaannikkelaat ($La_2NiO_{4+\delta}$) als poreuze elektrode gepresenteerd. Dit materiaal wordt gezien als potentieel stabieler met betrekking tot chroomvergiftiging van de kathode vanwege de lage affiniteit van chroomverbindingen voor reactie met lanthaan en nikkel. Dit materiaal toont zeer hoge oppervlakte zuurstofuitwisseling en ionogene geleiding. Het materiaal is echter zeer anisotroop en heeft een relatief lage elektrische geleiding, dit kan problematisch zijn in het gebruik als kathodemateriaal. De microstructuur van de $La_2NiO_{4+\delta}$ kathode heeft een grote invloed op de werking van de cel. Bij een opencircuit spanning kon een ASR van 0.1 $\Omega \cdot cm^2$ worden bereikt bij 700°C. Duurexperimenten onder brandstofcelcondities zullen moeten worden uitgevoerd om de uiteindelijke geschiktheid van dit materiaal te bepalen.

De tweede mogelijkheid is om een van de ‘state of the art’ materialen te nemen en verbeteringen in de microstructuur aan te brengen. In hoofdstuk 4 wordt de werking van $La_{0.6}Sr_{0.4}Co_{0.2}Fe_{0.8}O_{3-\delta}$ als kathodemateriaal bestudeerd. De microstructuur heeft een grote invloed op de eigenschappen van de cel. Cellen met kathoden gesinterd op 1200°C hadden de laagste schijnbare elektrolytweerstand en de laagste oppervlak specifieke weerstand (ASR) met als laagste waarde 0.7 $\Omega \cdot cm^2$ bij 550°C. Zowel de

temperatuurafhankelijkheid als de zuurstof drukafhankelijkheid liet zien dat de werking van de kathode wordt bepaald door de snelheid van de zuurstofuitwisseling aan het kathodeoppervlak. De impedantie karakteristieken van de cellen die zijn gesinterd op 1200°C zijn geanalyseerd met een complex kleinste kwadraten methode (CNLS-analysis) waarbij verschillende elektrochemische vervangingsschema's uit de literatuur werden getoetst. Deze verschillende vervangingsschema's zijn opgesteld om de beperkende processen in de kathodes te begrijpen. In een uitgebreide discussie wordt gekeken naar de geschiktheid en de validiteit van deze circuits. Voor de samples die in dit proefschrift worden gepresenteerd heeft de combinatie van een Gerischer (of chemische-) impedantie met een (RQ) impedantie de voorkeur voor de modellering van de totale responsie karakteristiek van de LSCF kathode. Dit leidt niet alleen tot een fenomenologisch begrip van de elektrode processen, maar het resulteert ook in de kleinste afwijkingen in de CNLS analyse. Combinatie van de studie van de poreuze elektroden in hoofdstuk 4 en de eenvoudige dichte elektroden in hoofdstuk 3 leidt tot de duidelijke conclusie dat de zuurstof uitwisselingsreactie aan het oppervlak de beperkende factor is in de werking van de kathode. De eerste reden is de intrinsieke maximale uitwisselingssnelheid van het materiaal. Een tweede mogelijkheid is dat het oppervlak van de korrels van de kathode is bezet of vergiftigd en niet beschikbaar voor zuurstoftransport van de gasfase naar de bulkfase van de kathode.

Door aanpassing van het elektrolyt / kathode grensvlak, in hoofdstuk 5 voor $La_{0.6}Sr_{0.4}Co_{0.2}Fe_{0.8}O_{3-\delta}$ en in hoofdstuk 6 voor $La_2NiO_{4+\delta}$, is aangetoond dat het oppervlakte transport van zuurstof over de kathode korrels kan worden vergroot. De truc bestaat uit de introductie van een dunne dichte laag van het kathode materiaal tussen de poreuze elektrode en het elektrolyt. Deze microstructuur resulteert in meer actieve plaatsen voor de zuurstofuitwisseling naar het elektrolyt in een gebied dat dicht bij het elektrolyt ligt. Dit leidt tot een toename van de oppervlaktediffusie van geladen zuurstofdeeltjes, omdat de beperkende 'drie-fasen-grenslijn' effectief wordt verspreid over het gehele vrije oppervlak van de dichte elektrodelaag. Adsorptie van zuurstof uit de gasfase aan, en oppervlaktetransport van zuurstofdeeltjes over de elektrode korrels wordt hiermee makkelijker. Met deze techniek wordt de 'ASR' met een factor 3

verlaagd in vergelijking tot de zelfde elektrode structuur zonder deze dichte tussenlaag. Dit betekent dat voor het 'state of the art' kathodemateriaal, $La_{0.6}Sr_{0.4}Co_{0.2}Fe_{0.8}O_{3-\delta}$, de werktemperatuur met 75°C verlaagd kan worden. Het is noodzakelijk om duurexperimenten uit te voeren onder brandstofcel condities om de practische waarde van deze microstructuur te bepalen.

In hoofdstuk 7 wordt tenslotte a nieuwe methode gepresenteerd om een complete cel the fabriceren met 'Pulsed Laser Deposition'. PLD is een typisch voorbeeld van wat nanotechnologie – en dus aan nanotechnologie gerelateerde technieken – kan toevoegen aan de verbetering van vaste stof brandstofcellen. De basis van de cel is een typische cermet anode, zoals deze gebruikt werd bij het Energieonderzoek Centrum Nederland voor de anode gedragen cellen. De juiste microstructuren en kristallografische fasen werden gerealiseerd voor het elektrolyt, de barrièrelaag en de dichte kathode laag. Pulsed Laser Depositie wordt gezien als een depositie techniek waarmee verschillende problemen in de huidige productie van de SOFC kunnen worden aangepakt. Het groeien van zeer dunnen lagen, gereduceerd gebruik van schaarse materialen, verlaging van de ohmse weerstand, vermijden van hoge productie temperaturen zijn voorbeelden van verbeteringen die met PLD mogelijk zijn. De eerste test metingen onder werkende brandstofcel condities moeten nog worden uitgevoerd om, bij gebruikmaking van deze depositietechniek, de behaalde verbeteringen aan te kunnen tonen. Bovendien is het mogelijk om met PLD lagen te groeien met een gecontroleerde oriëntatie wanneer deze worden gedeponeerd op daarvoor geëigende substraten. Door de gelaagde structuur van de $La_2NiO_{4+\delta}$ kathode zo te deponeren dat de kristalvlakken met snelle zuurstofionen diffusie loodrecht staan op het elektrolyt oppervlak is het mogelijk om voordeel te behalen uit de sterke anisotropie van dit materiaal.

Acknowledgement - Dankwoord Remerciements

Last but not least, probably the most read section of this book. Within this 4.5 year adventure, I met a lot of people who should appear here. I thank in advance those I forgot to mention.

Bernard, als mijn begeleider heb jij natuurlijk een heel belangrijke rol gehad. Bedankt voor alles wat je voor mij hebt gedaan. Zonder jouw wetenschappelijke en psychologische bijdrage was dit onderzoek nooit zo ver gekomen. Vanaf het begin heb ik op jou kunnen rekenen, zowel in de goede tijden als in de wat donkerdere perioden van mijn PhD.

Dave, bedankt voor de geweldige werksfeer die jij in IMS tot stand hebt weten te brengen: een afdeling waarin zowel natuurkundigen als chemici te vinden zijn, waarin werken in Zwitserland of Spanje ook tot de mogelijkheden behoort. Dit gecombineerd met een grote vrijheid om onderzoek te doen, maakte IMS DE plek om mijn promotie te doen en de Nederlandse cultuur te leren kennen.

Thanks to all my IMS colleagues (please find the complete list on the IMS website and don't forget to look in the Former PhDs and MSc students list). Both scientific and convivial (Gezellig!) aspects were great in this group. From day 1, back on the 15th of October 2006, I felt at ease. Frank!, you played an important role on that very first day: early in the morning, drinking the first coffee, showing the different labs, talking about the IMS volleyball team. Merci.
A special thanks to all my roommates, Minh, Henk, José, Hans on the 6th floor, Michiel, Vittorio, Sajid, Tomek, Sjoerd, Suresh on the 5th floor and

finally Frank! in Carré who had to stand my “Merde!” and “Putain!” from time to time. A special thank to Vasilis Besikiotis. Of course you did great work on the characterization of CGO electrolytes and your input gave me tons of energy.

Within the University of Twente, I would like to thank all the people who helped me to perform my research, Frank and Dick for the assistance in the Mesa+ area, Rico and Mark for the great TEM and SEM input, Joop for the preparation of the ceramic substrates. Thanks to the P-NUT board members for the good work. It was a pleasure to be the chairman of such enthusiastic people.

Outside University but within the scientific world, I would like to thank all former members of the SOFC team at ECN with whom I worked: Bert, Frans, Pieter, Bart, Luuk, Nico, Arno and of course Maciej. With all the changes of the last years at ECN, it was definitely not an easy time for you. Still, we managed to reach an end to this project and I could get some “last” series of samples in order to fill some gaps of my research. Thanks.

Thanks to all my friends in the Netherlands, in France and elsewhere. In good or in bad times, there was always somebody around with whom I could share and talk. Priceless during a PhD… Aan alle Nederlandse vrienden, bedankt voor jullie welkom. Vanaf mijn eerste maanden in Nederland voel ik mij hier thuis en jullie onzichtbare bijdrage aan mijn onderzoek is veel groter dan jullie denken. Merci! A mes amis français que je vois régulièrement pendant les vacances ou les weekends prolongés, quel bonheur de vous savoir présent quelque part en Europe. Merci de continuer à corriger ma grammaire française qui commence à devenir foireuse. Special thanks to my two paranymphs, Meyke and Sébastien not only for being my paranymphs, but also for what you meant / mean / will mean in my life.

Merci à mes parents pour leur aide, visible et invisible, leurs conseils pour mener à bien un tel projet, pour nos éternelles discussions qui servent à former un idéal vers lequel tendre. Bedankt aan Dick, Brigitte, Annet, Arjan, Christien en Bob Jan voor jullie welkom in de familie, gezelligheid en lol in het leven en soms advies voor mijn onderzoek, hè prof. Schoenpapa.

Marian, in welke taal moet ik schrijven? Merci pour ton soutien inconditionnel et ton bonheur de vivre. C'est une irremplaçable source d'énergie pour faire et finir une thèse.

Terminons par la plus petite. Amélie, tu ne le sais pas, mais tu m'as aidé à trouver la concentration et l'énergie nécessaires pour finaliser ce projet. Je te souhaite de pouvoir profiter un jour d'une énergie totalement propre!